

A review of the aerodynamics of airborne wind energy systems

Iván Castro-Fernández^a, Gonzalo Sánchez-Arriaga^b, Manuel García-Villalba^{c,*}

^a Space Programmes Department, Instituto Nacional de Técnica Aeroespacial (INTA), Torrejón de Ardoz 28850, Spain

^b Aerospace Engineering Department, Universidad Carlos III de Madrid, Leganés 28911, Spain

^c Institute of Fluid Mechanics and Heat Transfer, TU Wien, 1060 Vienna, Austria

ARTICLE INFO

Keywords:

Aerodynamics
Airborne wind energy
Experimental characterization
Numerical modeling
Kites

ABSTRACT

Airborne Wind Energy (AWE) systems are tethered aircraft for wind energy harvesting that, since not constrained by a tower like conventional wind turbines, can operate at high altitudes with access to a better wind resource. This work presents a comprehensive review of the current knowledge and state of the art of the aerodynamics of AWE systems. Aerodynamics, which affects power generation, flight physics, control, structure, and safety, among others, is the most transversal area for AWE technology. It is a rich field of experimental and theoretical research due to its significant impact on performance. The review starts organizing actual AWE prototypes, some of them reaching the 100 kW range, according to some selected dimensionless parameters strongly related with their aerodynamics including the Reynolds and Mach numbers, the aspect ratio, the maximum lift-to-weight ratio and aerodynamic efficiency, the reduced frequency, and the sweep and dihedral angles of the wing. AWE machines with different electrical generation solutions (on the ground and onboard), links to the ground (tethered and rotary machines), aircraft (non-rigid or soft, hybrid and fixed wing), and control (aerodynamic surfaces, hanging control pod, ground-based, etc.) are considered and the implication of each architecture on the aerodynamics is discussed. After such a fundamental introduction, the work reviews the current state of AWE numerical and experimental aerodynamics, detailing the modeling methods and key findings. The numerical models are categorized into fast, low- to mid-fidelity methods based on potential flow, and high-fidelity computational fluid dynamics methods like Reynolds-averaged Navier–Stokes and Large-Eddy Simulations. Most numerical studies aim to understand local phenomena by examining the flow and pressure fields over wings, and/or to calculate the aerodynamic force and moment coefficients of 2D airfoils or entire wings. On the experimental side, the significant progress characterizing different types of aircraft in wind tunnels, water channels and in-flight during typical AWE trajectories is summarized. Special attention is paid to the experimental setups and on-board instruments that have been used for the in-situ measurements of aerodynamic variables, as well as the estimation theory and applications of the experimental data to construct aerodynamic models. Furthermore, this paper analyzes the effective application of current numerical and experimental aerodynamic knowledge and models in related areas such as dynamics and control, and fluid–structure interaction. The paper concludes with a critical assessment of the current state of knowledge, highlighting the main open questions, challenges, and opportunities in the field of AWE aerodynamics.

Contents

1. Introduction	3
2. General description of AWE systems	3
2.1. Types of AWE aircraft	3
2.2. Airfoils in AWE aircraft	5
2.3. Characteristic parameters of some AWE machines	5
3. Fundamentals of AWE aerodynamics	6
3.1. Aerodynamic considerations in performance	7
3.2. Aerodynamics during operations	8
3.3. Control in AWE from an aerodynamic point of view	8

* Corresponding author.

E-mail address: manuel.garcia-villalba@tuwien.ac.at (M. García-Villalba).

<https://doi.org/10.1016/j.paerosci.2025.101157>

Received 28 December 2024; Received in revised form 11 November 2025; Accepted 17 November 2025

Available online 29 December 2025

0376-0421/© 2025 The Authors. Published by Elsevier Ltd. This is an open access article under the CC BY license (<http://creativecommons.org/licenses/by/4.0/>).

4.	Numerical and experimental research on AWE aerodynamics	9
4.1.	Numerical modeling	9
4.1.1.	Potential-flow methods	9
4.1.2.	Computational fluid dynamics: RANS and LES	10
4.2.	Experimental characterization	12
4.2.1.	Laboratory tests	12
4.2.2.	Flight tests	14
4.3.	Aerodynamic information for each type of wing	16
5.	Aerodynamics in other AWE areas	19
5.1.	Aerodynamics in dynamics and control	19
5.1.1.	Constant aerodynamic coefficients	19
5.1.2.	Look-up tables	19
5.1.3.	Constant aerodynamic derivatives	20
5.1.4.	Aerodynamic numerical tool	20
5.2.	Aerodynamics in fluid–structure interaction	21
6.	Future avenues for AWE aerodynamics	22
6.1.	Critical assessment of the current aerodynamic methods in AWE	22
6.2.	Open questions and challenges	23
6.3.	Opportunities	24
7.	Conclusions	25
	CRedit authorship contribution statement	25
	Declaration of competing interest	25
	Acknowledgments	25
	Appendix. Survey of works on experimental aerodynamic characterization	25
	Data availability	28
	References	28

List of notations

$(L/W)_{max}$	Maximum lift-to-weight ratio
α	Angle of attack
β	Sideslip angle
ω	Angular velocity of the aircraft
C_F	Vector of aerodynamic force coefficients
C_M	Vector of aerodynamic moment coefficients
F_A	Aerodynamic force
F_T	Tether force
M_A	Aerodynamic moment about the center of mass
u_c	Vector of deflections of ailerons, elevator and rudder
V_A	Aerodynamic velocity
V_K	Absolute velocity of the aircraft
V_W	Wind velocity
δ_a	Deflection of the ailerons
δ_e	Deflection of the elevator
δ_r	Deflection of the rudder
Λ	Aspect ratio
μ	Air viscosity
ρ	Air density
ζ_{FF}	Energy harvesting factor of a fly-gen system
ζ_{GG}	Energy harvesting factor of a ground-gen system
a	Speed of sound
b	Wingspan
c	Mean aerodynamic chord
C_A	Total aerodynamic force coefficient
C_D	Drag coefficient
C_L	Lift coefficient
$C_{D,r}$	Drag coefficient of the rotors

$C_{i,j}$	Stability derivative with $i = F, M$ and $j = 0, \beta, \omega, u_c$
$C_{L,max}$	Maximum lift coefficient
D	Drag
D_r	Drag induced by the rotors
D_t	Total drag (aircraft + rotors)
E	Aerodynamic efficiency
E_{max}	Maximum aerodynamic efficiency
f	Reeling factor
g	Gravitational acceleration
k	Reduced frequency
L	Lift
L_c	Length of the control tether or bridle line
L_p	Length of the power tether or bridle line
$L_{c,l}$	Length of the left control tether or bridle line
$L_{c,r}$	Length of the right control tether or bridle line
M	Mach number
m_K	Aircraft mass
P_W	Wind power
P_{FG}	Mechanical power generated by a fly-gen system
P_{GG}	Mechanical power generated by a ground-gen system
Re	Reynolds number
S	Wing area
T	Period of the crosswind patterns
$V_{K,\parallel}$	Absolute velocity of the aircraft parallel to the tether
$V_{K,\perp}$	Absolute velocity of the aircraft perpendicular to the tether
W/S	Wing loading

1. Introduction

Airborne Wind Energy (AWE) systems employ tethered aircraft to harvest energy from high-altitude winds overcoming some of the current limitations of established wind technology [1–3]. Along with their low material usage and high portability, AWE systems can reach heights above 300–500 m – beyond the reach of standard wind turbines – where studies have highlighted the high power density and availability of wind energy [4–6]. Although airborne windmills were studied in the United States and the Soviet Union before, the late 1970s was a turning point for AWE systems with the publication of seminal works [7,8] and the identification of three modes of operation to generate electricity by Loyd [9]: (i) the simple kite with a reel-out motion aligned with the tether, (ii) the lift power mode (also known as ground-gen and shown in Fig. 1a) where the kite flies crosswind trajectories (i.e., orthogonal to the wind) to pull the tether and move a generator on the ground, and (iii) the drag power mode (also known as fly-gen and shown in Fig. 1b) which uses onboard wind turbines creating additional drag that is converted into electricity and transferred back to ground through a conductive tether. At a later stage, Rotary AWE (RAWA) systems emerged, consisting of light structures with rotor blades, typically kept aloft by a stationary kite to generate electricity either on the ground (Fig. 1c) or onboard (Fig. 1d) [10–12]. Besides energy generation, transportation applications may also benefit from the traction of tethered aircraft. For instance, SkySails Power [13] became a pioneer of kite-based propulsion systems for seagoing vessels [14], later transferring this knowledge to the AWE field [15]. The idea of pulling a ship with a kite to generate electricity with hydraulic turbines was pursued by early works presented in the 2nd airborne wind energy conference in Stanford, CA in 2010 [16], and a similar concept to generate green hydrogen with the harvested wind energy is currently targeted by Oceanergy [17]. A singular vehicle known as the Windsled towed by a 150 m² kite was employed in several expeditions to the polar regions [18].

The development of AWE systems was accelerated in the 21st century with an important collaboration between academia and industry. The effort in terms of research and technology development has been summarized in several review papers on architectures and concepts [20–22], and dynamics and control [23–25]. Together with the previously mentioned areas, aerodynamics is a critical area for AWE and a large body of literature is currently available. However, to the best of our knowledge, no review has been conducted to organize and analyze our current understanding and the remaining challenges. For this reason, the main goal of this work is to review the state of the art of AWE numerical and experimental aerodynamics detailing the methods and main lessons learned. Wind-assist propulsion systems have clear synergies with AWE in terms of dynamics and control, and aerodynamics, among others. Therefore, the knowledge and remaining challenges shared in this review are fully applicable to both fields. The types of AWE aircraft and large variety of airfoils used together with typical parameters of current AWE machines are presented in Section 2. The fundamental aerodynamic aspects in performance, operations and control are revised in Section 3. A compendium of the published numerical and experimental works on AWE systems aerodynamics, which becomes the core of this review, is given in Section 4. Then, a survey of numerical aerodynamic methods used in two of the main areas in AWE: dynamics and control, and Fluid–Structure Interaction (FSI) simulations, is presented in Section 5. Finally, the main open questions, challenges and opportunities in the aerodynamic field identified in this review are summarized in Section 6 and the conclusions of this work are drawn in Section 7.

2. General description of AWE systems

2.1. Types of AWE aircraft

A great variety of AWE concepts have emerged since the beginning of the 21st century [20,24]. The main types are shown in Fig. 2,

which displays a selection of commercial AWE systems to illustrate the types of generation (ground-gen and fly-gen) and operation modes (crosswind and rotary) associated with each type of wing. This selection is not intended to be exhaustive but merely illustrative of the existing companies and research groups. One way of classifying them is by the type of aircraft or wing used [26]. The wings can be broadly grouped into fixed-wing (a–b), non-rigid or soft (c–d), hybrid (e–f) and rotary (g–h) aircraft. AWE aircraft use a significant portion of their aerodynamic forces to generate electricity, in addition to lifting their own weight and propelling themselves. Therefore, the design should be as light as possible while meeting the structural and aerodynamic requirements. For instance, the pioneering fly-gen company Makani Power used a fixed-wing aircraft with eight vertical rotors to generate up to 600 kW. Although Makani terminated its operation in early 2020 due to discontinued funding by the owners, the Makani team placed its accumulated experience and lessons learned during 13 years of development in 3 public comprehensive reports [27–29] and an online resource library [30]. Windlift [31] adopts a similar fixed-wing configuration, though with four vertical rotors instead of eight. Ground-gen systems like Kitemill (Fig. 2b) [32], Mozaero (successor of Ampyx Power) [33] and TwingTec [34] also use a fixed-wing aircraft with rotors to perform vertical and horizontal take-off and landing. Fixed-wing machines (Figs. 2a–b) may use stability and control elements based on elevators, rudders and ailerons like conventional airplanes [35,36]. Moreover, these aircraft are also subject to static and dynamic aeroelastic phenomena such as divergence and flutter, that were shown to be strongly influenced by the tether force and bridle geometry by Wijnja et al. [37]. Box wing configurations like that featured by KiteKraft (Fig. 2a) [38] and Skypull [39] are also used for AWE applications since they can provide stiffness that is comparable with wings of low wing span, with thin and light airfoils [40].

On the other hand, soft or membrane wings are generally employed in ground-gen AWE systems due to their low weight and low cost [15,47,48]. In this case, the high tether forces are distributed over the kite structure thanks to a bridle system. Special attention has been given to Leading-Edge Inflatable (LEI) (Fig. 2c) and ram-air (Fig. 2d) kites by the AWE community, e.g., by pioneering companies like Kitenergy [49]. LEI kites achieve the structural integrity through an inflated leading-edge tubular structure connected to several chordwise struts distributed along the span. A canopy provides the aerodynamic shape and copes with the aerodynamic pressure. Moreover, LEI kites are subject to high aero-structural deformations such as spanwise bending and torsion, and canopy billowing [50,51]. On the other hand, ram-air kites are membrane wings inflated by the apparent wind, similar to paragliders. Besides being very robust and light, they are easily deployed and stowed in the field. However, due to the soft membrane, ram-air kites exhibit significant fluid–structure interaction, leading to camber deformation, spanwise bending and formation of bumps near the leading edge [52–54].

Hybrid wings (Fig. 2e) combine a rigid frame, that provides the structural stiffness, with a textile canopy. A bridle system is normally used to distribute the tether tensions. Hybrid wings have been employed for ground generation by companies like EnerKite [55] and Toyota (Mothership project) [56], and for research purposes by universities like Universidad Carlos III de Madrid (UC3M) [57,58]. In EnerKite's swept wing, the canopy covers a set of rigid ribs and spars and the wing features standard cross-sectional airfoils [59]. These wings behave aerodynamically similar to fixed wings. The first prototype of the Mothership project is an inflatable kite with four semi-rigid control surfaces and a pitch control device, allowing for onboard aerodynamic control [60]. In commercial delta kites, like those used by UC3M, the frame is made of carbon fiber bars and supports the membrane canopy only at the outer edges. As a result, the canopy experiences low to moderate aeroelastic deformations [61,62]. Moreover, hybrid wings present a lower control response time than soft wings due to the favorable balance between stiffness and inertia of the former [58]. The

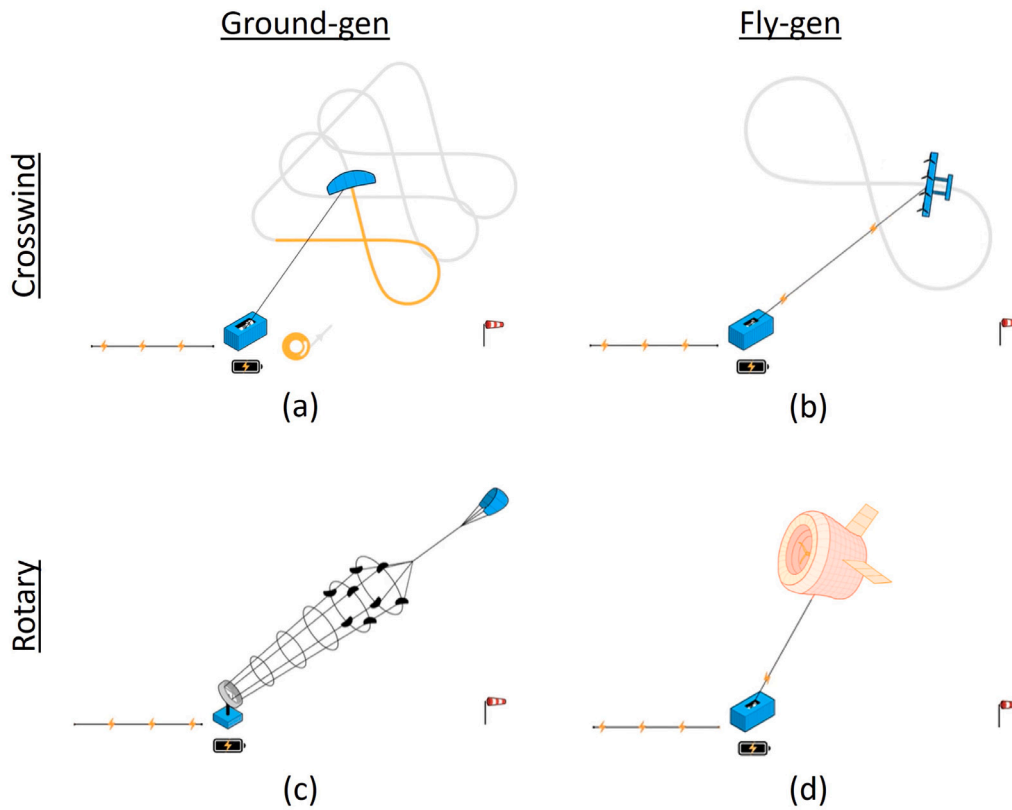


Fig. 1. Main types of AWE systems classified by the place of electricity generation (ground-gen and fly-gen) and the flight operation mode (crosswind and rotary). Source: Illustrations were adapted from Refs. [19,20].

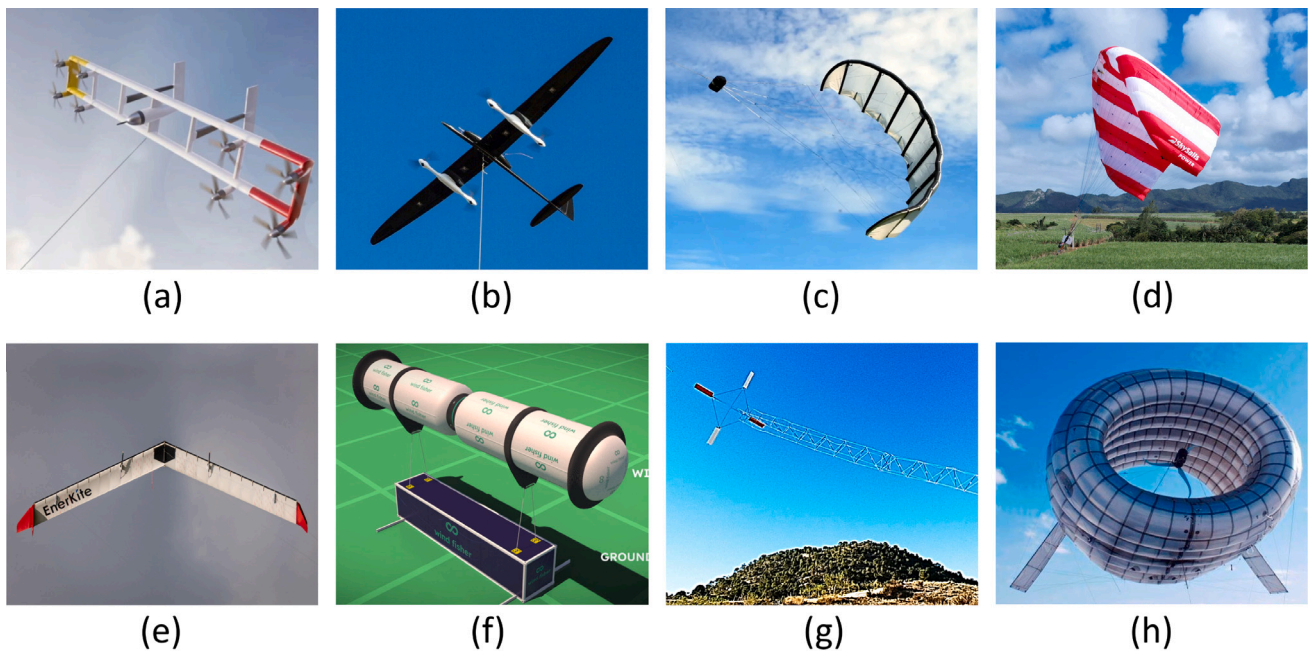


Fig. 2. Main types of fixed-wing (a–b), non-rigid or soft (c–d), hybrid (e–f) and rotary (g–h) aircraft. Selected aircraft (a–h) belong to KiteKraft (100-kW) [41], Kitemill (KM1) [42], Kitepower (Falcon) [43], SkySails Power (SKS PN-14) [13], EnerKite (EK 100) [44], Wind Fisher (MAG100) [45], someAWE (MAR1) [45] and Altaeros (proof-of-concept) [46], respectively.

Magnus-effect AWE system like the one being developed by Wind Fisher (Fig. 2f) is also considered a hybrid structure made of a rigid frame and a textile cover filled with Helium gas to become lighter than air [63]. This rotating dual-cylinder flies crosswind by using the Magnus effect to generate lift and turning torques [64,65].

Rotary AWE systems consist of rotor-blade assemblies that are kept airborne by using a lifting kite, a buoyant structure or their own lift. For instance, the prototypes developed by someAWE (Fig. 2g) [66] and Windswept & Interesting [12] use a static lifting kite to hold a rotor-blade system and a tensesgrity structure, that transfers the aerodynamic torque to the ground. Despite someAWE has established a proof-of-concept [66], future developments will aim to remove the lifting kite and use the lift generated by blades by applying cyclic pitch control, as tested by Unterweger [67]. Other companies like the pioneering MAGENN Power [68] and Altaeros (Fig. 2h) [69,70] proposed to hold the rotor and generator at high altitudes by using lighter-than-air structures similar to aerostats.

2.2. Airfoils in AWE aircraft

As in aerodynamics of conventional aircraft, the overall performance of AWE systems is significantly influenced by the shape of the wing, and in particular by the 2D wing cross-sections also known as airfoils. The geometric variety of the airfoils used in AWE wings is also remarkable. Fig. 3 shows some typical airfoils used by different AWE machines and/or studied in the literature. Fixed (Figs. 3a–b) and hybrid (Fig. 3c) wings commonly employ high-lift airfoils due to its positive influence on the power output (see Section 3.1). This can be achieved for instance by using multi-airfoil configurations [32,71] providing maximum sectional lift coefficients above 3 and up to 4.5 for biplane configurations [38]. Other geometries including flaps and slats to increase the airfoil lift have been considered by former AWE companies like Makani [27] and Ampyx Power [72] (Fig. 3b). However, as strongly recommended by the Makani team [27–29], it is advised to iteratively verify the aerodynamic performance gains against flight data not to overestimate the projected power output. In the optimization of this kind of airfoils, it was shown that the simultaneous parameterization of both slat and airfoil geometries provides the most promising results in terms of maximum lift coefficient (see optimal slat-airfoil geometry in Fig. 3c) [73].

On the other hand, soft kites feature airfoils that differ greatly from those of fixed wings, as well as from one another. For instance, LEI kite airfoils consist of a circular tube and a curved thin canopy as shown in Fig. 3d. Such airfoils are also called sailing airfoils since they have been historically employed in the context of sailing. The most remarkable aerodynamic feature of LEI airfoils is the presence of a recirculation zone behind the leading-edge tube even at low angles of attack. This phenomenon has been studied both in 2D [74–76] and 3D [77,78]. Ram-air kite airfoils are generally thicker and more uniform along the chord [53,54,79]. Fig. 3e shows the airfoil studied in Thedens et al. [79] together with the computed deformed shape without internal airfoil reinforcements, and the bridle attachment points. Indeed, the undesirable formation of bumps on the airfoil lower surface (pressure side) is highly reduced by including reinforcements [79].

Circular airfoils (Fig. 3f) are used by Magnus effect-based AWE systems due to the required axial symmetry in the Magnus effect. The aerodynamic lift and drag generated by the cylinder is strongly correlated to its spin ratio, which compares the rotating angular velocity with the apparent wind velocity. For instance, in Schmidt et al. [65] the lift coefficient, that was experimentally estimated, ranged between 1.5 and 5, and the drag coefficient between 0.5 and 2.5 for spin ratios between 0.5 and 2.5, showing similar trends to the polynomial relationship between the aerodynamic coefficients and spin ratio proposed by Milutinović et al. [80].

Finally, rigid rotors in RAWE machines feature airfoils designed for low Reynolds number applications on small wind turbines, like the FX 63-137 airfoil shown in Fig. 3g [66]. Similarly, the rotors of buoyant airborne wind turbines are also designed with airfoils typically employed in medium-size wind turbine blades like the NREL S-series (e.g., S-820 airfoils is shown in Fig. 3h) as described by Ali and coworkers [81–83]. In contrast, the rotor of some RAWE machines consists of rings of flexible inflatable kites [12], whose airfoils depend on the specific kites used.

2.3. Characteristic parameters of some AWE machines

Table 1 shows some characteristic dimensional and non-dimensional parameters of the selected commercial and pre-commercial machines shown in Fig. 2. It represents the best effort from the authors to collect or estimate this data based on the information provided by some companies and/or found in the references below every AWE machine in the first row of the table. Regarding dimensional parameters, the rated power of these machines ranges from tens to hundreds of kW at their current technology readiness level, and it scales with the wing area and the altitude of operation, among others. Although its data was not gathered in Table 1, the pioneering Makani fly-gen system targeted a power output of about 600 kW by aggressively scaling up the system. However, this target was never achieved during flight tests for a number of technical reasons, namely, gaps between simulated aerodynamics and insufficient flight test data, tether mass and drag, rotor limits, etc. [27–29]. However, the Makani team noted that higher power levels could be achievable in principle if the system were scaled up more gradually and with substantial improvements in aerodynamics, structural efficiency, and tether performance. The cut-in (minimum required) and cut-out (maximum allowed) wind speeds of operation are between 3 and 25 m/s, similarly to conventional wind turbines [84]. The aircraft mass segregates fixed-wing (heavy), non-rigid (light) and hybrid (medium weight) aircraft. The average airspeed during crosswind operation is a figure of merit related to the power production capability of the machine, since the latter grows with the third power of the airspeed, as shown in Section 3.1. We define the period of the crosswind patterns as the time spent to complete a crosswind trajectory like a circle, a figure of eight or a full blade rotation. This parameter characterizes the period of the quasi-periodic crosswind motion that may lead to cyclic changes in the aerodynamic velocity vector (airspeed, angle of attack and sideslip angle) during the crosswind flight.

Table 1 also gathers important aerodynamic non-dimensional numbers computed with the reference dimensional values of the table or directly taken from the literature (see the main references under each AWE machine), being $\rho = 1.19 \text{ kg/m}^3$, $\mu = 1.75 \times 10^{-5} \text{ kg m}^{-1} \text{ s}^{-1}$ and $a = 340 \text{ m/s}$ the air density, viscosity and speed of sound at a reference height of 300 m, S , b and $c = S/b$ the wing area, wingspan and mean aerodynamic chord, and $g = 9.82 \text{ m/s}^2$ the gravitational acceleration. The Reynolds number Re is between 10^5 – 10^7 which is generally lower than the Reynolds number of commercial aircraft and wind turbines, both reaching up to $Re = 10^8$. The low values of the Mach number M (below 0.15) indicate that these aircraft fly in the incompressible flow regime ($M < 0.3$). However, higher values of the Mach number ($M \sim 0.5$) are reached in the rotor blade tips of some fly-gen aircraft like Kitekraft [89]. The maximum lift coefficient $C_{L,max}$ and maximum aerodynamic efficiency $E_{max} = (C_L/C_D)_{max}$ (maximum ratio between the lift C_L and drag C_D coefficients of the aircraft) are two important aerodynamic performance indicators that have a large influence on the airspeed, and therefore on the power output. For this reason, fixed-wing (a–b) and hybrid (e) aircraft that generally have higher aspect ratios and more optimized airfoil designs than soft kites (c–d), present higher aerodynamic velocities. An extensive list of ram-air kite designs together with their characteristic aerodynamic efficiencies and wing loading (W/S) was reported by de Wachter [52].

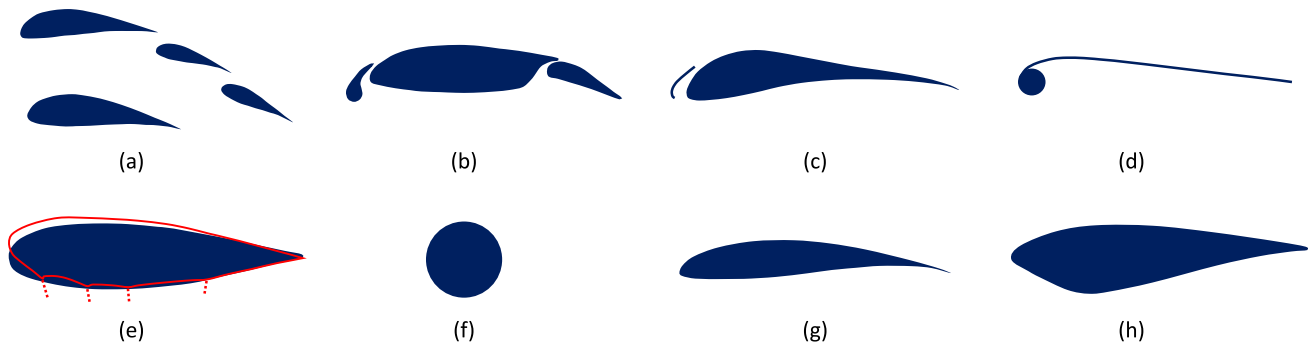


Fig. 3. Typical airfoils in AWE fixed-wing (a–b) [71,72], hybrid (c) [73], LEI (d) [76], ram-air (deformed shape and bridle attachments plotted in red) (e) [79], Magnus effect-based (f) and rotary (g–h) [66,81] aircraft.

Table 1

Characteristic parameters of the selected commercial and pre-commercial AWE machines shown in Figs. 2a–h. Values for the rotary machines (g–h) correspond to one of their blades except for E_{max} in machine (h) that involves the entire airborne wind turbine.

AWE machines								
	(a) Kitekraft [25,38]	(b) Kitemill [25,42,85]	(c) Kitepower [43,50,86]	(d) SkySails Power [13,25,53,54]	(e) EnerKite [44,55,87]	(f) Wind Fisher [45]	(g) someAWE [66,67,88]	(h) Altaeros [46,69,70]
Dimensional parameters								
Rated power (kW)	100	20	100	120	100	100	0.4	2.4
Tether length (m)	150	600	450	800	500	600	30	100
Aircraft mass m_k (kg)	–	–	30	41	160	220	0.5	–
Wing area S (m ²)	10	10	60	180	45.6	91.2	0.1	0.7
Wingspan b (m)	10	7.5	15	23	27	24	0.6	2
Airspeed V_A (m/s)	45	45	30	30	25	20	13	20
Period of the crosswind patterns T (s)	6	7	20	20	10	30	0.5	0.3
Nondimensional parameters								
Reynolds number $Re = \rho V_A c / \mu$ ($\times 10^6$)	2.7	4.5	8	16	2.9	5.2	0.1	0.5
Mach number M	0.13	0.13	0.09	0.09	0.07	0.06	0.04	0.06
Maximum lift coefficient $C_{L,max}$	3.5	1.5	1.3	1	2.6	5	1.5	–
Maximum aerodynamic efficiency $E_{max} = (C_L/C_D)_{max}$	8	8	10	7	15.7	5	10	1.7
Maximum lift-to-weight ratio $(L/W)_{max} = \rho S V_A^2 C_{L,max} / (2m_k g)$	–	–	140	240	27.9	20.1	2.5	–
Aspect ratio $\Lambda = b^2/S$	13	5.5	3.8	2.9	16	6.3	4	5
Sweep angle of the wing (deg)	0	0	0	20	15	0	0	0
Dihedral(+)/Anhedral(–) angle of the wing (deg)	0	0	–34	–30	0	0	0	0
Reduced frequency $k = 2\pi c / (V_A T)$	0.02	0.03	0.04	0.09	0.04	0.04	0.15	0.4

On the other hand, the maximum lift-to-weight ratio $(L/W)_{max}$, that compares the maximum lift with the aircraft weight, is higher in soft kites than in fixed-wing aircraft meaning that the latter spend a larger portion of their aerodynamic forces on lifting themselves. However, the high values of the lift-to-weight ratio for barely all AWE aircraft justify the weightless assumption for basic performance computations as shown in Section 3.1.

Three-dimensional aerodynamic effects are mostly influenced by the aspect ratio of the wing. The higher the latter, the lower induced velocity from the wing tips, achieving better aerodynamic performance. Low aspect ratios (below 5) are employed in current machines, except for the high-aspect-ratio wing by EnerKite (e). Other geometrical parameters such as the sweep and dihedral(+)/anhedral(–) angles of the wing are important for maneuverability, stability and aeroelastic reasons. The only swept wings among the selected machines are SkySails Power (d) and EnerKite (e). Likewise, the only machines that present high anhedral angles are the soft kites by Kite Power (c) and SkySails Power (d). Finally, an important metric for unsteady aerodynamics is the reduced frequency k , which compares the convective fluid time

and the period of the crosswind patterns. Therefore, a high value indicates high unsteadiness and vice versa. The reduced frequency is generally below 0.1 for aircraft a–f which indicates that a combination of aerodynamic quasi-steady and unsteady effects is likely to appear. Indeed, experimental evidence of dynamic stall at similar reduced frequencies was reported for helicopter blades [90] and the UC3M hybrid delta kite [61] when performing high-amplitude pitching motions. Moreover, an early AWE concept based on an oscillating wing was designed to take advantage of unsteady aerodynamics [91]. The system controlled the phasing between the pitch and plunge motions to produce lift and thrust thanks to the unsteady oscillation, besides generating power from the wind. On the other hand, rotary machines present higher values of k due to their low oscillation period being prone to undergo unsteady phenomena similarly to conventional wind turbine blades [92].

3. Fundamentals of AWE aerodynamics

The aerodynamics of AWE systems presents a set of specific characteristics that distinguish these systems from conventional aircraft and

wind turbines. In the first place, the aerodynamics does not only affect to the flight physics and the dynamics and control of the aircraft, but also to the power generation, which is the final objective of the AWE machine. In the second place, the motion and deformation of the aircraft is constrained by the bridle and the main tether, thus reinforcing aero-structural coupling. Finally, the freedom of AWE system to operate within the full wind window opens a large space for design and optimization as compared to wind turbines. For instance, the power generated by a ground-gen AWE machine operated in a figure-of-eight is the result of the full cycle, where the aircraft should have good aerodynamic performance during the straight paths and the turns in the reel-out phase as well as in the reel-in phase (typically done on one side of the wind window). For these reasons, the aerodynamic fundamentals in the performance, operations and control of AWE systems are discussed below.

3.1. Aerodynamic considerations in performance

To discuss the relevant performance equations, Fig. 4(a) displays a 2D diagram of an AWE aircraft operating in crosswind conditions with the absolute velocity of the kite V_K decomposed into its parallel $V_{K,\parallel}$ and perpendicular $V_{K,\perp}$ components to the tether, the wind velocity V_W , aerodynamic velocity $V_A = V_K - V_W$, lift L , total drag D_t (sum of the kite D and the rotors D_r contributions), resultant aerodynamic force F_A and tether force F_T . In the remaining of the work, bold symbols and bold symbols with overlines denote vectors and matrices, respectively, and regular symbols denote scalars (e.g., F_T is the magnitude of vector F_T). For simplicity, the tether elevation angle and the aircraft weight are assumed to be small. The discussion is focused on crosswind operation, either in ground-gen or fly-gen, since it demonstrated to be more advantageous than non-crosswind motion in terms of power production [9]. The mechanical power generated by a ground-gen system reads [9]

$$P_{GG} = F_T V_{K,\parallel} = \frac{1}{2} \rho S C_A V_A^2 V_{K,\parallel}, \quad (1)$$

where $C_A = \sqrt{C_L^2 + C_D^2}$ and we assumed $F_T \approx F_A$, which implies equilibrium conditions. Likewise, the power output of a fly-gen system is defined as the product of the drag generated by the onboard rotors D_r (not plotted in Fig. 4(a) for clarity) and the aerodynamic velocity V_A ,

$$P_{FG} = D_r V_A = \frac{1}{2} \rho S V_A^3 C_{D,r}. \quad (2)$$

The following relationship results from the similarity between the two right triangles colored in blue in Fig. 4(a) [9],

$$\frac{V_A}{V_W} = \frac{V_W - V_{K,\parallel}}{V_W} \frac{F_A}{D_t} = (1-f) \sqrt{1 + \left(\frac{C_L}{C_{D,t}}\right)^2}, \quad (3)$$

being $f \equiv V_{K,\parallel}/V_W$ the reeling factor (non-zero for ground-gen systems and generally zero for fly-gen systems). By using Eq. (3) and defining the wind power as $P_W \equiv \rho S V_W^3/2$, expressions for the energy harvesting factors for ground-gen systems ζ_{GG} as a function of the aerodynamic characteristics of the aircraft and the reeling factor (C_L , C_D , f) and fly-gen systems ζ_{FG} as a function of the aerodynamic characteristics of the aircraft and the rotors (C_L , C_D , $C_{D,r}$) are obtained [9],

$$\begin{aligned} \zeta_{GG} &\equiv \frac{P_{GG}}{P_W} = C_L \sqrt{1 + \frac{1}{E^2} (1 + E^2) f (1-f)^2}, \\ \zeta_{FG} &\equiv \frac{P_{FG}}{P_W} = C_{D,r} \left[1 + \left(\frac{C_L}{C_D + C_{D,r}}\right)^2 \right]^{3/2}. \end{aligned} \quad (4)$$

Fig. 4(b) shows the ground-gen and fly-gen energy harvesting factors versus f and $C_{D,r}$, respectively, for different values of the aerodynamic efficiency E . Both ζ_{GG} and ζ_{FG} increase with the aerodynamic efficiency and reach the same maxima at $\zeta_{GG,opt}(f_{opt} = 1/3) = \zeta_{FG,opt}(C_{D,r,opt} = C_D/2) = 4C_L^3/(27C_D^2)$, where $E \gg 1$ was assumed in

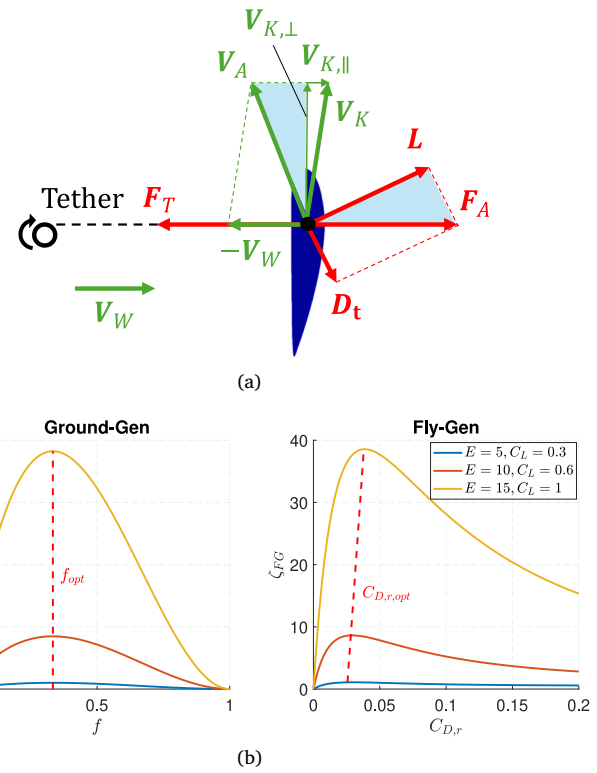


Fig. 4. Panel (a) displays a 2D diagram of an AWE aircraft in crosswind conditions and null tether elevation angle where velocities and forces are represented by green and red arrows, respectively. Panel (b) shows the ground-gen and fly-gen energy harvesting factors versus the reeling factor f and the onboard rotors drag $C_{D,r}$, respectively, for different aerodynamic efficiencies together with the loci of maximum values (dashed red line).

the case of fly-gen systems. It is therefore of great interest for any AWE system to maximize both the aerodynamic efficiency E and the ratio C_L^3/C_D^2 during the crosswind operation. For comparison, the maximum attainable energy harvesting factor during non-crosswind motion for an aerodynamic efficiency $E \rightarrow \infty$ is lower than 0.4 which is about 100 times smaller than the crosswind counterpart for $E = 15$.

Despite Loyd's performance model described above provides a first approximation of the energy harvesting factors, several works revisited these equations. For instance, Trevisi [93] proposed a new normalization of the output power of a fly-gen system P_{FG} . Instead of using the wing area S to compute the wind power P_W , the area of a disk with radius the aircraft wingspan was used. The fact that the latter depends only on the wingspan leads to a key question in AWE design: "given a wingspan, which design maximizes power?"; and slightly different conclusions from Loyd's theory about the optimal aerodynamic figures of merit were found [94].

Other works identified three main power losses that were not accounted for in the basic equations, Eq. (4). The first loss is the tether drag, that is a distributed force parallel to the local aerodynamic velocity of the tether. In performance computations, the total tether drag was approximated to the drag of one quarter of the tether length moving at the aerodynamic speed of the kite [95–97]. Similarly, the effect of tether centrifugal and gravity force was lumped with the kite to refine the power equations [98].

The non-zero elevation angle of the tether and the kite weight also imply important power losses, namely, cubic cosine losses [97,99]. They arise from the misalignment between the resultant aerodynamic force F_A and the tether force F_T invalidating Eq. (3). In addition, it was demonstrated in Ref. [97] that a weightless kite during symmetric flight

(i.e., zero sideslip angle) keeps a constant angle of attack regardless of the tether elevation angle under quasi-steady conditions. Therefore, the weight, among others, is responsible for the changes in the angle of attack along the flight path.

Moreover, induction losses, i.e., the slowdown of the incoming wind caused by the AWE system itself and/or by others in the same farm, has been an active field of research. In conventional wind turbines, this is accounted for in the Betz's limit that poses a constraint on the ratio between the maximum attainable mechanical power with a wind turbine and the kinetic energy of the wind (59.3%). In AWE, Loyd neglected this effect arguing that, to maximize power, the ratio between the wing area and the area swept along the trajectory must be minimized leading to a minimum induction factor [9]. Likewise, later works [5,100] also doubted about the application of the Betz's limit to AWE due to the invalid assumptions of a disk-like swept area and the commonly small ratio between the area of the kite and the swept area along a cycle. However, some analytical studies conducted on multi-kite systems concluded that induction effects can reduce the power production up to 30% in these systems [101,102].

3.2. Aerodynamics during operations

Ground-gen systems operate performing a pumping cycle that broadly consists of two stages as shown in Fig. 1a [14,47,48]. The first one is a traction phase where the kite flies crosswind trajectories such as circular or figure-of-eight patterns reeling out the tether and generating energy thanks to the generator on the ground. As shown in Section 3.1, to maximize the power during this phase, the reel-out speed must be adjusted to achieve an optimal reeling factor f , the angle of attack of the kite α must be set to maximize the aerodynamic figure of merit C_L^3/C_D^2 , and the aerodynamic velocity V_A must be maximized [9]. During the second stage (retraction phase), the tether is reeled in by using a motor on the ground spending a small fraction of the energy generated during the reel-out phase. A depowered configuration of the kite can be set by decreasing the angle of attack and/or bringing the kite to one side of the wind window, among others, with the objective of minimizing the tether tension and, therefore, the energy consumption during this stage.

Fly-gen systems (see Fig. 1b) keep a constant tether length during operation unless a change in operational altitude is commanded or during takeoff and landing [27–29,103]. Interestingly, fly-gen systems reach their optimal power production at exactly the same aircraft aerodynamic setting (C_L and C_D) as ground-gen systems, as demonstrated in Section 3.1 [9]. However, the energy harvesting process also depends on the drag generated by the onboard rotors. Therefore, besides achieving a maximum C_L^3/C_D^2 of the wing and aerodynamic velocity V_A , the design and performance of the onboard wind turbines must be optimized to maximize the power output. During fly-gen operation, there may be power generation and consumption legs with the rotors working as turbines or propellers, respectively [27]. This is due to the effect of gravity which accelerates (flying down) or decelerates (flying up) the aircraft. However, a study on fly-gen trajectory optimization revealed that it is theoretically possible to perform full cycles without power consumption legs at the expense of having large variations of the kite absolute velocity during the cycle [104].

The operation of RAWE machines involves the rotary motion of multiple wings/blades that constitute or are mounted on a static aircraft, i.e., not flying crosswind as shown in Figs. 1c–d [10–12,66]. The operation is qualitatively similar to vertical-axis and horizontal-axis wind turbines, where the crosswind motion is performed by the blades and not by the holding structure. However, RAWE machines present some of the key advantages of AWE systems being light, portable and accessing to strong winds by regulating the operating altitude. The aerodynamic characteristics during operation depend on the subtype of RAWE machines. For instance, lighter-than-air (buoyant) RAWE machines feature horizontal-axis rotors that behave aerodynamically

similar to conventional wind turbines. Indeed, the technology demonstrator of Altaeros used a commercial, small-scale rotor aiming at leveraging the lessons learned in conventional wind energy [69,70]. Other RAWE machines are held by a static lifting kite and the rotor operates at an incidence angle with respect to the wind as shown in Fig. 2g [66]. On the other hand, RAWE machines based on the autogyro principle use rotors to generate lift to stay aloft and aerodynamic torque to generate electricity [10,11]. Companies like Sky WindPower [105,106] and SkyMill Energy [107,108] and Joby Energy [109] pursued this concept with the aim of harnessing high-altitude winds – specifically tapping the jet stream at about 10,000 m – in the early 2010s. However, using the rotors for dual purposes reduces their energy-harvesting capability. This is because the theoretical maximum power coefficient decreases as the angle of incidence (the angle between the rotor plane and the wind) increases, resulting in more lift but less aerodynamic torque, as shown in Roberts et al. [10]. Although Roberts et al. [10] and Rimkus and Das [11] did not consider it, cyclic pitch control has been demonstrated as a viable solution to steer the rotor by actively adjusting its angle of incidence and the direction of lift [67].

3.3. Control in AWE from an aerodynamic point of view

Control becomes an essential building block in every AWE system since it is needed during the whole operation including takeoff, reeling in/reeling out the tethers, flying crosswind trajectories, powering/depowering the kites and landing. Typically, the reel in/reel out control of the tether is decoupled from the pitching and lateral-directional control of the aircraft [24]. The two latter have important aerodynamic considerations regardless of the specific control strategy used. They are performed differently depending on the type of AWE system. As shown in Fig. 5a, fixed-wing aircraft have the possibility to use aerodynamic control surfaces (deflection of ailerons δ_a , elevators δ_e and rudder δ_r) to create aerodynamic torques about their center of mass that cause the aircraft to turn similarly to a conventional airplane [27,35,36,103].

On the other hand, soft and hybrid kites use other mechanisms to generate turning torques. Longitudinal control is achieved by applying a differential length between the power L_p and control L_c tethers (for multi-tether AWE systems) or bridle lines (for AWE systems with one tether and a bridle) causing a change in the pitch angle as shown in Figs. 5b–c. For the lateral steering, they need a differential length between the control tethers or bridle lines ($L_{c,l}$ and $L_{c,r}$), also known as steering input, that is imposed by a ground control unit for multi-tether systems [58,110,111] or an onboard control unit for single-tether systems [15,86,112] (Figs. 5b and 5c, respectively). Multiple experimental studies highlighted the correlation between the steering input and the time derivative of the kite course angle [58,113–115], defined as the angle between the kite velocity vector and the north vector in a local north-east-down reference frame with origin at the kite center of mass, demonstrating that the steering input induces a change in the attitude of the kite. Moreover, it was observed that the steering input has a correlation with the differential tether tension of a multi-tether hybrid kite [58] (Fig. 5b). Even though the precise turning mechanism was not studied, it can be inferred that this differential tether tension induces a roll angle on the kite that generates a nonzero lift component toward the center of curvature of the turn similarly to conventional aircraft. In soft kites, the steering input has been correlated with the aero-structural deformation in LEI kites [50,51,113,116,117]. These kites turn by performing first a yaw rotation caused by an aerodynamic yaw moment. The latter is induced by an asymmetric aero-structural deformation, i.e., spanwise torsion, as shown in Fig. 5c, that induces asymmetric drag and lift distributions.

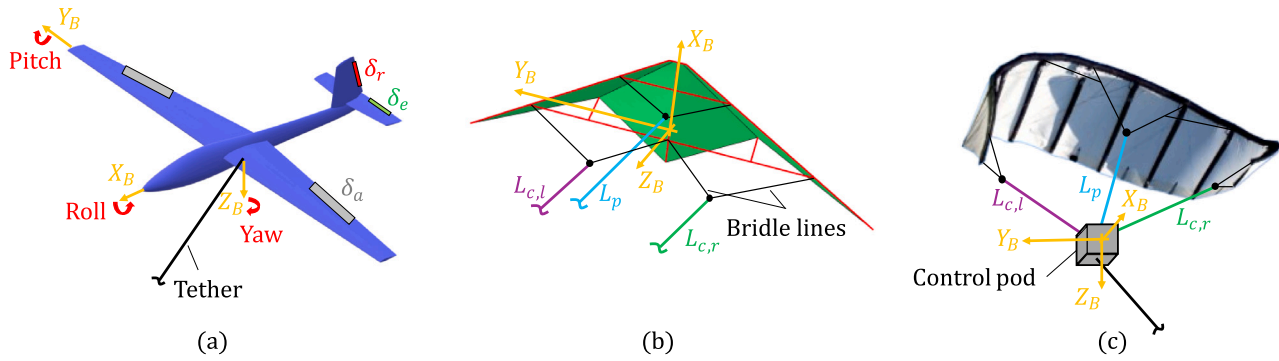


Fig. 5. Panel (a) displays the body axes (denoted by subscript B), roll, pitch and yaw angles and the control surface deflections ($\delta_a, \delta_r, \delta_e$) in a fixed-wing AWE aircraft. Panel (b) shows the body axes and the lengths of the power tether L_p , and the left $L_{c,l}$ and right $L_{c,r}$ control tethers in a multi-tether hybrid kite (figure adapted from Castro-Fernández et al. [61]). Panel (c) shows the body axes and the power, left and right bridle lines actuated by an hanging control pod during a turn induced by asymmetric aero-structural deformation in a LEI kite (figure adapted from Oehler and Schmehl [117]).

4. Numerical and experimental research on AWE aerodynamics

Due to its impact on the performance, the aerodynamics of AWE systems have been investigated by using a plethora of numerical models and experimental setups. The former covered a broad range in terms of fidelity and computational cost and the latter mainly includes test benches prepared by research groups and AWE prototypes owned by private companies.

4.1. Numerical modeling

The Reynolds number of operation of AWE systems is relatively large, $\mathcal{O}(10^6 - 10^7)$, while the Mach number is rather low, $M \lesssim 0.1$ (see Table 1). Therefore, these systems fly in the incompressible flow regime and the aerodynamics is well modeled by the Navier–Stokes equations of the incompressible flow. Since the Reynolds number is large, the boundary layers on the wing are typically thin but prone to becoming turbulent due to several effects, such as the presence of ambient perturbations or, in some configurations, the intrinsic complexity of the wing geometry. When a laminar boundary layer over a solid surface encounters an adverse pressure gradient it may separate from the surface. The separated shear layer may reattach to the surface, forming an attached turbulent boundary layer and creating what is known as a laminar separation bubble (LSB) [118]. Such LSBs influence significantly the aerodynamic performance. In addition, certain configurations are prone to flow separation at the leading edge, which can result in dynamic stall [119]. This is due to the large angles of attack typically required for crosswind operation in AWE systems, along with the sharp turns in their trajectory.

Therefore, depending on the aerodynamic phenomena of interest, a wide range of modeling approaches have been employed, differing primarily in physical fidelity rather than in the underlying numerical discretization schemes. These approaches include potential-flow models, which neglect viscous and rotational effects and are suited for attached flows, and Computational Fluid Dynamics (CFD) models that solve the Navier–Stokes equations using turbulence-modeling techniques such as Reynolds-Averaged Navier–Stokes (RANS) or Large-Eddy Simulation (LES) [120]. Each of these flow models may be implemented using various numerical methods (finite volume, finite element, etc.), but for clarity, in this review we classify the literature according to the aerodynamic modeling fidelity. Direct numerical simulation (DNS), while representing the highest-fidelity approach, remains computationally prohibitive for the Reynolds numbers relevant to AWE applications and is therefore not utilized for practical design or simulation tasks. The reviewed works have been classified in Table 2 depending on the aerodynamic model and type of AWE aircraft.

4.1.1. Potential-flow methods



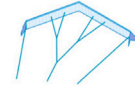


For preliminary calculations where quick results are needed, low- to mid-fidelity aerodynamic models are employed, most of them based on potential-flow methods. Under the potential-flow approximation, the flow is assumed to be inviscid and irrotational, which are reasonable assumptions for attached flows at high Reynolds numbers. For steady, incompressible flow, the equations of motion are simplified, and the flow velocity can be obtained by solving a Laplace equation for the velocity potential. Although nowadays it is feasible to solve directly the Laplace equation in arbitrary domains, using for example finite element methods [153], this is rarely done in practice. Instead, the employed numerical methods are based on the superposition of singularities (vortices, source/sinks, doublets, etc.) that are distributed on the aerodynamic surfaces [154]. The singularities are solutions of the Laplace equation, whose strengths are determined by imposing the non-penetration boundary condition at the surface of the object. Various methods with different levels of complexity are available. In the following, we discuss briefly the most important ones and some of their applications to AWE systems.

The simplest methods that take into account 3D effects are those based on Prandtl lifting-line theory [155]. They model the distribution of lift along the span of finite aspect ratio wings by using a finite number of planar horseshoe vortices that are placed along the wing span. Such methods are limited to small angles of attack and thin airfoils. Among other limitations, they do not account for variations of flow conditions or airfoil shapes along the span, which is a strong limitation for wings with substantial tapering or sweep. This methodology has been used in the context of AWE systems by several authors [37,121,123]. Jackson [121] developed a theory to determine the optimal shape of tension kites using lifting-line theory, combined with the condition that the kite's shape and spanwise tension must balance the forces acting perpendicular to it. The solution reveals both the kite's shape and the twist distribution needed to achieve the desired loading. Leloup et al. [123] applied the lifting-line method to a LEI kite after verifying the tool against CFD calculations in the case of a paragliding wing. Wijnja et al. [37] used the lifting-line method to study the flutter instability in a fixed-wing AWE system with onboard turbines. A benchmark of various lifting-line methodologies applied to different AWE wings was performed recently by Gaunaa [124], highlighting the influence of implementation details in the accuracy of these methods.

Further developments of the lifting line methods led to the Vortex-Step Methods (VSM), where the vortex sheet in the wake is approximated with a finite number of horseshoe vortices. As discussed by Damiani et al. [128], VSM can be applied to low and high aspect-ratio wings of different shapes, including swept and dihedral wings. In addition, modifications to account for the nonlinear polar curves of real airfoils are typically incorporated. An example of a VSM discretization

Table 2

Works on numerical aerodynamics grouped in aerodynamic methods based on potential flow or CFD, and each of them, subdivided into steady and unsteady solvers (columns), and the specific type of method (bullet points). The blue, orange, green, purple and red colors correspond to aerodynamic works on LEI, ram-air, hybrid, and fixed-wing AWE aircraft, and airborne wind turbines, respectively. Illustrations were adapted from Cherubini et al. [20].

		Potential flow		CFD	
		Steady	Unsteady	Steady	Unsteady
 LEI kites  Ram-air kites  Hybrid wings  Fixed wings  Airborne wind turbines		<p>•Lifting-line methods:</p> <p>Jackson [121], de Soliminihac et al. [122], Leloup et al. [123], Gaunaa [124], Wijnja et al. [37], Haas et al. [125].</p> <p>•Nonlinear vortex-step methods:</p> <p>Duport [126], Cayon et al. [50], Candade et al. [55,59], Ranneberg [127], Damiani et al. [128].</p> <p>•Vortex-lattice and panel methods:</p> <p>Gohl and Luchsinger [129], Leuthold [130], Gaunaa et al. [131], Thedens and Schmehl [54], Castro-Fernández et al. [62], Fasel et al. [132, 133], Eijkelhof et al. [40].</p>	<p>•Lifting-line methods:</p> <p>Trvisi et al. [134], Gaunaa et al. [135].</p> <p>•Nonlinear vortex-step methods:</p> <p>-</p> <p>•Vortex-lattice and panel methods:</p> <p>Castro-Fernández et al. [61, 136], Fonzi et al. [137].</p>	<p>•2D RANS:</p> <p>Bosch et al. [116], Breukels [74], Breukels et al. [75], Folkersma et al. [76], Thedens et al. [79], Fezza and Barber [71], Ko et al. [32], Fischer et al. [73].</p> <p>•3D RANS:</p> <p>Buffoni et al. [138], Viré et al. [77,78], Gaunaa et al. [131], Folkersma et al. [53], Eijkelhof et al. [40], Saleem and Kim [139-141], Ali and Kim [81,83].</p>	<p>•2D RANS:</p> <p>-</p> <p>•3D RANS:</p> <p>Castro-Fernández et al. [61], Kheiri et al. [142,143], Vimalakanthan et al. [72], Pynaert et al. [144-146], Saeed and Kim [147], Ali and Kim [82,148].</p> <p>•LES/DNS:</p> <p>Nejad et al. [149], Scupi et al. [150], Haas et al. [125,151], Crismer et al. [152].</p>

applied to an LEI kite is shown in Fig. 6a [50]. A VSM was used to compute the static and dynamic aerodynamic stability derivatives of a swept wing [127]. Due to its favorable balance between accuracy and computational efficiency, the VSM has been used in aero-structural frameworks of fixed-wing aircraft [59,128] and LEI kites [50]. A similar tool named nonlinear vortex lattice blade element model, that accounts for nonlinear polar of the airfoil and the velocity induced by the rotors, has been developed by Kitecraft [156]. The computational efficiency of this tool has allowed its use for engineering tasks like aircraft design, dimensioning and optimization, as well as real-time control purposes.

More detailed and accurate analysis of complex wing geometries can be obtained with the Vortex Lattice Method (VLM). The wing is represented with a lattice of discrete vortices, so that the surface of the wing is divided into a grid of panels, as depicted in Fig. 6b. In the classical VLM [157, § 5.2], each panel has a horseshoe vortex consisting of a bound vortex segment and trailing vortex legs that extend to infinity. Control points are placed in each panel and the induced velocities at each control point are calculated based on the influence of all vortices in the lattice. Similarly to the lifting-line method, the strength of the vortices is computed to satisfy the non-penetration boundary condition. The method is also limited to small angles of attack and thin wings, but can be applied to complex wing geometries such as those with sweep, taper or dihedral/anhedral. The VLM has been used in various studies of AWE systems, for example, to compute the aerodynamic forces and moments on different kite designs [129]. This methodology was then coupled with a dynamic simulator. The VLM was also used in an FSI simulation of a hybrid delta kite (displayed in Fig. 6b) [62]. The equilibrium shape of the thin canopy was highly influenced by the pressure distribution provided by the VLM. Furthermore, Gaunaa et al. [131] studied a C-type kite with a uniform sectional shape. Adding viscous corrections to the VLM, they compared their results to CFD predictions, with good agreement for the cases where the flow was attached. Since flow separation may occur on the suction side and behind the leading-edge tube of LEI kites, a multiple-wake VLM that shed part of the total circulation from prescribed separation positions was proposed by Leuthold [130]. However, the author highlighted the sensitivity of this method to the prescribed separation and re-attachment points.

Finally, panel methods are the most versatile of the potential-flow methods, employing a variety of singularities (source/sinks, doublets, vortices) depending on the particular formulation of the method. They are used in potential-flow problems (2D or 3D) around airfoils or wings of arbitrary shape. This makes them particularly useful for thick airfoils/wings consisting of an upper and a lower surface. An example of a typical panel method discretization applied to a ram-air kite is shown in Fig. 6c [158]. In the context of AWE systems, panel methods have been useful to determine the pressure distribution over a ram-air kite [54] and box wing kites [40]. A panel method was also employed to obtain the pressure distribution over camber-morphing AWE wings within an aero-structural optimization [132] and a reduced-order model [133]. In these studies, the panel method showed its potential to capture the effects of airfoil thickness and camber changes.

It is often possible to incorporate unsteady effects in the above methodologies. For example, Gaunaa et al. [135] added unsteady capabilities to their lifting-line method to capture the effects of the varying kinematics of a fixed-wing aircraft on a prescribed path. Fonzi et al. [137] employed an unsteady VLM in a nonlinear aeroelastic framework for a fixed-wing kite. Another unsteady VLM was employed by Castro-Fernández et al. [61,136] for a pitching delta kite in an attempt to capture dynamic stall phenomena. These authors illustrated the limitations of potential-flow methods, since the unsteady panel method failed to reproduce experimental observations.

4.1.2. Computational fluid dynamics: RANS and LES

Often, more accurate predictions than those provided by potential flow methods are needed, making the use of CFD necessary [159,160]. Given the high Reynolds number of operation of AWE systems, turbulence modeling is, in practice, required, since the direct solution of the equations is computationally too expensive. If a direct solution is intended, then the Reynolds number has to be severely reduced. This was done for example by Nejad et al. [149], who computed the 2D flow over a tethered kite at $Re = 730$.

A turbulent flow is characterized by a wide range of length and time scales, from the energetic large-scales to the small scales, where dissipation of energy takes place by viscous effects. This separation of scales is exploited in LES methods [161]. A filtering operation is introduced

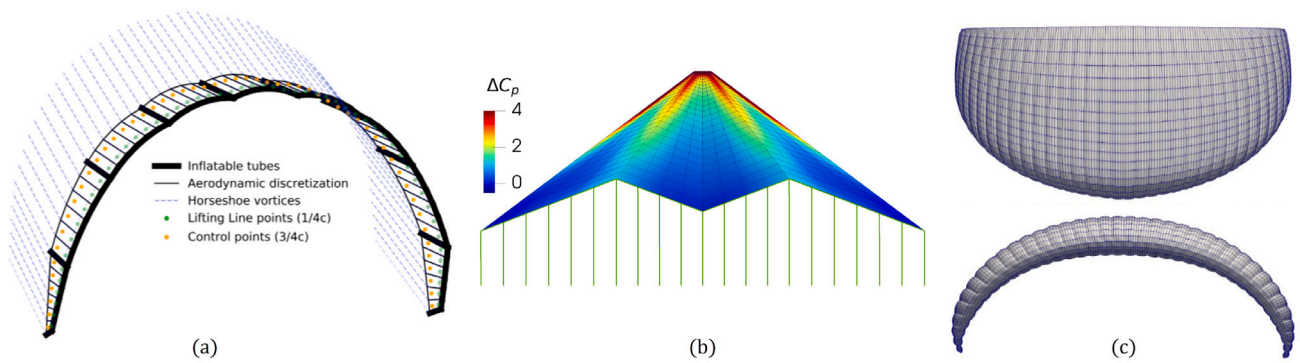


Fig. 6. Spatial discretizations of the VSM (a), VLM (b) and panel (c) methods applied to AWE wings. Panel (a): LEI kite with horseshoe vortices and control points, among others, in Cayon et al. [50]. Panel (b): quadrilateral vortex rings on the surface of a delta kite (colored with the pressure coefficient) and wake vortex lines (green) in Castro-Fernández et al. [62]. Panel (c): mesh of a ram-air kite used in a panel method in Thedens et al. [158].

to separate the large scales from the small scales, leading to the filtered Navier–Stokes equations. The large scales are computed by solving the filtered equations, while the small scales are modeled using a so-called sub-grid scale model. This technique, while being significantly less costly than DNS, is still computationally very expensive. This is because the calculations need to be three-dimensional and time-dependent, even if one is interested in the mean flow only. As a consequence, LES has not found widespread use in AWE systems yet. There are however some exceptions, for example, Haas et al. [125] employed LES to study the large-scale aerodynamics of an AWE farm consisting of ground-gen and fly-gen AWE systems. LES was also employed to compute the highly-separated flow of a full-scale kite for auxiliary propulsion of ships at high angles of attack (nearly perpendicular to the wind) [150]. The computations revealed unsteady components of the drag and lift associated to the turbulent wake and vortical shedding from the wing tips. In closely related fields, LES is being used for Reynolds numbers and operation conditions similar to those of AWE systems. For example, Vinuesa et al. [162] performed highly-resolved LES up to $Re = 10^6$ of the turbulent boundary layers developing around a wing with NACA airfoil cross-sections. Another relevant work was reported by Visbal and Garmann [163], who studied the onset of unsteady separation and dynamic stall vortex formation over a constant-rate pitching wing using LES at $Re = 2 \cdot 10^5$. Thus, it is expected that in the near future, LES will be adopted by the AWE community, as such works are starting to appear in recent conferences [151,152]. However, it is likely that it will be employed mainly to provide understanding of relevant flow phenomena associated to wind turbulence, for instance, rather than being used for design calculations.

An alternative approach consists in averaging the Navier–Stokes equations to separate the mean flow and the turbulent fluctuations. The averaging procedure was introduced by Reynolds, leading to the so-called RANS equations [164]. These equations require closure of one of the terms involving the turbulent fluctuations, i.e. the Reynolds stresses. Since the unknown variables in the RANS equations are the mean velocity and the mean pressure, there is no need to perform time-dependent calculations for statistically-stationary problems. This results in a significant decrease in the computational cost compared to DNS and LES. Also, for high aspect ratio wings, the central sections experience minimal influence from the 3D effects generated at the wing tips. As a consequence, relatively inexpensive 2D RANS calculations of airfoil sections can effectively represent the overall aerodynamic performance of the wing. For non-statistically-stationary problems, like for example when time-periodic maneuvers are performed, it is possible to solve the equations in a time-dependent manner, and this leads to the technique called Unsteady RANS (URANS).

Several studies have utilized 2D RANS calculations to characterize the flow over the various kinds of airfoils employed in AWE systems

or to optimize the airfoil geometry. Particularly interesting is the work of Folkersma et al. [76] who studied the flow over a LEI kite airfoil, similar to the one shown in Fig. 3d. The flow over the suction (upper) side of the airfoil is similar to the flow over a conventional airfoil. However, on the pressure (lower) side a recirculation zone is formed behind the tube, whose size depends on the Reynolds number and on the angle of attack (see Fig. 7a). Interestingly, the wings of some birds have airfoils with a comparable geometry and the formation of a recirculation region in the lower surface has also been reported [165]. In Folkersma et al. [76], the computations were performed for a wide range of Reynolds numbers with the $k-\omega$ SST turbulence model [166] while the effect of boundary layer transition was modeled using the $\gamma-\bar{Re}_{\theta t}$ model [167]. It was found that, at Reynolds numbers below $2 \cdot 10^7$, the aerodynamic performance was influenced by laminar separation occurring both on the suction and pressure sides of the airfoil. The best aerodynamic efficiency was achieved for a condition in which the boundary layer on the suction side remained laminar without the formation of an LSB. As a result of the study, it was hypothesized that the aerodynamic performance of the airfoil could be improved by delaying the boundary layer transition during the traction phase and tripping the transition in the retraction phase. This is because during the traction phase, the flow velocity and corresponding Reynolds number are high; by delaying the transition, the stall angle increases, leading to higher lift and lower drag. Thus, the kite flies faster and produces higher power output. During the retraction phase, the flow velocity is lower and tripping forces the boundary layer to become turbulent. This may lead to an improved performance, since turbulent boundary layers are known to have a delayed separation compared to laminar boundary layers. This is the same principle as the vortex generators employed in some aircraft and wind turbines [168].

For a fixed-wing AWE system, De Fezza and Barber [71] performed 2D RANS simulations of the flow over a multi-element airfoil like the one shown in Fig. 3a. The airfoil was divided into four elements and a parametric study was performed by altering the relative sizes and angles of the airfoil elements. It was found that the figure of merit $E^2 C_L$ could be increased by about 50% with respect to a baseline configuration. A similar multi-element airfoil was optimized using a fast aerodynamic solver (MSES) based on a viscous-inviscid formulation by Ko et al. [32]. These authors also reported 2D RANS simulations that showed that the fast aerodynamic solver provided reasonable predictions for the lift coefficient but a significant underprediction of the drag coefficient. In the AWE community, 2D RANS has often been employed to generate databases to be queried by other low-fidelity aerodynamic models as those discussed in Section 4.1.1 [50,59,75,116,123,128]. This approach has sometimes been extended to include 3D effects. An example is the work of Buffoni et al. [138], who performed 3D RANS calculations of a 3D curved rigid kite. The calculated aerodynamic coefficients were then used to test an active pitch control strategy. Another

early example is the work of Gaunaa et al. [131] who performed 3D RANS calculations to assess the performance of a VLM.

More recent works using 3D RANS have aimed to explore more complex phenomena. For example, Viré et al. [77] extended the 2D work of Folkersma et al. [76] by incorporating 3D effects in their study of the aerodynamic performance of a LEI kite. They showed that a transition model was required to accurately predict the occurrence of stall up to at least $Re = 3 \cdot 10^6$. They also found a large amount of cross flow along the span of the wing, a result that cannot be obtained with the 2D assumption. In a subsequent work, Viré et al. [78] also included in their wing model the effect of eight chordwise strut tubes that support the wing canopy. It was shown that the struts have little influence on the overall aerodynamic performance. However, they do influence the local flow, through the increased vortex shedding around the struts. In Folkersma et al. [53], a similar 3D RANS solver was coupled with a structural solver to study the steady-state aeroelastic behavior of the ram-air kite shown in Fig. 7b. Moreover, the aerodynamic performance of this kite was compared with the LEI kite studied in [77] for similar flow conditions. The flow characteristics around both anhedral kites was similar highlighting the high spanwise flow and the wing tip vortices (see Fig. 7b). However, despite it was already well-known that LEI airfoils develop a strong recirculation region on the pressure side, reducing their performance, the LEI kite showed a better aerodynamic performance across the entire range of angles of attack. The authors attributed this behavior to the higher aspect ratio of the LEI kite, being twice that of the ram-air kite.

Other configurations have also been studied using 3D RANS, such as box wing kites and buoyant wind turbines. Box wing kites have been studied by Eijkelhof et al. [40], who found that the stall of the upper wing was delayed with respect to the lower wing, a phenomenon clearly visible in the visualization shown in Fig. 7c. This happened because the separated flow over the lower wing influenced the effective angle of attack of the upper wing. As a consequence, it was observed that the stall angle was increased with respect to a monoplane wing using similar airfoils. Buoyant wind turbines have been studied in a series of recent works [81,83,139–141]. In these studies, the configuration features a buoyant, ducted shell with integrated airfoils, housing an NREL Phase IV rotor. The computations include both a stationary domain for the shell and a rotating domain for the rotor, which are coupled via a conformal mesh at the interface. Several aspects have been studied, such as the influence of the shape of the shell-integrated airfoils [140] or the quantification of shell augmentation on power output at elevated heights [83].

Although widely used for its reasonable computational cost, steady-state 3D RANS has significant limitations in capturing large-scale unsteady effects, particularly at high angles of attack where flow separation is dominant. In such cases, while URANS may not achieve the accuracy of DNS or LES, it often provides improved predictions compared to steady-state RANS. This was clearly demonstrated by Castro-Fernández et al. [61] in a study of delta kites under dynamic stall conditions. By comparing with experiments, they showed that the unsteady RANS calculations qualitatively matched experimental measurements, identifying a leading-edge vortex (LEV) that formed and detached cyclically during the pitching motion. The LEV attached to the wing is clearly visible in the visualization shown in Fig. 7d. Moreover, the steady and unsteady RANS data were used to fine tune a semi-empirical dynamic stall tool that presented a good accuracy as compared to URANS at a much lower computational cost. Also, relevant is the work of Pynaert and collaborators who have employed URANS to study the effect of wing deformation on an AWE system performing a crosswind flight maneuver [145] and the effect of control surfaces in the CFD framework [146]. In the first of these studies, Pynaert et al. [145] studied a fixed-wing AWE aircraft navigating a logarithmic wind-shear profile. The latter caused periodic variations in the angle of attack, and consequently, in the longitudinal aerodynamic coefficients. This result highlights the importance of considering realistic kinematics between

the aircraft and the wind reference frames. The use of URANS is gradually expanding [72,82,142–144,147,148], however, best practice guidelines need to be established in the AWE community for accurate computation. As an example, some of the recent works employ first-order upwind schemes for the convective terms in the momentum equation, and first-order time integration schemes. It is, however, well known in the CFD community that first-order schemes are too dissipative and, therefore, not recommended; instead, at least second order schemes should be employed [160].

Finally, CFD methods are also employed in the so-called mesoscale models that attempt to predict large-scale atmospheric and weather phenomena. As remarked by some works from the early AWE conferences, there is a variety of mesoscale models, each aiming at resolving different relevant phenomena (turbulence, Earth boundary layer, clouds, etc.) and at very different altitudes [169]. Later on, these models have been mostly employed for wind speed forecasting at altitudes below 2000 m. A mesoscale Weather Research and Forecasting (WRF) model developed by Skamarock and Klemp [170] was used to assess the wind resource and optimal operating altitudes for AWE systems in Sommerfeld et al. [171]. The WRF model was improved by assimilating LIDAR measurements at various altitudes up to 1100 m, that were gathered in a previous work [172], by using observation nudging, demonstrating that the wind speed predictions improved between 300–500 m. By using a simplified AWE model, the most probable optimal altitude for AWE systems was found between 200–600 m. This study was continued in a recent work by assessing the impact of realistic wind profiles predicted by the WRF tool on ground-gen AWE systems [173]. Unlike simplified wind speed approximations (e.g., logarithmic wind profiles), the k-means clustering technique was used to group wind velocity profiles predicted by the WRF model with similar characteristics. Interestingly, small differences between the simplified model and the WRF wind model in the ground-gen system power curves were found when operating offshore, but they differed for onshore operation due to the more frequent non-monotonic wind conditions.

4.2. Experimental characterization

Together with the numerical analysis, the experimental work constitutes the second pillar of our knowledge on AWE aerodynamics. Over three thousand years of flying kites have provided significant insights into kite aerodynamics and flight physics. Moreover, the use of kites in some sport disciplines in the last few decades, like kitesurfing, revolutionized kite design and manufacturing to improve aerodynamic performance and handling quality. Ram-air kites, LEI kites, rigid-framed kites, and soft single skin kites, are all power kites invented by kite designers that used in-flight testing as the main design driver. Originally, the AWE sector drew from the long history of kites and chose power kites for the preparation of the first AWE prototypes due to their low cost and high surface-to-mass ratio. In the last two decades, AWE made significant contributions to kite aerodynamics through wind and water tunnel experiments and flight tests using the ground stations of the AWE prototypes. Nowadays, there are AWE machines with ram-air and LEI kites and fixed-wing aircraft, and in all cases the experimental characterization of the aerodynamics is a cornerstone due to its impact on performance and control.

4.2.1. Laboratory tests

The main advantage of using wind and water tunnels for the aerodynamic characterization of AWE systems is the possibility of carrying out experiments in a controlled and repeatable environment. There is an important body of literature on wind tunnel testing of aircraft later used in AWE or close to it like paragliders, inflatable kites, and ram-air inflated wings offering high-performance in terms of lift (see for instance Refs. [174–177] and therein). For instance, the lift and drag coefficients of several Cody-type kites (a type of box kite for meteorological and military observation) were measured in wind tunnel

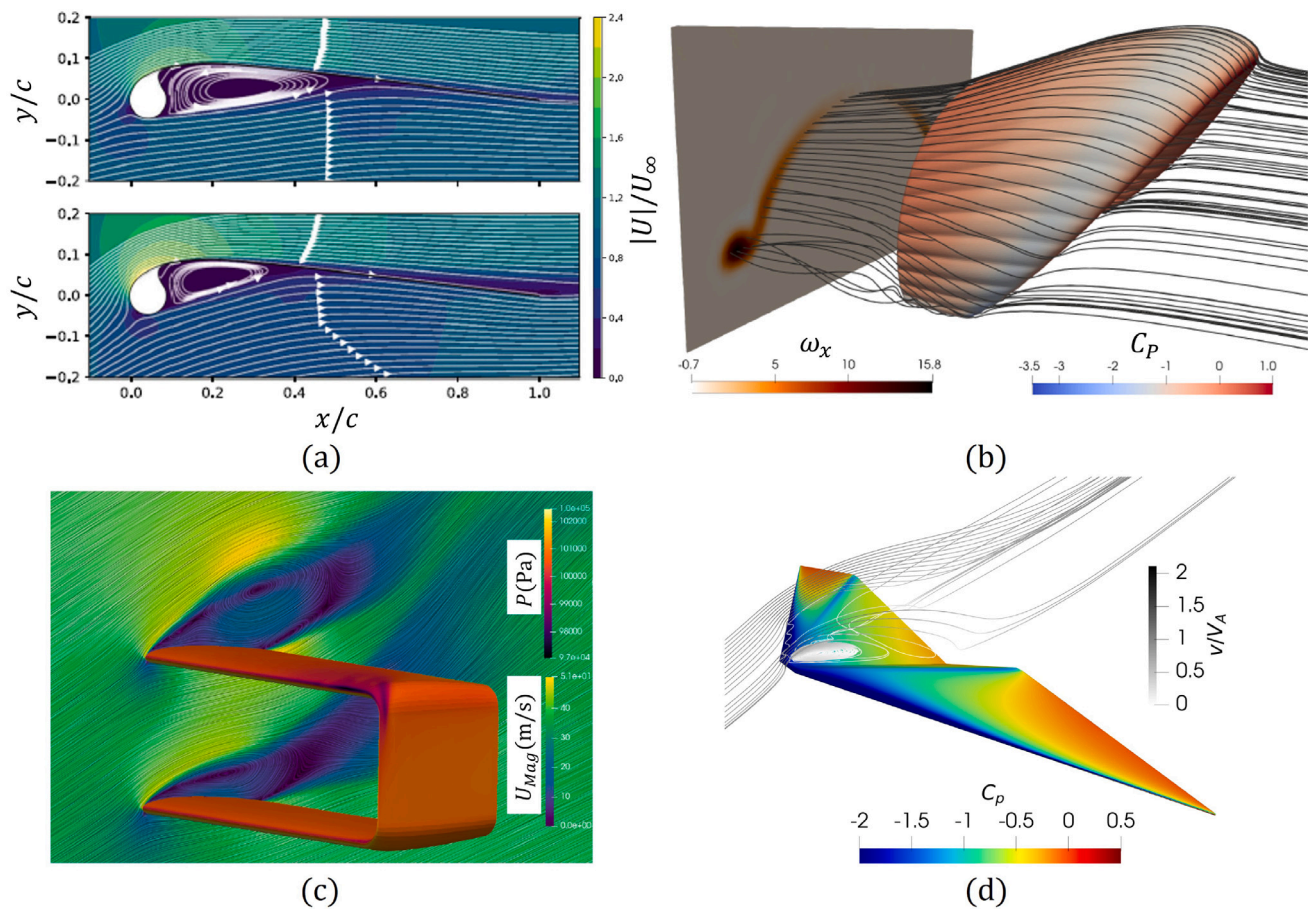


Fig. 7. Panel (a): flow field around a LEI airfoil computed with CFD showing a large recirculation region behind the leading-edge tube at 6° (up) and 12° (down) of angle of attack in Folkersma et al. [76]. Panel (b): streamlines and pressure coefficient over a ram-air kite showing the streamwise component of the vorticity in Folkersma et al. [53], flow is from right to left. Panel (c): Pressure distribution on a box wing and velocity magnitude contour on the symmetry plane in Eijkelhof et al. [40]. Panel (d): flow field and pressure coefficient distribution around a delta kite at the maximum angle of attack (38°) during an unsteady pitching motion in Castro-Fernández et al. [61].

tests in the middle of the 20th century for a broad range of angles of attack and airspeeds [178]. As shown in Section 3.1, these two coefficients play a key role in determining the performance of an AWE machine, and most of the experimental works on AWE were focused on their determination. A summary of some selected works containing the testing facility, wing type, sensors, design parameters or variables varied in the tests and main goal is shown in Table A.7.

A pioneering work on wind tunnel testing of ram-air kites applied to AWE was performed by de Wachter [52]. Besides measuring C_L and C_D and analyzing the state of the boundary layer with a thermographic camera, photogrammetry and laser scanning techniques were used to investigate the aero-structural deformation of a 6 m² ram-air kite. This is a crucial aspect of ram-air kites, as it can lead to structural collapse and imposes additional constraints on the flight envelope, particularly in terms of the angle of attack and speed. The three-dimensional shape of the kite was captured and later used to make a CFD analysis and relate kite deformation with changes in the aerodynamic coefficients. The ram-air wing of the EK30 prototype, a three-line ground-actuated system developed by EnerKite GmbH, was also tested in a wind tunnel [87]. The aerodynamics of a 1.3 m² four-line ram-air kite was studied by Rementeria Zalduegui [179]. The experimental setup had a frame that emulates the control input of the kite and transmits the aerodynamic loads to an external six-component strain-gauge balance. Therefore, it allowed to measure the force and torque produced by the kite as well as to simulate kite turning. The study provided interesting qualitative information, but difficulties related to lateral-directional

instabilities in the tests driven by the interaction of the wake with the wind tunnel walls hindered high-quality quantitative data. The drag and lift coefficients of a kite for propelling marine shipping were also studied in wind tunnel tests and with LES simulations [150]. The kite was rigid (3D printed), untwisted with a cambered span, constant chord length, and a section profile consisting of NACA 4415 airfoils. The parametric analysis varying the attack and sideslip angles provided quantitative values for C_D and C_L and revealed that the time evolution of the force coefficients is not steady due to the turbulent wake behind the kite and the vortex shedding from the kite's ends.

LEI kites substituted ram-air kites in some AWE prototypes in the 2010s looking for better aerodynamic performance, larger wind windows, and trying to avoid the kite collapse under low free-stream dynamic pressure. However, similarly to ram-air kites, their testing in the wind tunnel is challenging due to the difficulty of adequately scaling down large inflatable membrane structures. LEI kites have a similar shape to the commonly named sailwings, which are structures with a circular leading edge and a membrane as discussed above. In 1979, A. Bruining measured the lift and drag coefficients of a rigid sailwing section made of a cylinder and an arc-shaped rigid plate [180]. One year later, a similar work, but using a rigid cylinder and a dacron sail, measured a higher $(C_L/C_D)_{max}$ [181]. However, as pointed out in Folkersma et al. [76], the Reynolds number in the experiments of Refs. [180,181] was in the order of 10^5 – 5×10^5 , which is relevant for the retraction phase of AWE systems, but a Reynolds number of about 10^6 – 10^7 is reached in the traction phase. More recently, a scale model

of a 25 m² LEI kite was manufactured with carbon fiber reinforced polymer and tested in a wind tunnel [182]. The rigid kite was suspended in the wind tunnel thanks to a support structure that included a motorized mechanism to change the angle of attack and sideslip angle, and a six-axis force balance. The force and moment coefficients were measured for different angles of attack and sideslip angles at realistic Reynolds numbers, and the lift and drag curves were compared to theoretical analyses based on the vortex-step method and CFD. Further works using this setup and adding capabilities like stereoscopic particle image velocimetry are expected to be available soon.

Together with LEI kites, inflatable kites are a good alternative to avoid the collapse of ram-air kites. These structures have been used for a long time in a wide range of applications (see Ref. [183] and therein). AWE is not an exception, and tethered inflatable kites were also tested in wind tunnels. For instance, in Ref. [184] two inflatable kites were tested within a speed range of 15 to 32.5 m/s and for three tether attachment configurations. The experimental database, which includes stereo photogrammetry data, force and moment measurements, and wake pressure measurements, is available in a public repository and constitutes a valuable source for validating aeroelastic models and high-fidelity CFD simulations.

Regarding fixed wings, TU Delft research group and a team of Makani engineers tested a small scale model of the wing of the M600 AWE machine in the low-speed low-turbulence wind tunnel of TU Delft [37,185]. They validated the flutter modes previously identified with the software package ASWING. The aerodynamic coefficients of the Kitecraft system were measured in a wind tunnel up to a maximum wind speed of 20 m/s [89]. The S1223 airfoil and an optimized airfoil with thin slat were tested in a wind tunnel up to a Reynolds number of 1.2×10^6 [73].

The aerodynamic and dynamic properties of several aerostats applied to AWE have also been investigated in the laboratory. A water channel was used to investigate the longitudinal and lateral modes of the buoyant airborne turbine of Altaeros Energies [186]. In a later work, the same aerostat was studied [187] focusing on validating a dimensional analysis to properly scale the laboratory-scale models to yield an equivalent dynamic response. Experiments in a water channel and in a wind tunnel with aerostats models of different scale showed that the aerodynamic coefficients are preserved all the way up to full scale [187].

In addition to wind and water tunnel testing, singular laboratory infrastructures has been developed specifically for AWE systems. An example is the rotating arm for the launch and recovery of unpropelled tethered airplanes developed at KU Leuven, shown in Fig. 8a [188]. Originally designed for the experimental validation of advanced estimation and control techniques [189], the infrastructure can measure the position and attitude of the airplane as well as the position of the arm. The experimental setup allowed to validate the control based on the deflection of two aerodynamic surfaces (ailerons and elevator) [188]. There are also laboratory infrastructures for Unmanned Aerial Vehicle (UAV) with potential synergies with AWE because both involve tethered aircraft. For instance, a spherical pendulum-like laboratory testbed was useful to characterize the dynamic and aeroelastic behavior of a UAV [190]. A flow measurement system consisting of vanes and a pitot tube was mounted on the UAV to measure the full aerodynamic velocity vector. This unconventional infrastructure, that was shown to be useful to investigate the behavior of semi-aeroelastic hinged wing tips, may also have applications to AWE.

4.2.2. Flight tests

Abundant aerodynamic information can also be obtained from flight tests. The conditions are not as controllable and repeatable as in the laboratory, but it is possible to test the aircraft at real scale, performing relevant AWE maneuvers and without wind tunnel wall effects. Flight data can provide valuable information about the dynamics, the control and the aerodynamics to be used for the validation of performance [97], dynamic [193,194], aerodynamic [61,77,136] and aeroelastic [50,51] models. The quantity and quality of the data mainly

depend on the quality of the prototype or experimental setup, which includes the ground station and onboard instruments, and the estimation algorithm that is used to determine the aerodynamic characteristics from the measurements. Both aspects are discussed below. Moreover, Table A.8 contains a survey of experimental AWE works related to in-flight aerodynamic characterization identifying the testing facility, wing type, sensors and estimators, actuators and main goal.

The list of AWE prototypes and experimental setups developed by universities and research centers [47,110–112,195–197], and companies [31,42–45,48,66,87,198,199] is very long (find a more complete list in Refs. [1,2]). Most of them are oriented to power generation but, directly or indirectly, they can provide experimental aerodynamic data or data that can be related with the aerodynamic behavior of the aircraft. Common sensors available at the ground station are load cells and line-angle sensors to measure the tether (or tethers) tensions and direction (azimuth and elevation angles) at the ground, weather station and LIDAR to measure wind velocity and direction on the ground and at the aircraft's height, Global Navigation Satellite System (GNSS) receivers for ground station position, encoders to determine the full control vector of the ground station, and camera systems to determine the aircraft and tether position, among others. The most used onboard sensors are the Inertial Measurement Units (IMUs) and the GNSS receivers to measure the position, velocity, attitude and angular velocity of the aircraft. None of these sensors provide a direct measurement of the body-components of the aerodynamic velocity vector V_A , which is an essential piece of information to carry out aerodynamic analysis. However, it can be obtained indirectly as follows. Firstly, the wind velocity V_W at the aircraft is measured with a LIDAR or estimated by combining a model for the wind profile with the measurement of the weather station. Secondly, the wind velocity is combined with the aircraft absolute velocity measured by the onboard GNSS (V_K) to find

$$V_A = V_K - V_W. \quad (5)$$

However, such a procedure typically provides poor results due to experimental errors in the measurements of both vectors. For this reason, AWE experimental setups that focused on aerodynamic research added onboard sensors for the in-situ measurement of V_A like multi-hole pitot tubes and pitot tubes combined with systems based on vanes. Surface tufts combined with onboard cameras were also used to visualize the state of the boundary layer (see for instance Fig. 8d).

Most of the ground stations are fixed to the ground and require a nonzero wind speed to perform the flight testing. However, other facilities move their ground stations to mimic the wind conditions and enable AWE testing at a null ambient wind speed. For instance, a pioneering work on the aerodynamic parameter identification of a single-skin traction kite was carried out in 2005 by using a tow test setup with a car and a circular flight testing strategy [200,201]. Another tow test rig was prepared in Dadd et al. [202] to measure the aerodynamic efficiency and the lift coefficient of a ram-air kite. Load cells and angular displacement transducers were used to measure the tension vector, whereas the angle of attack was obtained photographically by taking a side view of the kite. The work was later extended to consider several figure-of-eight trajectories [203]. A single-tethered inflatable kite was built by using the tensairity concept, that provides extra stiffness and load-bearing capacity by combining the inflatable structure with struts and cables, and tested by towing the kite with a car [204]. Measurements of the airspeed, and the line angle and tension allowed to compute the lift and drag coefficients. The lift coefficient and the aerodynamic efficiency of several LEI kites were measured by using another tow setup (see Fig. 8b) [111]. In order to provide constant and controllable flow conditions, and enhancing repeatability, the setup was installed on a car trailer and the driver adjusted the desired aerodynamic velocity. A similar tow test setup was developed by the University of Kyushu and used to test the equilibrium position and figure-of-eight maneuvers of a LEI kite [112].

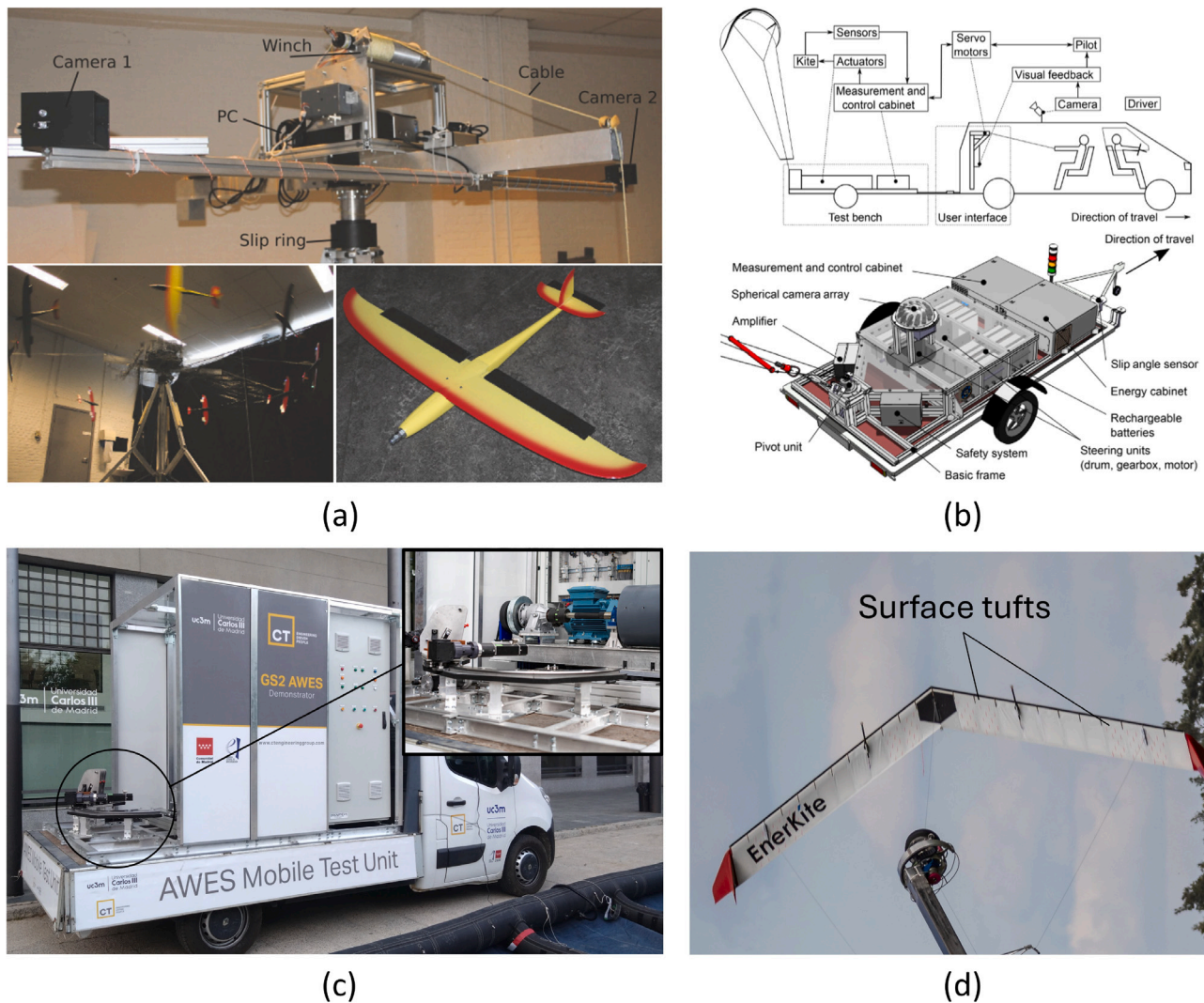


Fig. 8. Panel (a): laboratory setup based on a rotating arm developed in Geebelen et al. [188]. Panel (b): tow test setup mounted on a car trailer and developed in Hummel et al. [111]. Panel (c): ground-gen AWE machine developed by UC3M and the CT Engineering Group [191,192]. Panel (d): surface tufts attached to the EnerKite EK30 swept wing while being launched by the rotating system [44].

In parallel with experimental setups, an important effort was also dedicated to develop filters to estimate the state of the system from the measurements of the ground and onboard sensors. Filters are broadly divided into batch and sequential methods. An example of the former is the least-squares estimation, which involves fitting a model to a batch of measurements. This process may require significant computational resources, making it generally unsuitable for real-time applications. On the other hand, sequential methods, like the Kalman filter and its variants, can estimate the state vector in real time by optimally combining an observation model and a process model. Due to its extensive use in aerospace applications, the Kalman filter has also been mostly applied in AWE testing. For instance, three filtering algorithms based on a kinematic process model and focused on wing's position and velocity and of its velocity angle, also known as course angle, were presented and compared in Fagiano et al. [205]. An extended Kalman filter was developed and tested in an AWE simulation environment, combining range measurements from ultra-wideband radars with inertial readings from an IMU and using a sensor-driven kinematic process [206].

Unlike dynamic process models, kinematic equations are independent of the system mass, inertia, wing area and aerodynamic characteristics, among others. Moreover, these models do not include aerodynamic variables in the state vector that is key to perform aerodynamic

characterization. Precisely, this was the goal of work Schmidt et al. [65], that adapted an existing extended Kalman filter originally applied to power kites [207] for Magnus effect-based AWE systems. The aerodynamic lift and drag were included in the state vector, allowing to estimate afterward C_L and C_D as a function of the spin ratio parameter of the cylinder. A filtering scheme based on the unscented Kalman filter was developed to allow the joint estimation of wind conditions, aerodynamic parameters and system states [208]. In this filtering scheme, C_L and C_D were part of the state vector and its performance was tested with flight data of the EnerKite EK30. In addition to the kinematic vector of the kite and the bias of the sensors, the state vector of the flight path reconstruction algorithm for AWE systems of Ref. [195] also included three Markov vectors with the aerodynamic force and torque, the tether tension and the wind velocity. Designed as a first step towards the aerodynamic parameter identification of AWE systems using flight-test data and estimation before modeling techniques, the performance of the filter was investigated by using flight data from tests with two four-line LEI kites. Although the experimental setup included an onboard pitot tube for measuring the static and dynamic pressures, the work highlighted the importance of adding an air data boom with a high quality sensor for measuring the flow direction and magnitude [195]. An extended Kalman filter fed with measurements from

the ground station (line angles and their rates, traction force on the tether, and wind speed and direction a few meters above the ground) was used to study the aerodynamics of LEI and ram-air kites [209]. Experimental results of the lift coefficient and the aerodynamic efficiency as a function of the angle of attack were obtained. For the LEI kite, an atypical minimum for the lift coefficient was found and attributed to the flexible structure. Since the experimental results exhibited an important dispersion, adding a pitot tube for the in-situ measurement of the aerodynamic velocity was mentioned by the authors as a future improvement.

Other techniques different from Kalman filtering were useful for the aerodynamic system identification of AWE systems. For instance, the aerodynamic derivatives of the Ampyx 2nd generation PowerPlane were determined by means of time-domain system identification techniques using measurements from real flight tests [35,36]. The analysis was based on a multiple-experiment model-based parameter estimation algorithm that assumes a certain structure for the aerodynamic model of the aircraft, which included both aerodynamic forces and torques. Tether force, and from it the lift and drag, were estimated for a LEI kite using analytical and machine learning models trained with experimental data [197].

Building a reliable aerodynamic model from flight data does not only involve the estimation of the aerodynamic coefficients but also the instantaneous knowledge of the aerodynamic velocity vector of the aircraft. A step toward its accurate measurement is to obtain the wind speed vector at the kite's height to combine it with the kite absolute velocity by using Eq. (5). This was the selected approach in Ref. [210], that used a sonic wind profiler to measure the wind profile from 13 to 108 m above the ground with one point every 5 m. The wind velocity at the kite's height together with measurements of the tether tensions, among others, allowed to estimate the aerodynamic efficiency and the lift coefficient of a four-line LEI kite during figure-of-eight trajectories. Structural buckling phenomena for wind speed above certain threshold occurred during the test. The exact conditions for the buckling were difficult to predict, but pressure of the inflated leading edge and the bridle configuration were identified as the main drivers. The same aerodynamic properties were also investigated for the LEI kite of the 20 kW power system of TU Delft/Kitepower [97]. Such a system was equipped with a self-aligning pitot tube mounted on the bridle line system between the LEI kite and its control unit [117] [see panel (a) in Fig. 9]. Two flow vanes were used to measure two angles related to the attack and sideslip angles, thus allowing the in-situ measurement of the aerodynamic velocity vector, i.e., the airspeed, angle of attack and sideslip angle. Panel (b) in Fig. 9 shows the measured lift coefficient C_L as a function of the angle of attack and colored by the heading angle of the kite from Ref. [117]. It was also shown that the lift-to-drag ratio of the kite increases with the relative power setting and, for straight flight, the maximum ratio is reached at an angle of attack of 8° . Moreover, the experiments revealed the dependence of the aerodynamic characteristics of LEI kites not only with the angle of attack, as usual in rigid wings, but also on the level of aerodynamic loading that depends on the power setting. The authors pointed out the combination of the presented experimental setup with filtering techniques as a practical approach to increase the accuracy of the data.

Precisely, the combination of high-quality in-situ measurements of the aerodynamic velocity vector with filtering techniques was the basis of the experimental work of Ref. [57] at UC3M. The extended Kalman filter of Ref. [195] was adapted to incorporate the measurements of a multi-hole pitot tube that provided the aerodynamic velocity, the angle of attack and the sideslip angle. Instead of being mounted in the bridle line system following Ref. [117], the pitot was installed on a boom that was rigidly joined to the kites; which were a four-line LEI kite and a two-line rigid-framed delta kite. Panel (c) in Fig. 9 displays the rigid-framed delta kite with the boom, the pitot tube, and the onboard avionics. Unfortunately, the LEI kite flew most of the time in post-stall

conditions due to control limitations of the experimental setup, and the poor maneuverability impacted negatively on the data acquisition for the LEI kite. However, abundant data were obtained for the rigid-framed kite, which allowed to identify the lift, drag, and pitching moment coefficients as a function of the attack and the sideslip angles by using estimation before modeling techniques [57,211]. However, the identification of lateral-directional coefficients (force and torque) was not possible. Later analysis of the experimental data revealed hysteresis cycles of the lift and drag coefficient versus the angle of attack during figure-of-eight trajectories [61] [see panel (d) in Fig. 9]. In order to investigate such interesting feature deeper, the experimental setup was updated to incorporate surface tufts and an onboard camera. They provided experimental evidence of the periodic stall of the kite during the figure-of-eight trajectories, together with important aero-structural deformation at the phases with maximum aerodynamic loads [61]. A newer version of the UC3M-CT Engineering AWE machine, which is aimed at aerodynamic characterization among other uses, have been recently presented [212] and the latest state of the machine is shown in Fig. 8c. The tow setup developed in Hummel et al. [111] was also updated with onboard sensors, including a multi-hole pitot tube positioned far upstream of the kite's leading edge in Elfert et al. [213]. This low-cost sensor was custom-developed by using differential pressure flow meters between the central and the lateral holes of the tube, and calibrated in a wind tunnel. They found that the absolute velocity measured by the GNSS becomes an indirect reliable measurement of the airspeed as compared to the outputs of the multi-hole pitot tube during the tow tests with negligible ambient wind speed. This is an inherent feature of tow tests as compared to fixed testbeds, where the wind speed at the kite's height would also be required for this computation (see Eq. (5)).

4.3. Aerodynamic information for each type of wing

This section summarizes and discusses the relevant aerodynamic information predicted and measured with the numerical and experimental methods reviewed in Sections 4.1–4.2. This information is useful to optimize the aerodynamic design of the wings and for control [114,214] and power prediction purposes [47,72,97,125], among others. For instance, Vimalakanthan et al. [72] multiplied the total tension, as a projection of the lift, drag, inertial and gravity forces in the tether direction, by the longitudinal tether velocity to compute the instantaneous power. Haas et al. [125] used an actuator sector method to couple the aircraft dynamics with the LES model, being able to retrieve the generated power by ground-gen and fly-gen systems. Other works considered constant aerodynamic figures of merit (e.g., C_L/C_D) during the traction (reel-out), retraction (reel-in) and transition phases of ground-gen systems to estimate the power output along the generation cycles by using performance [47] or quasi-steady dynamic models [97].

A set of characteristic aerodynamic figures of merit have been selected, namely, wing area S , aspect ratio A , aerodynamic velocity V_A , zero-lift angle of attack α_0 , stall angle of attack α_{stall} , lift ($C_{L,stall}$) and drag ($C_{D,stall}$) coefficients at stall, minimum drag coefficient $C_{D,min}$, maximum-efficiency angle of attack $\alpha_{E,max}$, maximum efficiency E_{max} and reduced frequency k (as defined in Table 1). Table 3 shows the relevant aerodynamic information together with the type of wing and airfoil studied, and the method employed for a wide selection of works. For clarity, the works have been classified by the type of wing (LEI kites, ram-air kites, hybrid wings, fixed wings and rotary wings) and sorted in ascending year of publication. The figures that could not be retrieved from the cited works read “-” in the table. As noticed in past sections (e.g., Table 2), LEI, ram-air and fixed wings have been predominantly studied as compared to hybrid and rotary wings. A good balance between numerical and experimental methods have been employed in LEI kites, unlike in the rest of the wing types where numerical methods were predominant.

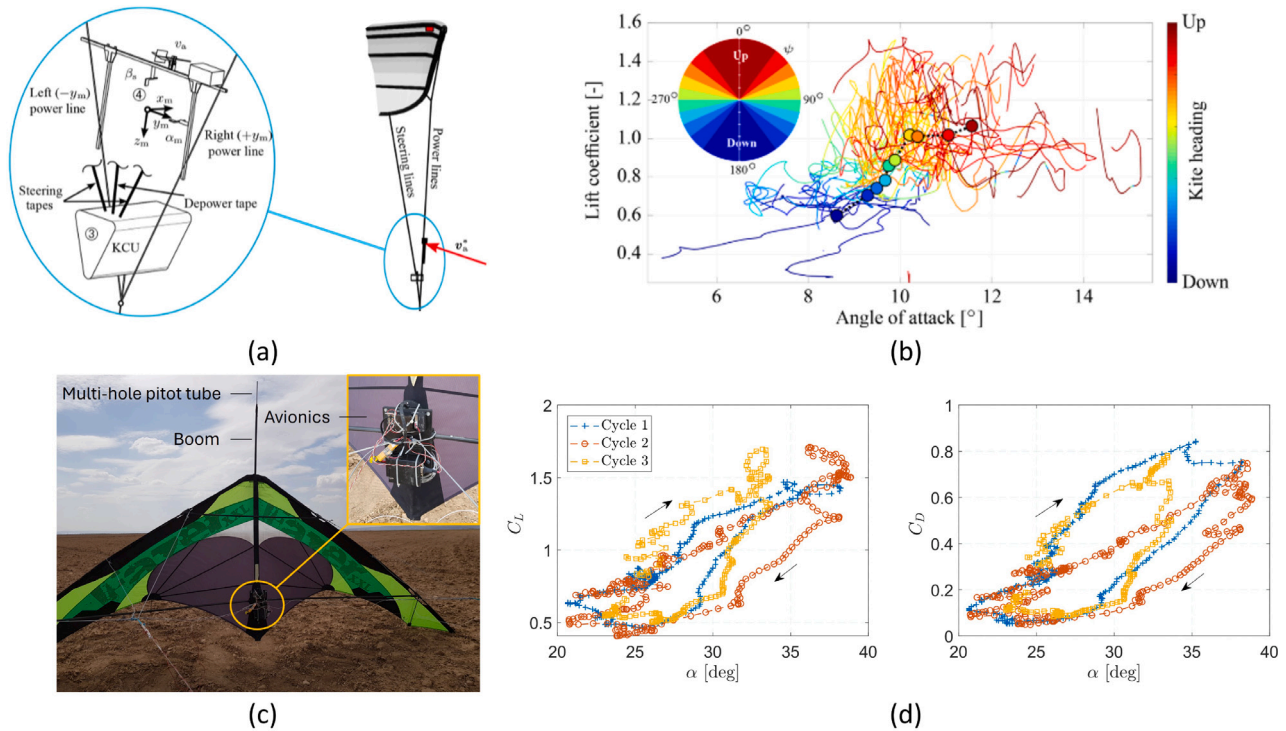


Fig. 9. Panels (a) and (b): experimental setup to measure the airspeed, angle of attack and sideslip angle of a LEI kite composed of two vanes and a pitot tube attached to the bridle lines, and experimental lift coefficient versus the angle of attack colored by the instantaneous kite heading in Oehler and Schmehl [117]. Panels (c) and (d): multi-hole pitot tube, boom and avionics onboard a hybrid delta kite in Borobia-Moreno et al. [57], and experimental lift and drag coefficients versus the angle of attack from Castro-Fernández et al. [61] estimated with the setup shown in panel (c).

Numerical methods – ranging from potential-flow approximations (lifting-line, vortex-lattice, panel and nonlinear vortex-step methods) to CFD (RANS and LES) – have been used to predict the aerodynamic performance of all types of AWE wings. Except for the vortex-step method, potential-flow tools cannot predict stall, providing a reasonable accuracy only for small enough angles of attack. Therefore, the stall figures (α_{stall} , $C_{L,stall}$, $C_{D,stall}$) read “N/A” for most of the potential-flow methods in Table 3. Lifting-line methods like the one developed in Leloup et al. [123] have been applied to ram-air kites, showing a very good match with the RANS computations from Maneia [215] in the linear region of the C_L versus α curve. To be able to capture the nonlinear region of this curve as well as accurate predictions of the C_D , modifications of potential-flow methods by including viscous data need to be performed, as done with the vortex-lattice method in Gaunaa et al. [131] (ram-air kite) and with the nonlinear vortex-step method in Ranneberg [208] (fixed wing) and Cayon et al. [50], Dupont [126] (LEI kite). The overall accuracy of the latter methods highly depends on the pre-computed 2D viscous data, normally calculated with viscous-inviscid and RANS methods. High-fidelity CFD tools predicted steady [40,77,78] and unsteady [61,144–146] flow separation in all the wing types, providing results for a broad range of angles of attack as shown in Table 3.

On the other hand, laboratory (wind tunnel) and flight testing were mostly applied but not limited to LEI kites. Most of the wind tunnel experiments were carried out under static conditions, whereas unsteady aerodynamic information was generally retrieved from flight tests. Some pioneering works on wind tunnel testing of kites [174,175] reported extensive databases of the aerodynamic coefficients of a variety of membrane kites. Likewise, a set of 2D wind tunnel experiments were reported in Bruining [180], den Boer [181], Babinsky [176]. They were not gathered in Table 3 for the sake of brevity. Other wind tunnel test campaigns focused on the static aerodynamic characterization of rigid LEI [182] and ram-air [216] kites by measuring the force and moment

coefficients as a function of the angle of attack and sideslip angle. Most of works on flight testing did not provide complete aerodynamic polars but only maximum and/or average values that have been labeled as “(max)” and “(av)”, respectively, in Table 3. Other works like Oehler and Schmehl [117], Schmidt et al. [209], Borobia-Moreno et al. [57] provided comprehensive results in terms of lift and drag coefficients of LEI and hybrid kites, but also highlighted the large dispersion of the experimental data. This means that there exist several values of the aerodynamic coefficient for the same angle of attack. The reasons for this dispersion were commonly associated to aeroelastic and unsteady aerodynamic effects. Indeed, among the different works that compare flight aerodynamic information with numerical computations, those applied to soft (LEI and ram-air) and hybrid kites remark the inability of the numerical tools to capture such large dispersion in the aerodynamic coefficients [61,77,136], unless fluid–structure interaction is included [50,62].

Although most of the aerodynamic data was available in the references listed in Table 3, key parameters such as aerodynamic efficiency, E , and drag coefficient, C_D , as a function of the angle of attack, α , were often missing, particularly for fixed-wing configurations. As discussed in Section 3.1, the aerodynamic efficiency is a crucial figure of merit in performance models used to predict the generated mechanical power. Another important aerodynamic design parameter is the aspect ratio, Λ . Typical values are around 3 for LEI and ram-air kites, while fixed wings exhibit values above 10. This parameter influences three-dimensional aerodynamic effects and, consequently, the attainable lift. To illustrate this, Fig. 10 shows the stall lift coefficient, $C_{L,stall}$, from Table 3 plotted against Λ for different wing types. An increasing trend of $C_{L,stall}$ with Λ is evident regardless of the wing type, most clearly for fixed wings due to their wider range of aspect ratios. In contrast, LEI and ram-air kites cluster at lower Λ and moderate $C_{L,stall}$ values, whereas hybrid kites, though less documented, generally show higher aspect ratios and lift coefficients than soft kites [55,59]. Finally, the

Table 3

Aerodynamic figures of merit for each type of AWE wing (LEI kites, ram-air kites, hybrid wings, fixed wings and rotary wings) extracted from a selection of numerical and experimental works (1/2).

Work	Airfoil	Method (st./unst.)	S (m ²)	A (-)	V_A (m/s)	α_0 (°)	α_{stall} (°)	$C_{L,stall}$ (-)	$C_{D,stall}$ (-)	$C_{D,min}$ (-)	$\alpha_{E_{max}}$ (°)	E_{max} (-)	k (-)
LEI kites													
Gohl and Luchsinger [129]	N/S	Vortex-lattice (steady)	36.1	4.4	5	-10	N/A	N/A	N/A	0.13	10	5.5	-
Buffoni et al. [138]	Clark-Y	RANS (steady)	6	2.7	20	-4	15	0.9	-	-	10	6.5	-
Fagiano et al. [114]	N/S	Flight test (unsteady)	12	0.8	-	-	-	0.85 (av)	-	-	-	5.3 (av)	-
Duport [126]	$D_{LEI}/c \approx 0.1$	Nonlinear vortex-step (steady)	4.2	6	-	-3	16	0.7	0.05	0.01	-	-	-
Behrel et al. [210]	N/S	Flight test (unsteady)	5	-	15	-	-	0.87 (max)	-	-	-	4.8 (max)	0.09
Hummel et al. [111]	N/S	Flight test (unsteady)	10	-	11.3	-	-	0.7 (max)	-	-	-	8 (max)	-
Oehler and Schmehl [117]	N/S	Flight test (unsteady)	25	3.1	20	-	10	1	-	-	5-10	5	0.08
Schmidt et al. [209]	N/S	Flight test (unsteady)	9	-	7	-	25 (max)	1.5 (max)	-	-	7	6	-
Viré et al. [77,78]	N/S	RANS (steady)	25	3.1	16.3	-4	17	1.3	0.16	0.05	-	-	-
Borobia-Moreno et al. [57]	N/S	Flight test (unsteady)	10	-	10	-	35	0.95	0.06	-	-	-	0.14
Cayon et al. [50]	N/S	Nonlinear vortex-step (steady)	25	3.1	-	-2	15	1.25	0.17	0.05	6.5	8.5	-
Van Spronsen [182]	N/S	Wind tunnel (steady)	25	3.1	-	-3	10	0.9	0.35	0.05	6	7.5	-
Ram-air kites													
Maneia [215]	Clark-Y	RANS (steady)	16	3.2	20.2	-5.5	18	1.1	0.18	0.01	0	26	-
de Wachter [52]	N/S	Wind tunnel (steady)	5.2	3.9	8	-	-	-	-	-	-	8	-
Gaunaa et al. [131]	NACA 64-418	Vortex-lattice (steady)	0.3	3.3	-	-7	16	0.9	0.085	0.01	-	-	-
Leloup et al. [123]	Clark-Y	Lifting-line (steady)	16	3.2	20.2	-6	N/A	N/A	N/A	0.01	-	-	-
Belloc [216]	NACA 23015	Wind tunnel (steady)	25	2.8	10	-1	17	0.85	0.07	0.02	-	-	-
Folkersma et al. [53]	N/S	RANS (steady)	160	1.9	7.9	-2.5	27	1.05	0.2	0.02	-	-	-
Thekens and Schmehl [54]	N/S	Panel method & Flight test (steady)	160	2.9	20	-5	N/A	N/A	N/A	0.01	3	17	-
Hybrid wings													
Borobia-Moreno et al. [57]	Single membrane	Flight test (unsteady)	1.9	-	15	-	40	1.4	1.25	0.1	-	-	0.03
Castro-Fernández et al. [62,136]	Single membrane	Vortex-lattice (unsteady)	1.9	7	15	16	N/A	N/A	N/A	0.1	35	7	0.02
Castro-Fernández et al. [61]	Single membrane	RANS (unsteady)	1.9	7	15	16	37	0.9	0.35	0.15	-	-	0.02
Fixed wings													
Ranneberg [127]	Delta (S1223)	Nonlinear vortex-step (steady)	14	3.5	-	2	24	1.55	0.16	0.03	-	-	-
Wijnja et al. [37]	NACA 0012	Lifting-line (steady)	-	18.7	-	-	23	3.1	-	-	-	-	-
Vimalakanthan et al. [72]	AP-3 airplane (multi-element)	RANS (steady/ unsteady)	12	12	10	-5	20	2.5	0.27	0.06	-	-	0.02
Benedetti and Veras [177]	Dynamically inflatable wing (-)	Wind tunnel (steady)	0.3	0.5	9	-	20	0.9	-	-	-	-	-
Haas et al. [125]	Fixed wing (SD 7032)	Lifting-line (steady)	310.1	12	12	-4	20.6	1.9	-	-	8.1	17	0.04
Kheiri et al. [143]	Rectangular wing (Clark-Y)	RANS (steady)	200.7	14.5	11.9	-5	15	1.35	0.15	0.02	-	-	-
Pynaert et al. [144,145,146]	Multi-MW airplane (-)	RANS (unsteady)	150	12.2	80	-15	20	1.6	0.35	0.09	-	-	0.02
Eijkelhof et al. [40]	Box wing (NACA 0012)	Panel method / RANS (steady)	0.2	5	37	0	18	0.9	0.22	0.02	-	-	-
Crismer et al. [152]	Multi-MW airplane (-)	LES (unsteady)	150	12.2	10	-	-	-	-	-	-	-	0.19
Rotary wings													
Vermillion et al. [70]	Altaeros Airborne wind turbine (-)	Flight test (steady)	-	0.7	5	10	30	-	-	-	30	1.7 (shell)	0.4
Deodhar et al. [187]	Airborne wind turbine (NACA)	Wind tunnel (steady)	-	-	0.3	-7	15	3	1.35	0.8	-	-	-
Saleem and Kim [141]	Airborne wind turbine shell (optimized)	RANS (steady)	-	-	10	-12	12	2 (2D)	0.03 (2D)	0.01 (2D)	5 (2D)	175 (2D)	-

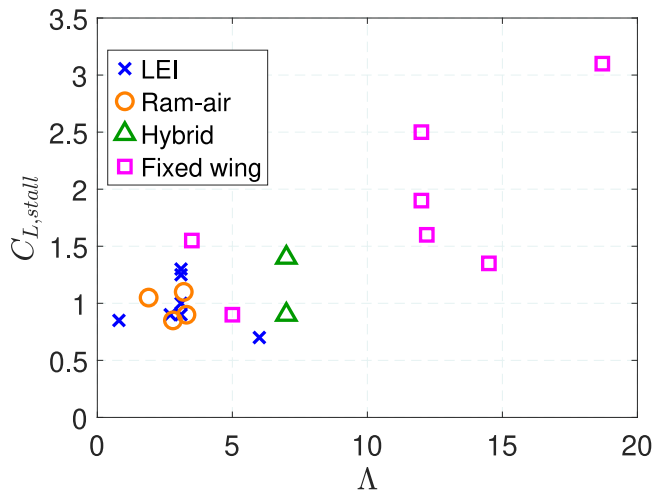


Fig. 10. Lift coefficient at stall $C_{L, stall}$ versus aspect ratio of the wing Λ from Table 3 with different markers for every type of wing.

reduced frequency, k , also compiled in Table 3, provides insight into aerodynamic unsteadiness: high k values denote stronger unsteady effects. This parameter is only reported in studies that explicitly address unsteady aerodynamics, which remain limited in the AWE literature. Reported values are typically low (~ 0.03) for hybrid and fixed wings and moderate (~ 0.1) for LEI kites. Comparable trends are found in commercial and pre-commercial systems (Table 1), suggesting that both quasi-steady and unsteady aerodynamic effects contribute to their operation [61].

Based on the information compiled in Table 3, a procedure to obtain the Aerodynamic Readiness Level (ARL) of each type of wing is proposed. The ARL is defined as an alphanumeric grade: Low (0–9 pts), Medium (10–19 pts) and High (20–30 pts). This grade is computed by adding up the points assigned to three criteria: (1) experimental data availability (5 pts for wind tunnel data availability, plus 5 pts for flight data availability), (2) fidelity of the numerical methods applied (3 pts for potential-flow models, plus 2 pts for nonlinear vortex-step models, plus 5 pts for CFD models), and (3) validation of numerical against experimental tools (5 pts for comparisons between numerical and wind tunnel data, plus 5 pts for comparisons between numerical and flight data). Moreover, the sub-criteria within criteria (1) and (2) (e.g., wind tunnel data availability) are weighted by $N_{i,w}/N_{i,max}$, with $N_{i,w}$ the number of works fulfilling a given sub-criterion (i) for the wing being evaluated (w) and $N_{i,max}$ the highest number of works fulfilling sub-criterion i for any type of wing in Table 3. Therefore, the ARL grade establishes the relative amount and quality of the numerical and experimental data obtained for each AWE wing. A summary of the ARL results is shown in Table 4. The ARL ranking following the proposed methodology in descending order is LEI (high, 25.5), ram-air (high, 20.5), fixed (medium, 16.5), hybrid (low, 7.7) and rotary (low, 4.16) wings. These results highlight that a good balance between numerical and experimental methods, as well as validation has been applied to LEI and ram-air kites. Fixed wings were well studied numerically but they partially lack of experimental data. Hybrid and rotary wings are under-characterized both numerically and experimentally and, hence, their low ARL. It must be noticed that the present ARL analysis has been solely based on the information given in Table 3, that was the best effort by the authors to collect relevant aerodynamic figures of merit in AWE. Other works lacking these data have not been considered in the analysis.

5. Aerodynamics in other AWE areas

Aerodynamics significantly influences various aspects of AWE systems, with dynamics and control, as well as fluid–structure interaction,

being the most prominent. In these areas, aerodynamics plays a critical role, closely interacting with the flight mechanics, control systems, and structural components of the AWE system, as illustrated in Fig. 11. This section examines the application and effectiveness of current aerodynamic knowledge and models in these domains, focusing particularly on numerical studies.

5.1. Aerodynamics in dynamics and control

Multiple numerical dynamic and control AWE models at different levels of fidelity have been proposed [24]. The simplest dynamic models, whether based on a point mass with an empirical turning law and quasi-steady approximations [14,15,114] or without these assumptions [218], proved to be effective for closed-loop control purposes. These models are fast but lack substantial physical representation since they do not consider the full attitude state of the kite and assume a straight and weightless tether, among other assumptions. On the contrary, higher degree-of-freedom models typically include the six degrees of freedom of the aircraft, a winch model and the tether at different levels of approximation, including tether segmentation into inelastic rods [219], quasi-static tether models [220] and spring–mass models [193,221]. They are based on classical (Newtonian) mechanics and naturally lead to non-minimal coordinates, which generally result in higher computational effort. For this reason, analytical mechanics was applied to AWE systems by developing efficient flight simulators for single- and multi-kite systems, yielding for instance the optimal control toolbox AWEbox [222–224]. Lagrangian kite simulators were also developed for one-line, two-line, multi-kite and rotary AWE systems and gathered in the open-source software LAKSA [194,217,225–227].

Either Newtonian or Lagrangian, dynamic models need an aerodynamic model to obtain the aerodynamic forces and moments on the aircraft and the tether at every time step of a dynamic simulation, as shown on the left side of Fig. 11. The aerodynamics becomes an essential building block in a dynamic simulation, since it greatly influences the motion of the aircraft and the power predictions. Table 5 gathers a large sample of the works on dynamics and control of AWE systems, classified by the type of aerodynamic model employed (columns) and the data or model the latter was based on (rows). An additional axis was added to the table by coloring in blue, orange, green and purple the works on ground-gen, fly-gen, both of the latter, and rotary AWE systems, respectively. Within the reviewed literature, four main methods to evaluate the aerodynamic coefficients were identified, and they are described in Sections 5.1.1–5.1.4. Six distinct sources of data to feed the aerodynamic models were found in the literature: empirical/heuristic data are obtained from real machines or reference values in the literature, analytical methods like the thin-airfoil and Prandtl lifting-line theories, potential-flow methods with steady (i.e., assuming that the flow is fully developed in every aerodynamic evaluation) or quasi-steady/unsteady (i.e., considering transient conditions) assumptions, and steady or unsteady CFD.

5.1.1. Constant aerodynamic coefficients

They are the simplest aerodynamic models by assuming either a constant aerodynamic efficiency E [15,232] or constant lift C_L and drag C_D coefficients independently [104,231]. These are typically used in simplified point-mass dynamic models and to estimate the tether aerodynamic drag [194,220]. In ground-gen systems, they commonly use different sets of coefficients during the traction and retraction phases [97]. As shown in Table 5, the works using this type of aerodynamic model estimated the aerodynamic coefficients by using empirical data from real AWE machines [97] or they proposed heuristic values [228].

5.1.2. Look-up tables

The evaluation of the aircraft aerodynamic coefficients from aerodynamic databases has also been extensively used in AWE simulators.

Table 4
Summary of the aerodynamic readiness level analysis for LEI, ram-air, hybrid, fixed and rotary wings.

	LEI kites	Ram-air kites	Hybrid wings	Fixed wings	Rotary
Criterion (1)	$5 \cdot 1/2 + 5 \cdot 6/6 = 7.5$	$5 \cdot 2/2 + 5 \cdot 1/6 = 5.83$	$5 \cdot 0/2 + 5 \cdot 1/6 = 0.83$	$5 \cdot 1/2 + 5 \cdot 1/6 = 3.33$	$5 \cdot 1/2 + 5 \cdot 1/6 = 3.33$
Criterion (2)	$3 \cdot 1/3 + 2 \cdot 2/2 + 5 \cdot 6/6 = 8$	$3 \cdot 3/3 + 2 \cdot 0/2 + 5 \cdot 2/6 = 4.67$	$3 \cdot 1/3 + 2 \cdot 0/2 + 5 \cdot 1/6 = 1.83$	$3 \cdot 3/3 + 2 \cdot 1/2 + 5 \cdot 5/6 = 8.16$	$3 \cdot 0/3 + 2 \cdot 0/2 + 5 \cdot 1/6 = 0.83$
Criterion 3)	$5 + 5 = 10$	$5 + 5 = 10$	$0 + 5 = 5$	$5 + 0 = 5$	$0 + 0 = 0$
ARL Grade	High (25.5)	High (20.5)	Low (7.7)	Medium (16.5)	Low (4.16)

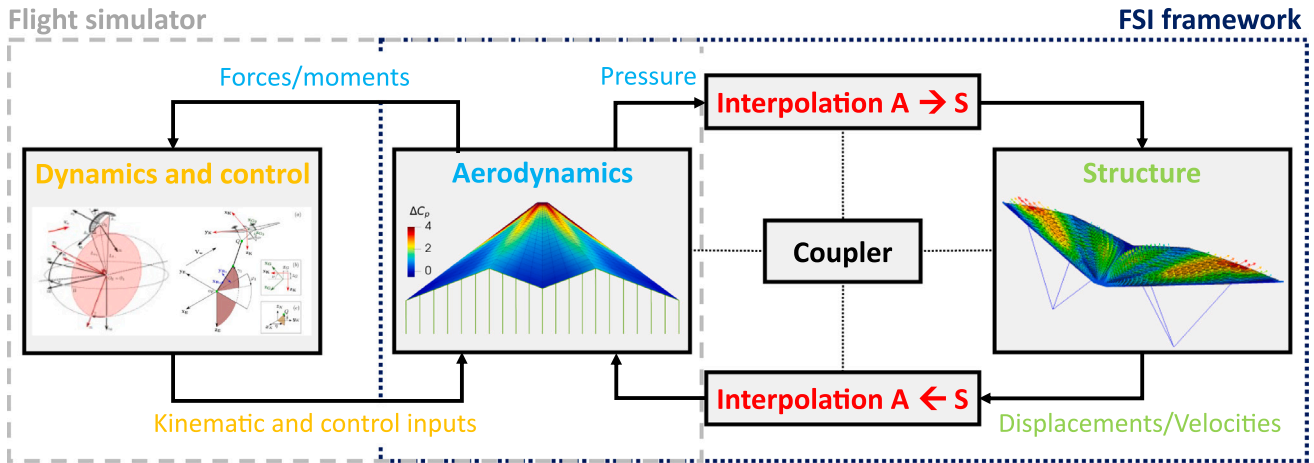


Fig. 11. Block diagram showing the interaction of the aerodynamics (center) with dynamics and control (left), and structure (right). The blocks are also grouped into a flight simulator and an FSI framework, showing the common dependence on the aerodynamic block.
Source: Illustrations were adapted from Sánchez-Arriaga et al. [217], Castro-Fernández et al. [62].

In these models, the aerodynamic coefficients are pre-computed either from empirical or numerical data as a function of different aerodynamic variables such as the angle of attack, sideslip angle and angular velocity. Other inputs like the airfoil thickness and camber were considered to account for the flexibility of LEI kites [252]. Then, single-variable [233] and multi-variate [85] interpolations were used to evaluate the aerodynamic coefficients for every set of input conditions. These databases were commonly fed with steady empirical [193, 234], potential-flow [218,253] and CFD [258,259] (including viscous-inviscid calculations [260,261]) data as shown in Table 5.

5.1.3. Constant aerodynamic derivatives

While keeping a low computational cost, the next level of approximation is achieved with models involving constant aerodynamic stability derivatives. They are similar to the linear aerodynamic models used for dynamic stability studies of conventional aircraft. However, they do not necessarily need to be linearized about a trimming condition, therefore, they can model aerodynamic nonlinearities like stall. In these models, the vectors of aerodynamic force F_A and moment M_A about the aircraft center of mass read

$$F_A = \frac{1}{2} \rho V_A^2 S C_F(\alpha, \beta, \omega, u_c), \quad M_A = \frac{1}{2} \rho V_A^2 S \begin{bmatrix} b & 0 & 0 \\ 0 & c & 0 \\ 0 & 0 & b \end{bmatrix} C_M(\alpha, \beta, \omega, u_c), \quad (6)$$

with C_F and C_M the force and moment coefficient vectors. The latter are generally a function of the angle of attack α , the sideslip angle β , the angular velocity of the aircraft ω and the aerodynamic surfaces deflections grouped into $u_c = [\delta_\alpha, \delta_\epsilon, \delta_r]^T$, which constitute the kinematic and control inputs of the aerodynamic model. Steady aerodynamic models only input α , β and u_c , whereas quasi-steady/unsteady methods also depend on ω . The aerodynamic coefficient vectors C_i , $i = F, M$ can be

generically expressed as

$$C_i = C_{i,0}(\alpha) + C_{i,\beta}(\alpha)\beta + \overline{C}_{i,\omega}(\alpha) \begin{bmatrix} b & 0 & 0 \\ 0 & c & 0 \\ 0 & 0 & b \end{bmatrix} \frac{\omega}{2V_A} + \overline{C}_{i,u_c}(\alpha)u_c, \quad (7)$$

where bold and overlined bold symbols represent vectors and matrices, respectively. A generic component of one of these vectors or matrices $C_{i,j}(\alpha)$, $j = 0, \beta, \omega, u_c$ can be expressed as an N th-order polynomial of α with constant coefficients as

$$C_{i,j}(\alpha) = \sum_{n=0}^N C_{i,j,n} \alpha^n, \quad (8)$$

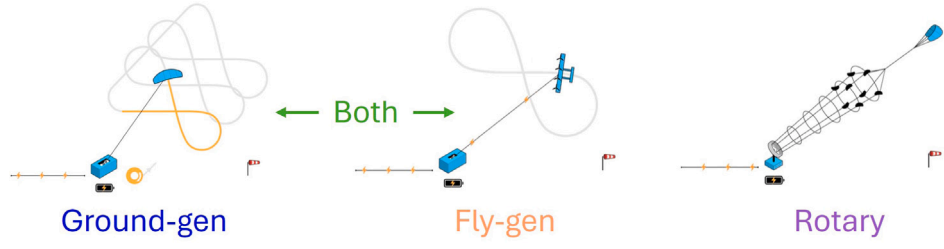
where $C_{i,j,n}$ are the constant coefficients of the aerodynamic model. In fact, the accuracy of these models strongly depends on the method used to estimate these coefficients. Interestingly, most of the aerodynamic models based on constant aerodynamic derivatives from the reviewed literature employed empirical [242,243] and heuristic [225,248] data to estimate these coefficients, as shown in Table 5. Only a few works employed analytical methods like the 2D thin-airfoil theory [250], or models based on potential flow [254,257] or CFD [74] to estimate them.

5.1.4. Aerodynamic numerical tool

The coupling of a dynamic simulator with an aerodynamic numerical tool has not been the preferred option in the literature to date, as seen in Table 5. The computational burden of evaluating a numerical aerodynamic model ranges from tens to thousands of times that of evaluating the analytical models described in Sections 5.1.1–5.1.3. However, they generally present a higher physical representation by including unsteady phenomena, wake induction effects, etc. To give some examples, an analytical model based on the blade element momentum theory was coupled with a dynamic model of a rotary AWE system [251]. For ground-gen and fly-gen systems, potential-flow tools implementing lifting-line methods [125], panel methods [133], the

Table 5

Works on numerical dynamics and control organized by the type of aerodynamic model (columns) used to evaluate aerodynamic forces and moments, and the source of data (rows) of the aerodynamic models. The blue, orange, green and purple colors correspond to works on ground-gen, fly-gen, both of these two, and rotary AWE systems. Illustrations were taken from Airborne Wind Europe [19].



Based on	Aerod. model	Constant aerodynamic coefficients	Look-up tables	Constant aerodynamic derivatives	Aerodynamic numerical tool
Empirical/heuristic data		Berra and Fagiano [228], Erhard and Strauch [14,15], Licitra et al. [229], van der Vlugt et al. [97], Zempoalteca-Jimenez et al. [230], Aull and Cohen [231], Trevisi et al. [98], Diwale et al. [232], Williams [220], Sánchez-Arriaga et al. [194].	Baayen and Ockels [233], Fechner et al. [193], Sánchez [234], Terink et al. [235].	Alonso-Pardo and Sánchez-Arriaga [236], Fernandes et al. [237], Gros and Diehl [222], Gros et al. [238], Kakavand and Nikoobin [239], Li et al. [240], Licitra et al. [241,242], Malz et al. [243], Rapp and Schmehl [244], Nikpoorparizi et al. [245], Li et al. [246], Salord Losantos and Sánchez-Arriaga [247], Sánchez-Arriaga et al. [217,225–227], Schutter et al. [224,248], Leuthold et al. [223].	-
Analytical model		-	-	Dadd et al. [203], Houska and Diehl [249], Williams et al. [219], Schutter et al. [250].	Tulloch et al. [251].
Potential flow (steady)		-	Groot et al. [252], Eijkelhof et al. [253], Eijkelhof and Schmehl [221], Cobb et al. [218].	Fagiano et al. [254], Van et al. [255].	Fasel et al. [133], Gohl and Luchsinger [129], Haas et al. [125].
Potential flow (quasi-steady/unsteady)		-	Echeverri et al. [27].	Williams et al. [256], Trevisi et al. [257].	Fonzi et al. [137].
CFD (steady)		-	Canale et al. [258], Orzan et al. [259], Todeschini et al. [39], Fuest et al. [260], Duda et al. [261].	Breukels [74], Bosch et al. [116,262], Rapp et al. [85], Bauer et al. [38,103].	-
CFD (unsteady)		-	-	-	Crismer et al. [152].

VLM [129] and the unsteady VLM [137] were coupled to high-degree-of-freedom simulators. In a recent work, the two-way coupling between a large-eddy simulation and a 6-degree-of-freedom dynamic simulator with a closed-loop controller was achieved. This was done using an actuator-line representation of the fixed-wing aircraft that acted as an interface between both frameworks [152].

5.2. Aerodynamics in fluid–structure interaction

The interplay between aerodynamics and structure is of great importance in AWE aircraft, particularly in soft and hybrid kites. Besides the inherent flexibility of these structures, the aerodynamic pressure is subject to significant variations induced by the kinematic conditions and control inputs, i.e., aerodynamic velocity, angle of attack, sideslip angle, powering control, etc. [61,145]. Systems that experience significant aeroelastic deformation in flight include ram-air and LEI kites (presenting spanwise deformation and local camber changes), many hybrid designs [132,133], and, to a lesser extent, large fixed-wing concepts where bridle/attachment geometry affects wing deformation [145]. Moreover, soft kites take advantage of asymmetric aero-structural deformations to turn [113,116,117] as discussed in Section 3.3. The literature shows more steady-state FSI work for LEI and hybrid kites, while ram-air kites remain under-studied despite evidence of local aeroelastic effects such as leading edge bumps and camber variations [53,54]. Due to the relatively low airspeed of AWE aircraft, studies on static and dynamic aeroelastic instabilities such as divergence and flutter are scarce in the AWE literature. Only Wijnja et al. [37] highlighted the strong influence of the bridle attachment points on the flutter speed of a large fixed-wing aircraft similar to Makani’s machine.





The right side of Fig. 11 illustrates a representative flowchart of an FSI problem in AWE, highlighting its key components: aerody-

namics, structural analysis, interpolation between aerodynamic and structural meshes (in both directions), and a coupler responsible for coordinating these modules. It also depicts the flow of information among them. Most of the works used structural solvers based on finite elements including beam, rod and shell elements to model fixed-wing structures [132,137,145] and either nonlinear membranes [53,54] or particle system models [50,51] for the canopy of soft kites. Being the aerodynamics the other half of the problem and the focus of this review paper, Table 6 gathers the works on FSI of AWE systems classifying them by the type of aerodynamic tool (columns) and the dimensions of the aerodynamic problem (rows), namely, two- (2D) and three-dimensional (3D). Works on LEI, ram-air, hybrid and fixed-wing kites have been colored in blue, orange, green and purple, respectively. For convenience, the aerodynamic solvers were divided into potential-flow and CFD tools, and each of them, subdivided into steady and unsteady.

Most of the effort until now has been put into the steady aeroelastic problem, i.e., solving the resulting steady-state structural shape and aerodynamic forces, through staggered coupling schemes similar to the one shown on the right side of Fig. 11. Only the structural displacements, not the velocities, are relevant inputs for the aerodynamics in steady FSI. Two-dimensional steady aerodynamic computations by using thin-airfoil theory [51] and RANS [74,75,116] were used to compute the aerodynamic pressure of several spanwise airfoils and, with them, reconstruct the complete pressure field over a LEI kite. To reduce the computational time and given the steady nature of the problem, some of these studies [74,75,116] pre-computed a database with RANS by sweeping the airfoil thickness, camber and angle of attack. The aerodynamic forces were interpolated as a function of these three inputs during the FSI iteration. This technique allowed to use high-fidelity aerodynamic data in the FSI problem avoiding the direct coupling between the structural and aerodynamic solvers. Other 2D

Table 6

Works on fluid–structure interaction organized by the type of aerodynamic model (columns) used to evaluate the aerodynamic forces, and the dimensions of the aerodynamic problem (rows). The blue, orange, green and purple colors correspond to FSI works on LEI, ram-air, hybrid, and fixed-wing AWE aircraft. Illustrations were adapted from Cherubini et al. [20].

		   		
Aerod. model → Dimensions ↓	Potential flow		CFD	
	Steady	Unsteady	Steady	Unsteady
2D	Poland and Schmehl [51].	-	Breukels [74], Breukels et al. [75], Bosch et al. [116], Thedens et al. [79].	-
3D	de Solminihac et al. [122], Cayon et al. [50], Thedens and Schmehl [54], Candade et al. [55,59], Castro-Fernández et al. [62], Wijnja et al. [37], Fasel et al. [132,133].	Duport [126], Fonzi et al. [137].	Folkersma et al. [53].	Pynaert et al. [145].

works like Thedens et al. [79] were only interested in the airfoil's reinforcement design of a ram-air kite and used a fast viscous-inviscid interaction solver (here considered a CFD method).

The majority of the steady FSI works used 3D aerodynamic methods to capture wing sweep, dihedral and wing-tip effects, among others. Engineering tools based on 3D potential flow like the lifting-line [37, 122] and nonlinear vortex-step methods [50,55,59] (see Section 4.1 for further details) combined with 2D viscous data from external CFD tools were applied to LEI and hybrid kites. These methods present a good balance between speed and fidelity since they can also capture stall and viscous effects. However, they only provide the spanwise lift distribution. For this reason, other works employed vortex-lattice and panel methods to solve the full pressure field over the wing [54,62, 132,133]. On the other hand, the application of 3D CFD tools in steady FSI has been limited up to now probably due to its high computational time. For instance, Folkersma et al. [53] used 3D RANS within an aero-structural framework of a ram-air kite and highlighted the importance of local aeroelastic phenomena such as leading-edge bumps and camber changes. Despite the significant advances in FSI knowledge in AWE through steady aerodynamic models in 2D or 3D, these methods are inherently limited to stationary conditions. They cannot fully capture the realistic kinematic effects and wind turbulence encountered during crosswind flight, underscoring the need for unsteady approaches.

To address these dynamic complexities, recent efforts are beginning to explore unsteady FSI frameworks, although the literature on unsteady FSI of AWE aircraft remains scarce. Examples of recent work include the use of the VLM method, either in a quasi-steady version [126] or an unsteady version [137], within an FSI module integrated in a dynamic simulator. Furthermore, in an effort to reduce the computational demands of unsteady FSI, Fonzi et al. [137] introduced a data-driven reduced-order aeroelastic model, demonstrated using a fixed-morphing-wing AWE system. Additionally, unsteady RANS equations coupled with a detailed finite element model [145] were employed to analyze the wing deformation of a similar aircraft during a prescribed circular trajectory. This work revealed significant asymmetric wing deformation during turning motions, which were shown to enhance the symmetry of the spanwise loading.

In summary, although several steady FSI investigations exist for LEI, ram-air, hybrid and fixed-wing AWE aircraft, the literature is dominated by one-way or staggered steady couplings and potential-flow approaches augmented with 2-D viscous data. These methods capture spanwise lift trends and quasi-static deformations but cannot reliably represent separated or strongly nonlinear unsteady aerodynamics that arise during crosswind maneuvers, gust encounters and rapid steering. Only a few studies implemented unsteady two-way couplings, and experimental validation of aeroelastic response across the full maneuvering envelope is sparse. Therefore, for deformable concepts (ram-air and LEI kites in particular), present aerodynamic

and FSI evidence is insufficient to guarantee robust predictions of cycle-averaged power output and aero-structural-based control, among others, without targeted unsteady FSI studies and dedicated validation campaigns.

6. Future avenues for AWE aerodynamics

The knowledge extracted from this review paper is used to perform a critical assessment of the readiness level and limitations of the aerodynamic methods applied to AWE wings, and identify the open questions, challenges and opportunities in AWE aerodynamics. The conclusions from this section may help readers identify research gaps in AWE aerodynamics where further contributions are needed.

6.1. Critical assessment of the current aerodynamic methods in AWE

The great variety of numerical and experimental aerodynamic methods, as well as the main aerodynamic information extracted from each method is found in Section 4. The aerodynamic characteristics of all types of AWE wings (LEI, ram-air, hybrid, fixed, rotary, etc.) were predicted with fast potential-flow tools ranging from basic lifting-line methods to slightly more complex vortex-lattice and panel methods. These tools were often benchmarked against both CFD tools [54,123, 131] and experimental data [40,136] demonstrating the ability to predict the linear part of the lift coefficient versus the angle of attack. However, they are unable to predict stall and they underestimate the drag coefficient due to the lack of viscous effects. From a purely aerodynamic point of view, this set of tools is not sufficiently accurate for a comprehensive aerodynamic analysis of a wing. Nonetheless, they become practical tools to be coupled with dynamic and control simulators [137] and structural solvers. Indeed, most of the fluid–structure interaction analyses performed in AWE considering the entire wing (3D FSI) used potential-flow models as shown in Table 6. This is a reasonable approach since most of the structural deformations are due to lift. To overcome some of these limitations, the nonlinear vortex-step methods include viscous effects by introducing external aerodynamic information of the airfoils, normally from 2D viscous-inviscid and RANS methods. They demonstrated a good aerodynamic performance as compared to existing tools like XFLR5 [128] and RANS [50]. Moreover, they have been successfully applied to 3D FSI in Candade et al. [55,59]. However, an important limitation of the nonlinear vortex-step method is the inability to provide chordwise pressure distribution, that for certain FSI cases may be critical. In conclusion, potential-flow tools do not generally predict fully representative aerodynamic results, but they become fast engineering tools for coupling in dynamic and control, and FSI tools, as long as the above limitations of the tools are considered.

Higher-fidelity methods such as RANS has been extensively applied to all types of AWE airfoils and wings uncovering relevant aerodynamic

aspects. Some examples are the recirculation region in the pressure side of LEI kites [76], the stall characteristics of box wings [40] and the dynamic stall in maneuvering hybrid kites [61]. Two-dimensional RANS data has been mostly used to feed nonlinear vortex-step methods [50,55,59] and to perform 2D FSI of flexible airfoils like those in LEI [75,116] and ram-air [79] wings. Three-dimensional RANS in its steady and unsteady forms has been the preferred method to predict both the underlying flow physics of entire wings (see Fig. 7) and the nonlinear aerodynamic polars (see Table 3). Several attempts to evaluate the accuracy of these methods against flight data of flexible AWE systems are not considered completely concluding because of a mix of unsteady aerodynamic and aeroelastic phenomena, and experimental uncertainties, making the flight data very disperse [61,77]. Only qualitative agreement with experimental results has been achieved by modeling periodic flow separation with unsteady RANS [61] and aeroelasticity by using a nonlinear vortex-step method (with 2D RANS data) [50]. Among the few studies on fixed wings where RANS methods were benchmarked against experimental data, Eijkelhof et al. [40] showed a remarkable agreement in the lift and drag coefficients of a box wing. Therefore, although RANS methods are well known to provide 2D and 3D representative aerodynamic results, attention must be paid to unmodeled effects like aeroelasticity and unsteady flight conditions to achieve a good accuracy. In addition, careful consideration of the computational time must be taken when applying this class of methods to dynamics and control, and FSI without any modeling reduction.

A large number of experimental studies have been conducted both in the laboratory (see Table A.7) and in the field (see Table A.8), most of which provide valuable insights for improving our understanding of AWE aerodynamics. However, some limitations and potential improvements are discussed hereafter. Most of the wind tunnel setups were equipped with either load cells or balance systems to measure the aerodynamic forces. Only some works measured the 6 components of aerodynamic force and moment as a function of the angle of attack and sideslip angle at the expense of constructing rigid models and removing the tethers from ram-air [216] and LEI [182] kites. Testing tethered models in wind tunnels highly constrains the control degrees of freedom because of the limited space and the inability to find equilibrium positions for some control settings. For this reason, most of the tests of tethered wings were limited to longitudinal control (pitch angle, power setting, etc.) providing the lift and drag coefficient versus the angle of attack curves [176,180]. Therefore, an important tradeoff between adding tethers constraining the testable aerodynamic conditions and removing them losing representativeness for a full aerodynamic characterization needs to be performed when testing AWE systems in wind tunnels. These setups were also very useful for measuring wing deformation of different types of wings such as sailwings [181], ram-air kites [52] and inflatable kites [263] through photogrammetry techniques providing relevant data for aeroelastic validation. However, barely none of them applied quality flow visualization techniques such as particle image velocimetry that has the potential of uncovering aerodynamic phenomena such as flow separation, tip-vortex effects, etc. under a controlled environment.

Although the number of experimental works on flight testing of AWE systems is large, most of them did not focus on aerodynamic characterization but on dynamic and control characterization and performance of AWE prototypes. However, they indirectly contributed to experimental aerodynamics by proposing a variety of sensors, and state and parameter estimation techniques, among others, as discussed in Section 4.2. The tests dedicated to in-flight aerodynamic characterization demonstrated that the knowledge of the aerodynamic velocity vector (airspeed, angle of attack and sideslip angle) is critical to accurately reconstruct the aerodynamic coefficients as a function of the aerodynamic conditions [57,117,213]. They also highlighted the importance of choosing the right estimation technique so that the aerodynamic coefficients come as outputs of the estimations [35,36,57,209]. However, a common characteristic of most of these works is the high dispersion exhibited by the aerodynamic coefficients measured in flight, identifying for instance several lift coefficients for the same

angle of attack. There is lack of consensus on the origin of this dispersion mainly because every AWE system may be subject to different phenomena such as aeroelasticity, unsteady aerodynamics induced by crosswind maneuvers, wind turbulence, etc. Indeed, a way of characterizing these phenomena could be by extending the capabilities of current setups by including for instance accelerometers and strain gauges to measure structural deformations, and pressure taps and flow-visualization sensors to locally characterize the flow and pressure fields. In conclusion, in-flight aerodynamic and aeroelastic characterization is a critical area in AWE and further research is required to reach a better understanding of the phenomena and to validate numerical methods.

6.2. Open questions and challenges

Great advances in numerical aerodynamic modeling (Section 4.1) and experimental aerodynamic characterization (Section 4.2) have been made in the last 25 years by the AWE community, allowing for a deeper understanding of AWE aerodynamics. However, there are still several open questions and challenges to be addressed in the short and midterm. The scale-up problem, which is probably one of the most important, has been discussed in several studies together with the levelised cost of energy [264,265]. In this respect, some lessons can be learned from conventional wind energy. The first electricity-generating wind turbine with a power of about 4 kW was developed in 1883. Almost 50 years later, they reached 100 kW and the first megawatt-scale wind turbine was connected to the local electrical distribution system in 1941. Although advances were also made on the aerodynamic efficiency, such spectacular scaling of the power was possible by increasing the size of the machines. Important structural, aerodynamic, and aeroelastic challenges were faced like finding the balance between blade length, weight and aerodynamic performance while avoiding catastrophic aeroelastic instabilities [266]. Currently, the most powerful prototype is able to produce more than 15 MW. On the other hand, AWE took momentum in the early 21st century and has reached nowadays a good level of maturity for technologies ranging 100–200 kW in about 25 years. Following the path of wind turbines, a logic reasoning suggests that to become a competitive on-grid solution, AWE systems will likely scale up to the megawatt-scale by increasing the system size. This is in fact the strategy followed by Skysails Power, which certified the power curve for its PN-14 AWE prototype in 2024 [267]. The datasheet of its first product Venyo, which is based on the PN-14, shows a rated power of 200 kW for kite areas within the range 120–180 m². The datasheet of its second product Kyo mentions a rated power of 450 kW and a kite area of 300–450 m². The company announces in its website a third product named Fujun with a rated power of 1.3 MW. The use of giant parafoils to pull ships that produce electric power using hydraulic turbines has been also discussed as a technical solution to reach the MW range [268].

The aero-structural scaling must be carefully analyzed principally in soft and hybrid kites which present large aeroelastic deformations, as foreseen in the early work by Felker [269]. A key question that would need to be solved is whether current concepts like LEI and ram-air kites could cope with the higher aerodynamic and bridle forces while keeping an aerodynamically efficient shape. For this reason, the fluid structure interaction physics and tools must be further investigated principally in ram-air kites, as highlighted by the low number of works on FSI in Table 6.

As discussed in Section 5.1, current dynamic and control tools use simple and fast aerodynamic models based on constant aerodynamic coefficients, look-up tables or constant aerodynamic derivatives. Numerical aerodynamic tools have been scarcely coupled with flight simulators. Based on these two observations, two questions arise: would the two-way coupling between dynamic and aerodynamic computational tools add significant physical representation as compared to the current simple aerodynamic models? Is it possible to develop aerodynamic tools that are both efficient and accurate enough to enable

feasible implementation of this coupling? The latter presents several challenges like balancing the computational cost and fidelity of the aerodynamic tool, using larger time steps in the dynamic simulation (e.g., using models based on inelastic tethers that remove the fast longitudinal waves along the tether) or using different time steps for the dynamic time integration and the update of the aerodynamic forces and moments.

Another challenge linked to the previous paragraph is the validation of the aerodynamic tools. As highlighted in Section 4.2, and although there are some exceptions [35,36,57,184], most of the experimental work in wind tunnels and flight tests were restricted to the analysis of variables related to the longitudinal components of the aerodynamic force, i.e. lift and drag coefficients and the efficiency. Therefore, there is a lack of experimental data about the lateral force component and the aerodynamic torque of fixed wings, and LEI and ram-air kites. Indeed, one of the most critical lessons learned by the Makani team shared after the project termination was the gap between simulation predictions and experimental data [28]. Nearly every flight test was used to improve the aerodynamic and dynamic models. The challenge of producing data for numerical tool validation is inevitably linked to the challenge of improving AWE experimental setups. The in-situ measurement of the aerodynamic velocity vector is essential, but high-quality multi-hole pitot tubes are expensive and delicate. Finding reliable and robust solutions to measure the angle of attack, the sideslip angle and the airspeed in flight tests is certainly a challenge with a deep impact on AWE aerodynamics.

Unsteady aerodynamic phenomena induced by the figure-of-eight trajectories of some AWE systems and the turbulence of the incoming wind is another important field of research that remains almost unexplored. Indeed, the characteristic reduced frequencies of the AWE aircraft shown in Section 2 (Table 1) indicate that a combination of quasi-steady and unsteady effects is likely to occur in most of them. Some experiments [57,61,117] reported evidence of mixed unsteady aerodynamic and aeroelastic effects during crosswind maneuvers. Unlike experiments, computational frameworks allow isolating and quantifying these effects. For this reason, realistic unsteady kinematic conditions, either experimentally estimated or simulated with a dynamic model, were considered in some aerodynamic simulations [58, 125,136,144–146,152] observing unsteady phenomena like dynamic stall or periodic variations of the kite aerodynamic coefficients. Unsteady effects induced by the wind turbulence while flying crosswind trajectories in closed loop were also reported [125,152]. Nevertheless, it is unclear what is the relative importance of these unsteady phenomena as compared to other effects such as asymmetric wing deformation in fixed-wing aircraft [145] and large aero-structural coupling in LEI [50,51] and ram-air [53,54] kites. Moreover, unsteady effects may be different in every AWE system since, as shown in Table 1, they present different characteristic parameters. Thus, further research effort is still required for a complete understanding of unsteady aerodynamic phenomena in AWE.

Another topic that remains partially open is the importance of aerodynamic induction, i.e., the slow-down of the incoming wind caused by the AWE aircraft itself and/or by others in the same AWE farm. Although numerous analytical [5,100–102] and numerical [125,134, 142,143] aerodynamic studies have quantified induction effects, there remains a lack of consensus on how induction influences the power production of various AWE architectures (e.g., single-kite and multi-kite systems) and farm layouts. Additionally, the relevant direction in the evaluation of the induction velocity remains an open question.

6.3. Opportunities

At the current state of development, the AWE field is still full of opportunities for the research and industrial communities to innovate. A remarkable opportunity arises due to the general lack of aerodynamic optimization of current 2D airfoils and 3D wing geometries

(see Section 2) mostly featured by soft kites. LEI and ram-air kites based their designs on already existing surfing and paragliding kites, respectively. While this approach enabled rapid development and significant scaling of their wings, these designs may be aerodynamically suboptimal. Some examples of aerodynamic inefficiencies are the well-known large recirculation bubble behind the leading-edge tube on the lower surface of LEI airfoils even at low angles of attack [76–78] (see Fig. 7c) and the generally low aspect ratio of ram-air kites which leads to undesired aerodynamic 3D effects [53]. These effects globally reduce the aerodynamic efficiency, E , which was shown to be an essential parameter to maximize the power production (see Section 3.1).

Artificial intelligence (AI) and data-driven techniques are increasingly transforming scientific and technological fields. In areas related to AWE systems, AI has made notable contributions to enhancing aircraft performance [270], advancing computational fluid dynamics [271], and improving experimental techniques [272]. However, their application to AWE aerodynamics remains limited, presenting a clear opportunity to generate new insights and develop innovative tools. Understanding and modeling the aerodynamics of an AWE system by collecting either numerical or experimental relevant data to train an AI-based algorithm could bring new knowledge and tools to the field. For instance, surrogate aerodynamic models that preserve most of the physical representation at a much lower computational cost than the full model could be built and used for example in dynamic simulators or FSI frameworks. As an example, the loads over an offshore wind turbine were estimated with a surrogate model trained with noisy data in Singh et al. [273]. In addition to modeling aerodynamic forces and moments, crucial local-scale aerodynamic insights – such as flow and pressure field reconstruction – could be derived using minimal data, as demonstrated in other fluid mechanics problems [274–276]. For instance, Moreno Soto et al. [276] used physics-informed neural networks to obtain a time-resolved flow characterization based on non-time-resolved measurements. It has also been proposed to use AI to accelerate CFD [277]. This is done by using a deep learning framework to establish a correction between a low-cost coarse-grid simulation and a costly fine-grid simulation. These authors showed that such strategies can lead to significant savings in computational time while accurately representing the most relevant features of the flow. The aerodynamics of AWE would benefit from such techniques, since inexpensive computation is a requisite in many applications. The control of aerodynamic variables by using machine learning techniques has also been studied numerically [278–280] and experimentally [281,282] in the non-AWE literature. All of these works highlighted the difficulty of finding model-based control techniques due to the inherent chaotic nature of turbulent flows and, instead, they proposed machine learning control. Interesting applications for active flow control in cylinders demonstrated drag reductions up to 20% [278,280]. These applications and methodologies share clear synergies with Magnus effect-based AWE systems, but could in principle be applied to other AWE aircraft in the near future.

The large number of testbeds and full-scale AWE machines, together with the software developed to gather and analyze the experimental data, present interesting opportunities due to their field-testing capability. Unlike wind and water tunnels, they allow for the testing of full-scale aircraft without wall effects. These infrastructures are ready to be used for doing basic research on AWE systems and increase our knowledge on aerodynamic and aeroelasticity, while they still have room for improvement. For instance, some ideas to complement the set of sensors of actual testbeds and improve the data related to aircraft aerodynamics are LIDAR sensors, pressure taps to reconstruct the pressure field, multi-hole pitot tubes, on-board load cells to measure the tension force seen by the aircraft, tufts and camera systems, and extensometers to measure structural deformation. The latter are particularly interesting to gather experimental data to validate FSI tools, mainly those applied to LEI and ram-air kites that show larger deformations. To the best of our knowledge, the flow and pressure fields were never reconstructed by using onboard sensors, and they have the potential

to uncover relevant aerodynamic phenomena including separation and flow unsteadiness.

AWE experimental infrastructures also open interesting opportunities for non-AWE aerospace systems, such as airplanes and UAVs. Low-scale models are normally tested in wind and water tunnel facilities to reduce testing costs. However, reaching aerodynamic and structural similarity in the models is difficult and testing dynamic maneuvers in the wind tunnels is also troublesome. AWE testbeds could become a suitable facility for these systems, as demonstrated in Healy et al. [190], where indoor tethered flight testing was performed to characterize the dynamic and aeroelastic behavior of a UAV. Obviously, the conditions of the flight testing are not as controlled and repeatable as in the laboratory, but much bigger models can be used because AWE testbeds and machines can easily handle forces up to several tons. This is certainly an advantage to reach structural similarity. The unpredictable character of the wind could be balanced by a good selection of on-ground and on-board sensors.

7. Conclusions

The wind power density at high altitudes (above 300 m) is a valuable resource driving the advancement of AWE technology for sustainable electricity generation. This review has highlighted significant progress in the aerodynamics of this emerging renewable energy technology, spanning areas such as numerical modeling and experimental testing. These advancements have directly impacted a wide range of topics, including dynamics, control, performance, structure, and safety. Collectively, these efforts have contributed to the development of the AWE sector, which today offers fully autonomous systems with rated power exceeding 100 kW. Although some concepts have reached a higher maturity and have been able to demonstrate higher power production in a relatively short time, there are still a high diversity of AWE architectures and aircraft. Research on aerodynamics and aeroelasticity is needed to uncover the best concepts to operate in the MW range.

This work has organized the information of more than 280 references, partially or directly related to AWE aerodynamics, with the goal of improving our current understanding of the state of the art and identifying gaps and open challenges that can impact on the development of the technology. The discussion about the impact on basic aerodynamic features of the type of AWE aircraft (fixed-wing, non-rigid, hybrid and rotary), the type of 2D airfoils (inflatable, ram-air and rigid single- and multi-airfoil configurations), the operation modes (ground-gen, fly-gen and rotary) and the control strategies (aerodynamic surfaces, hanging control pod and ground-based), revealed the wealth of the topic. Indeed, the broad range of aerodynamic domains covered by AWE systems was quantified by constructing some characteristic non-dimensional aerodynamic parameters of selected commercial and pre-commercial AWE machines.

In terms of numerical aerodynamic research, one of the main conclusion is the important body of literature that is nowadays available based on potential-flow, like the lifting-line and VLM methods, RANS and LES. They represent valuable knowledge for the development of future AWE machines. Most of the works assumed steady conditions, and although there are some exceptions, quasi-steady and unsteady aerodynamics remains an almost unexplored field of research. Since highly dynamic crosswind maneuvers and wind turbulence can trigger unsteady aerodynamic phenomena, the topic is identified as one of the targets for the next years. As shown by the review work, the great variety of experimental setups for AWE systems that were developed in the last years can certainly play an important role to untangle this and other open topics in aerodynamics. Such a statement is supported by the large variety of AWE aircraft (ram-air, LEI and inflatable kites, fixed wings and buoyant airborne turbines), that were successfully tested in laboratory facilities, like wind and water tunnels, and outdoor facilities like ground-fixed and tow testbeds. This review has shown how both types of facilities have progressively advanced, not only through an

increase in the number and quality of sensors but also through the enhancement of filtering algorithms used to fuse experimental data, providing more accurate estimations of system states and aerodynamic coefficients (aerodynamic parameter identification). We have also collected aerodynamic data from numerical and experimental studies, and classified it depending on the type of wing. This has allowed to propose a quantitative aerodynamic readiness level analysis, based on numerical fidelity, experimental data availability, and validation. The analysis has shown that LEI and ram-air kites exhibit the highest aerodynamic maturity, with fixed wings lagging somewhat behind while hybrid, and rotary wings remain clearly less developed.

Finally, the review has assessed the degree of application of the reviewed aerodynamic methods and knowledge in important AWE areas like dynamics and control, and fluid–structure interaction. It was found that nowadays dynamics and control tools are mainly based on fast and low-fidelity aerodynamic models to compute the total forces and moments on the aircraft and tethers. On the other hand, fluid–structure interaction analysis requires the spanwise and/or chordwise pressure distribution, and 2D and 3D aerodynamic tools, at different levels of fidelity, have been two-way coupled with structural solvers. It can be said that achieving the right balance between fidelity and computational cost of the aerodynamic tools applied to dynamics and control is one of the most important challenges in this area. The list of challenges and opportunities in AWE aerodynamics may be helpful to steer the research and to assist the development and progress of the fast-growing AWE field.

CRedit authorship contribution statement

Iván Castro-Fernández: Writing – original draft, Visualization, Data curation. **Gonzalo Sánchez-Arriaga:** Writing – original draft, Funding acquisition, Conceptualization. **Manuel García-Villalba:** Writing – original draft, Conceptualization.

Declaration of competing interest

The authors declare the following financial interests/personal relationships which may be considered as potential competing interests: Gonzalo Sanchez Arriaga reports financial support was provided by State Agency of Research. If there are other authors, they declare that they have no known competing financial interests or personal relationships that could have appeared to influence the work reported in this paper.

Acknowledgments

This work was carried out under the framework of the Kite2Grid project with reference PID2022-141520OB-I00 and funded by MCIN/AEI/10.13039/501100011033/FEDER, EU. The authors thank the AWE companies Kitekraft, SkySails Power, EnerKite, Wind Fisher, Kitepower and someAWE for providing images and data of their machines, and Prof. Roland Schmehl for valuable comments on an earlier version of the manuscript. The support of Prof. Chunlei Charles Liang is gratefully acknowledged. The authors acknowledge TU Wien Bibliothek for financial support through its Open Access Funding Programme.

Appendix. Survey of works on experimental aerodynamic characterization

This appendix presents a survey of experimental works on aerodynamic characterization of AWE aircraft performed in the laboratory (Table A.7) and in flight (Table A.8). The tables identify the type of testing facility and wing, together with the sensors, actuators, system parameters during the testing and main goal for each work.

Table A.7

Works on laboratory aerodynamic testing of AWE wings or close to them identifying the laboratory facility, wing type, sensors, system parameters (i.e., design parameter or variable varied in the tests) and main goal.

Year	Work	Facility	Wing	Sensors	System parameters	Goal
1951	Jackson [178]	Wind tunnel	Cody kites	Force sensors and lateral robot camera	Bridle geometry and wind speed	Measure lift and drag
1967	Rogallo [174]	Wind tunnel	Flexible wings	Force sensors	Wing configuration	Measure maximum lift-to-drag ratios
1970	Naeseth [175]	Wind tunnel	Parawings	Load cells	Wing geometry	Measure maximum lift-to-drag ratios
1979	Bruining [180]	Wind tunnel	2D rigid sailwings	Balance system, pitot-static tube and pressure sensors	Leading-edge tube position, angle of attack and wind speed	Influence of a tubular spar on lift and drag
1980	den Boer [181]	Wind tunnel	2D flexible sailwings	Photogrammetry and pressure sensors	Slack of the sail, angle of attack and wind speed	Influence of slack of the sail on lift and drag
1999	Babinsky [176]	Wind tunnel	2D paragliders	Balance system and pressure taps	Angle of attack and wind speed	Measure lift and drag
2008	de Wachter [52]	Wind tunnel	Ram-air kite	Photogrammetry, laser scanning, load cells, thermography and digital inclinometer	Bridle geometry (brakes), angle of attack and wind speed	Obtain wing deformation and aerodynamic performance
2013	Bormann et al. [87]	Wind tunnel	Ram-air kite	Load sensors	–	Load analysis
2013	Geebelen et al. [188]	Rotating arm	Fixed wings	Stereo vision system, IMU and encoders	Ailerons and elevator position	Test advanced estimation and control techniques
2014	Vermillion et al. [186]	Water channel	Buoyant airborne turbines	Load cells, and side and top waterproof cameras	Inertia properties	Dynamic characterization of buoyant airborne turbines
2015	Scupi et al. [150]	Wind tunnel	Rigid ram-air kites	Balance system	Angle of attack and sideslip angle	Measure aerodynamic forces in crosswind conditions
2017	Deodhar et al. [187]	Water channel	Buoyant airborne turbines	Three high-speed cameras and microload cells	Inertia properties and length of the three tethers	Dynamic and aerodynamic characterization of buoyant airborne turbines
2018	Wijnja et al. [37]	Wind tunnel	Fixed wings	Airspeed sensor	Bridle configuration and wind speed	Aeroelastic analysis
2019	Zalduogui [179]	Wind tunnel	Ram-air kites	Balance system, and front and side cameras	Anhedral angle or the wing, bridle geometry (brakes) and wind speed	Measure aerodynamic coefficients
2021	Benedetti and Veras [177]	Wind tunnel	Inflatable wing	Inner-outer differential pressure taps	Angle of attack and wind speed	Local and integral aerodynamic characteristics
2022	Healy et al. [190]	Spherical pendulum	Fixed wings	Angle of attack and sideslip vanes, pitot-static probe, IMU and camera on the tailplane	Flared folding wing tips, angle of attack, sideslip angle and wind speed	Dynamic and aeroelastic behavior
2023	Firdich [89]	Wind tunnel	Fixed wing	Balance system and smog probe	Pitch and yaw angles, wind speed and rotor configuration	Aerodynamic characterization of the fixed wing and rotors
2024	Desai et al. [263]	Wind tunnel	Inflatable kites	Stereo photogrammetry, force and moment sensors and wake rake	Fabric material, tether attachment configuration and wind speed	Experimental database for aeroelastic model validation
2024	Van Spronsen [182]	Wind tunnel	LEI kite	Six-axis balance system	Angle of attack, sideslip angle, wind speed and turbulence generation configurations	Aerodynamic characterization through force and moment measurements

Table A.8

Experimental AWE works related to flight aerodynamic testing identifying the testing facility, wing type, sensors and estimators, actuators, and main goal.

Year	Work	Facility	Wing	Sensors and estimators	Actuators	Goal
2005	Stevenson et al. [200], Stevenson and Alexander [201]	Circular-flight testbed	Soft kites (3.4 m ²)	Speed sensor and line loads	Manual steering	Circular flight testing of kites
2010	Dadd et al. [202,203]	Tow testbed	Ram-air kites (3 m ²)	Load cells, line-angle sensors, wind transducers and side camera	Manual steering	Measure static and dynamic kite performance
2010	Breuer and Luchsinger [204]	Tow testbed	Tensairity inflatable kites (11 m ²)	Load cells, line-angle sensors and wind station	No steering (constant-length single tether)	Structural and aerodynamic characterization of custom-made tensairity kites
2013	van der Vlugt et al. [47]	Fixed ground-gen	LEI kite (14-25 m ²)	IMU, GNSS receivers, encoders, potentiometers, pitot tube, wind station and load cells	Kite control unit and drum-generator	Design and performance characterization of a ground-gen prototype
2013	Fritz [198]	Fixed ground-gen	Ram-air kites	–	Kite control unit, drum-generator and launch/retrieval mast	Testing of a functional ground-gen prototype
2013	Milanesi et al. [48]	Fixed ground-gen	Ram-air kites (20 m ²)	IMU, GNSS receivers, wind stations, encoders, line-angle sensors, load cells and ammeters	Two-line ground control unit (drums) and drum-generator	Design and testing of a functional ground-gen prototype
2013	Ruiterkamp and Sieberling [199]	Fixed ground-gen	Fixed wing (3 m ²)	–	Flaps, ailerons, elevator, rudder and drum-generator	Preliminary test results of a ground-gen system
2014	Fagiano and Marks [110], Fagiano et al. [205]	Fixed testbed	LEI kites (6-15 m ²)	IMU, GNSS receiver, onground anemometer, load cells and line-angle sensors; Kalman filtering	Three-line ground control unit (linear actuators)	Test filtering algorithms and control characterization
2013	Ranneberg [208]	Fixed ground-gen	Ram-air (12.8 m ²)	LIDAR system (wind speed at kite's height) and accelerometers; unscented Kalman filter	Three-line ground control unit (drums) and generator	Joint estimation of wind conditions, aerodynamic parameters and system states
2017	Saraiva et al. [207]	Fixed testbed	Ram-air (3 m ²)	Line-angle sensors and load cell; extended Kalman filter	Steering and de-powering servomotors	Extended Kalman filter and closed-loop design
2017, 2019	Licitra et al. [35,36]	Untether-ed flight	Fixed wing (3 m ²)	IMU and pitot tube	Flaps, ailerons, elevator and rudder	Aerodynamic parameter identification of a fixed wing
2018	Borobia et al. [195]	Fixed testbed	LEI kites (10-13 m ²)	IMU, GNSS receiver, pitot tube, load cells, distance sensors; extended Kalman filter	Manual steering	Flight path reconstruction and aerodynamic characterization
2018	Hesse et al. [196]	Fixed testbed	LEI kites (10 m ²)	IMU, line-angle and length sensors, load cells, vision motion tracking sensor; extended Kalman filter	Two-line ground control unit (drums)	Visual motion tracking and sensor fusion
2018	Behrel et al. [210]	Fixed and boat-based testbed	LEI kites (5 m ²)	3D and 1D load cells, encoders, anemometers and wind profiler (13–108 m)	Three-line ground control unit (winches)	Estimation of aerodynamic efficiency during figure-of-eight trajectories

(continued on next page)

Table A.8 (continued).

2019	Hummel et al. [111]	Tow testbed	Membrane kites (10 m ²)	Line-angle sensors, load cells and magnetic rotary sensor	Three-line ground control unit (drums)	Dynamic and aerodynamic characterization of tethered wings
2019	Beaupoil [66]	Fixed rotary ground-gen	Rotary system (5.9 m ²) + lifting kite (4.6 m ²)	Load cells	Brakes and generator	Practical experiences with a rotary ground-gen prototype
2019	Oehler and Schmehl [117]	Fixed ground-gen	LEI kite (25 m ²)	IMU, GNSS receivers, relative-flow sensor (pitot tube and vanes system) and load cells	Kite control unit and drum-generator	Aerodynamic characterization of soft kites
2020	Rushdi et al. [112]	Tow testbed	LEI kite (6 m ²)	IMU, GNSS receiver, load cells and vehicle speed sensor	Suspended kite control unit	Data sets in different test conditions
2020	Schmidt et al. [209]	Fixed testbed	LEI and ram-air kites (3-12 m ²)	IMU, GNSS receiver, line-angle sensors, load cells and wind station; extended Kalman filter	Three-line ground control unit (linear actuators)	In-flight aerodynamic estimation
2021	Borobia-Moreno et al. [57]	Fixed testbed	LEI (10 m ²) and hybrid (1.9 m ²) kites	IMU, GNSS receiver, multi-hole pitot tube, load cells and wind station; extended Kalman filter	Manual steering	Identification of kite's aerodynamics
2022	Castelino et al. [197]	Fixed testbed	LEI kite (12 m ²)	IMU, GNSS receiver, load cells and wind sensor	Manual control bar	Tether force estimation
2023	Castro-Fernández et al. [58]	Fixed testbed	Hybrid kite (1.9 m ²)	IMU, GNSS receivers, load cells, actuator encoders, wind station and visual motion tracking system (3 cameras)	Three-line ground control system (linear actuator and winch)	Testbed for aerodynamic, dynamic and control characterization
2024	Elfert et al. [213]	Tow testbed	LEI kite (10 m ²)	IMU, GNSS receiver, multi-hole pitot tube, line-angle sensors and load cells	Three-line ground control unit (drums)	Turning behavior of tethered membrane wings

Data availability

No data was used for the research described in the article.

References

- [1] M. Blanch, A. Makris, B. Valpy, Getting airborne—the need to realise the benefits of airborne wind energy for net zero, 2022, pp. 1–44, White Paper for Airborne Wind Europe. URL: <https://airbornewindeurope.org/wp-content/uploads/2023/03/BVGA-Getting-Airborne-White-Paper-220929.pdf>.
- [2] K. Van Hussen, E. Dietrich, J. Smeltink, K. Berentsen, M. van der Sleen, R. Haffner, L. Fagiano, Study on challenges in the commercialisation of airborne wind energy systems, 2018, European Commission. URL: <https://op.europa.eu/en/publication-detail/-/publication/a874f843-c137-11e8-9893-01aa75ed71a1/language-en>.
- [3] U.S. Department of Energy, Report to congress: Challenges and opportunities for airborne wind energy in the United States, 2021, URL: <https://www.energy.gov/sites/default/files/2021-12/report-to-congress-challenges-opportunities-airborne-wind-energy-united-states.pdf>.
- [4] C.L. Archer, K. Caldeira, Global assessment of high-altitude wind power, 2, (2) 2009, pp. 307–319, <http://dx.doi.org/10.3390/en20200307>,
- [5] C.L. Archer, An introduction to meteorology for airborne wind energy, Springer, 2013, pp. 81–94.
- [6] P. Bechtle, M. Schelbergen, R. Schmehl, U. Zillmann, S. Watson, Airborne wind energy resource analysis, Renew. Energy 141 (2019) 1103–1116, <http://dx.doi.org/10.1016/j.renene.2019.03.118>.
- [7] M.S. Manalis, Airborne windmills and communication aerostats, J. Aircr. 13 (7) (1976) 543–544, <http://dx.doi.org/10.2514/3.58686>.
- [8] C.A.J. Fletcher, B.W. Roberts, Electricity generation from jet-stream winds, J. Energy 3 (4) (1979) 241–249, <http://dx.doi.org/10.2514/3.48003>.
- [9] M.L. Loyd, Crosswind kite power, J. Energy (1980) URL: <https://arc.aiaa.org/doi/abs/10.2514/3.48021?journalCode=je>.
- [10] B.W. Roberts, D.H. Shepard, K. Caldeira, M.E. Cannon, D.G. Eccles, A.J. Grenier, J.F. Freidin, Harnessing high-altitude wind power, IEEE Trans. Energy Convers. 22 (2007) 136–144, <http://dx.doi.org/10.1109/TEC.2006.889603>.
- [11] S. Rimkus, T. Das, An application of the autogyro theory to airborne wind energy extraction, 2013, <http://dx.doi.org/10.1115/DSCC2013-3840>, ASME 2013 Dynamic Systems and Control Conference.
- [12] R. Read, Kite networks for harvesting wind energy, in: Airborne Wind Energy: Advances in Technology Development and Research, Springer, 2018, pp. 515–537, URL: <https://link.springer.com/book/10.1007/978-981-10-1947-0>.
- [13] SkySails Power, SkySails power webpage, 2024, URL: <https://skysails-power.com/>.
- [14] M. Erhard, H. Strauch, Control of towing kites for seagoing vessels, in: IEEE Transactions on Control Systems Technology, vol. 21, 2013, pp. 1629–1640, <http://dx.doi.org/10.1109/TCST.2012.2221093>.
- [15] M. Erhard, H. Strauch, Flight control of tethered kites in autonomous pumping cycles for airborne wind energy, Control Eng. Pract. 40 (2015) 13–26, <http://dx.doi.org/10.1016/j.conengprac.2015.03.001>.
- [16] J.-c. Kim, C. Park, Wind power generation by pulling a ship with a parafoil, in: Airborne Wind Energy Conference 2010, Stanford, CA, 2010, pp. 1–12.
- [17] Oceanergy, Oceanergy webpage, 2025, URL: <https://www.oceanergy.com/>.
- [18] S. González, H. Moreno, Gone with the wind: Providing forecasts to the polar windsled expeditions, Helmholtz Blogs (2019) URL: <https://blogs.helmholtz.de/polarpredictionmatters/2019/12/gone-with-the-wind-providing-forecasts-to-the-polar-windsled-expeditions/>.
- [19] Airborne Wind Europe, Airborne wind europe webpage, 2024, URL: <https://airbornewindeurope.org/>.

- [20] A. Cherubini, A. Papini, R. Verthey, M. Fontana, Airborne wind energy systems: A review of the technologies, *Renew. Sustain. Energy Rev.* 51 (2015) 1461–1476, <http://dx.doi.org/10.1016/j.rser.2015.07.053>.
- [21] A.F. Pereira, J.M. Sousa, A review on crosswind airborne wind energy systems: Key factors for a design choice, *Energies* 16 (2023) 351, <http://dx.doi.org/10.3390/en16010351>.
- [22] Y. Khurshid, P. Paul, M. Elhesasy, B. Ali, M.M. Kamra, M. Okasha, T.N. Dief, From inception to commercialization : A systematic review of airborne wind energy systems, *Sustain. Energy Technol. Assess.* 83 (September) (2025) 104623, <http://dx.doi.org/10.1016/j.seta.2025.104623>.
- [23] L. Fagiano, M. Milanese, Airborne wind energy: An overview, *Proc. Am. Control. Conf.* (2012) 3132–3143, <http://dx.doi.org/10.1109/acc.2012.6314801>.
- [24] C. Vermillion, M. Cobb, L. Fagiano, R. Leuthold, M. Diehl, R.S. Smith, T.A. Wood, S. Rapp, R. Schmehl, D. Olinger, M. Demetriou, Electricity in the air: Insights from two decades of advanced control research and experimental flight testing of airborne wind energy systems, *Annu. Rev. Control.* 52 (2021) 330–357, <http://dx.doi.org/10.1016/j.arcontrol.2021.03.002>.
- [25] L. Fagiano, M. Quack, F. Bauer, L. Carnel, E. Oland, Autonomous airborne wind energy systems: Accomplishments and challenges, *Annu. Rev. Control. Robot. Auton. Syst.* 5 (2022) 603–631, <http://dx.doi.org/10.1146/annurev-control-042820-124658>.
- [26] Airborne Wind Europe, Glossary—Definitions of AWE-specific terms, 2024, URL: <https://airbornewindeurope.org/glossary-2/>.
- [27] P. Echeverri, T. Fricke, G. Homsy, N. Tucker, The energy kite: Selected results from the design, development and testing of makani's airborne wind turbines. Part I, 2020, Makani Technologies LLC, URL: <https://archive.org/details/theenergykite>.
- [28] P. Echeverri, T. Fricke, G. Homsy, N. Tucker, The energy kite selected results from the design, development and testing of makani's airborne wind turbines Part II, 2020, Makani Technologies LLC, URL: <https://archive.org/details/theenergykite>.
- [29] P. Echeverri, T. Fricke, G. Homsy, N. Tucker, The energy kite selected results from the design, development and testing of makani's airborne wind turbines. Part III, 2020, Makani Technologies LLC, URL: <https://archive.org/details/theenergykite>.
- [30] Makani, The makani collection. Shared resources from the energy kite project, 2020, URL: <https://x.company/collection/makani/>.
- [31] Windlift, Windlift webpage, 2024, URL: <https://windlift.com/>.
- [32] A.P. Ko, S. Smidt, R. Schmehl, M. Mandru, Optimization of a multi-element airfoil for a fixed-wing airborne wind energy system, *Energies* 16 (2023) 3521, <http://dx.doi.org/10.22214/ijraset.2020.4084>.
- [33] Mozaero, Mozaero webpage, 2025, URL: <https://www.mozaero.com/>.
- [34] TwingTec, TwingTec webpage, 2025, URL: <https://twingtec.ch/>.
- [35] G. Licitra, P. Williams, J. Gillis, S. Ghandchi, S. Sieberling, R. Ruiterkamp, M. Diehl, Aerodynamic parameter identification for an airborne wind energy pumping system, *IFAC-PapersOnLine* 50 (2017) 11951–11958, <http://dx.doi.org/10.1016/j.ifacol.2017.08.1038>.
- [36] G. Licitra, A. Bürger, P. Williams, R. Ruiterkamp, M. Diehl, Aerodynamic model identification of an autonomous aircraft for airborne wind energy, *Optim. Control. Appl. Methods* 40 (2019) 422–447, <http://dx.doi.org/10.1002/oca.2485>.
- [37] J. Wijnja, R. Schmehl, R.D. Breuker, K. Jensen, D.V. Lind, Aeroelastic analysis of a large airborne wind turbine, *J. Guid. Control Dyn.* 41 (2018) 1–12, <http://dx.doi.org/10.2514/1.G001663>.
- [38] F. Bauer, R.M. Kennel, C.M. Hackl, F. Campagnolo, M. Patt, R. Schmehl, Drag power kite with very high lift coefficient, *Renew. Energy* 118 (2018) 290–305, <http://dx.doi.org/10.1016/j.renene.2017.10.073>.
- [39] D. Todeschini, L. Fagiano, C. Micheli, A. Cattano, Control of a rigid wing pumping airborne wind energy system in all operational phases, *Control Eng. Pract.* 111 (2021) <http://dx.doi.org/10.1016/j.conengprac.2021.104794>.
- [40] D. Eijkelhof, G. Buendía, R. Schmehl, Low- and high-fidelity aerodynamic simulations of box wing kites for airborne wind energy applications, *Energies* 16 (2023) 3008, <http://dx.doi.org/10.3390/en16073008>.
- [41] KiteKraft, KiteKraft webpage, 2024, URL: <https://www.kitekraft.de/>.
- [42] Kitemill, Kitemill webpage, 2024, URL: <https://www.kitemill.com/>.
- [43] Kitepower, Webpage of kitepower, 2024, URL: <https://thekitepower.com/>.
- [44] EnerKite, Enerkite webpage, 2024, URL: <https://enerkite.de/en/>.
- [45] Wind Fisher, Wind Fisher webpage, 2024, URL: <https://wind-fisher.com/>.
- [46] Altaeros, Altaeros webpage, 2024, 2024, URL: <https://www.altaios.com/>.
- [47] R. van der Vlugt, J. Peschel, R. Schmehl, Design and experimental characterization of a pumping kite power system, in: U. Ahrens, M. Diehl, R. Schmehl (Eds.), *Airborne Wind Energy. Series: Green Energy and Technology*, 2013, pp. 403–425, http://dx.doi.org/10.1007/978-3-642-39965-7_23.
- [48] M. Milanese, F. Taddei, S. Milanese, Design and testing of a 60 kw yo-yo airborne wind energy generator, in: U. Ahrens, M. Diehl, R. Schmehl (Eds.), *Airborne Wind Energy. Series: Green Energy and Technology*, 2013, pp. 373–386, http://dx.doi.org/10.1007/978-3-642-39965-7_21.
- [49] M. Milanese, Kiteenergy project: Renewable energy cheaper than oil, in: *High Altitude Wind Power (HAWP) Conference 2009*, Chico, CA, 2009.
- [50] O. Cayon, M. Gaunaa, R. Schmehl, Fast aero-structural model of a leading-edge inflatable kite, *Energies* 16 (2023) 3061, <http://dx.doi.org/10.3390/en16073061>.
- [51] J.A.W. Poland, R. Schmehl, Modelling aero-structural deformation of flexible membrane kites, *Energies* 16 (2023) 5264, <http://dx.doi.org/10.3390/en16145264>.
- [52] A. de Wachter, Deformation and Aerodynamic Performance of a Ram-Air Wing (Master's thesis), Delft Univ. Tech., 2008, URL: <http://resolver.tudelft.nl/uuid:786e3395-4590-4755-829f-51283a8df3d2>.
- [53] M. Folkersma, R. Schmehl, A. Vire, Steady-state aeroelasticity of a ram-air wing for airborne wind energy applications, *J. Phys.: Conf. Ser.* (2020) 1–13, <http://dx.doi.org/10.1088/1742-6596/1618/3/032018>.
- [54] P. Thedens, R. Schmehl, An aero-structural model for ram-air kite simulations, *Energies* 16 (2023) 2603, <http://dx.doi.org/10.3390/en16062603>.
- [55] A.A. Candade, M. Ranneberg, R. Schmehl, Structural analysis and optimization of a tethered swept wing for airborne wind energy generation, *Wind. Energy* 23 (2020) 1006–1025, <http://dx.doi.org/10.1002/we.2469>.
- [56] T. Nam, E. Itakura, T. Tsukada, High altitude aerial platform “mothership” project vision and progress, in: *AIAA SCITECH 2024 Forum*, Orlando, FL, 2024, <http://dx.doi.org/10.2514/6.2024-2094>.
- [57] R. Borobia-Moreno, D. Ramiro-Rebollo, R. Schmehl, G. Sánchez-Arriaga, Identification of kite aerodynamic characteristics using the estimation before modeling technique, *Wind. Energy* 24 (2021) 596–608, <http://dx.doi.org/10.1002/we.2591>.
- [58] I. Castro-Fernández, F. DeLosRíos-Navarrete, R. Borobia-Moreno, M. Fernández-Jiménez, H. García-Cousillas, M. Zas-Bustingorri, Á.T. Ghoibassi, F. López-Vega, K. Best, R. Cavallaro, G. Sánchez-Arriaga, Automatic testbed with a visual motion tracking system for airborne wind energy applications, *Wind. Energy* 26 (2023) 388–401, <http://dx.doi.org/10.1002/we.2805>.
- [59] A.A. Candade, M. Ranneberg, R. Schmehl, Aero-structural design of composite wings for airborne wind energy applications, *J. Phys.: Conf. Ser.* 1618 (2020) <http://dx.doi.org/10.1088/1742-6596/1618/3/032016>.
- [60] T. Nam, Y. Zhu, X. Deng, C. Zhao, E. Itakura, T. Tsukada, Development and testing of an airborne wind energy system, in: *Airborne Wind Energy Conference 2024*, Madrid, 2024, <http://dx.doi.org/10.4233/uuid:85fd0eb1-83ec-4e34-9ac8-be6b32082a52>.
- [61] I. Castro-Fernández, R. Cavallaro, R. Schmehl, G. Sánchez-Arriaga, Unsteady aerodynamics of delta kites for airborne wind energy under dynamic stall conditions, *Wind. Energy* 27 (9) (2024) 936–952, <http://dx.doi.org/10.1002/we.2932>.
- [62] I. Castro-Fernández, A. Cini, R. Cavallaro, A. Iboleón-Azcona, M. Gisbert-Calvo, G. Sánchez-Arriaga, Fluid-structure interaction analysis of a rigid-Framed Delta kite for airborne wind energy, 2024, <http://dx.doi.org/10.13140/RG.2.2.17699.26402>, *Airborne Wind Energy Conference 2024*.
- [63] Y. Boucheriguene, G. Smith, A. Tardella, E. Carvalho, A. Nègre, N. Meslem, J. Dumon, Dual-cylinder magnus effect kite: Fixed-distance flight tests at wind Fisher, 2024, <http://dx.doi.org/10.4233/uuid:85fd0eb1-83ec-4e34-9ac8-be6b32082a52>, *Airborne Wind Energy Conference 2024*.
- [64] Y. Boucheriguene, E. Carvalho, G. Smith, A. Tardella, Modeling and control of a magnus effect kite: Pumping cycle with reversing rotation, 2024, <http://dx.doi.org/10.4233/uuid:85fd0eb1-83ec-4e34-9ac8-be6b32082a52>, *Airborne Wind Energy Conference 2024*.
- [65] E. Schmidt, Y. Gupta, J. Dumon, A. Hably, In-flight estimation of the aerodynamic characteristics of a magnus effect-based airborne wind energy system, in: *4th Int. Conf. Renewable Energies for Developing Countries, REDEC, IEEE, 2018*, pp. 1–7, URL: <https://hal.science/hal-01895342v1/file/redecsmall.pdf>.
- [66] C. Beaupoil, Practical experiences with a torsion based rigid blade rotary airborne wind energy system with ground based power generation, in: *Airborne Wind Energy Conference 2019*, Glasgow (UK), 2019, pp. 146–147, <http://dx.doi.org/10.4233/uuid:57fd203c-e069-11e9-9fcb-441ea15f7c9c>.
- [67] D. Unterweger, Cyclic pitch control of a rotary kite, 2022, IMTEK, Faculty of Engineering, University of Freiburg. URL: <https://www.syscop.de/files/2021/ws/msi/Cyclic%20Pitch%20Control.pdf>.
- [68] P. Rivard, MAGENN power, inc. Wind power anywhere, 2010, *Airborne Wind Energy Conference 2010*.
- [69] C. Vermillion, T. Grunnagle, I. Kolmanovsky, Modeling and control design for a prototype lighter-than-air wind energy system, in: *American Control Conference, 2012*, pp. 5813–5818, URL: <https://ieeexplore.ieee.org/document/6315434>.
- [70] C. Vermillion, B. Glass, A. Rein, Lighter-than-air wind energy systems, in: U. Ahrens, M. Diehl, R. Schmehl (Eds.), *Airborne Wind Energy. Series: Green Energy and Technology*, Springer, 2013, pp. 501–514, http://dx.doi.org/10.1007/978-3-642-39965-7_30.
- [71] G.D.D. Fezza, S. Barber, Parameter analysis of a multi-element airfoil for application to airborne wind energy, *Wind. Energy Sci.* 7 (2022) 1627–1640, <http://dx.doi.org/10.5194/wes-7-1627-2022>.
- [72] K. Vimalakanthan, M. Caboni, J. Schepers, E. Pechenik, P. Williams, Aerodynamic analysis of Ampyx's airborne wind energy system, *J. Phys.: Conf. Ser.* 1037 (2018) 1–10, <http://dx.doi.org/10.1088/1742-6596/1037/6/062008>.

- [73] D. Fischer, B. Church, C.N. Nayeri, C.O. Paschereit, Investigation and optimisation of high-lift airfoils for airborne wind energy systems at high Reynolds numbers, *Wind* 3 (2) (2023) 273–290, <http://dx.doi.org/10.3390/wind3020016>.
- [74] J. Breukels, An Engineering Methodology for Kite Design (Ph.D. thesis), Delft Univ. Techn., 2010, URL: <http://resolver.tudelft.nl/uuid:cdece38a-1f13-47cc-b277-ed64fd4da7cdf>.
- [75] J. Breukels, R. Schmehl, W. Ockels, Aeroelastic simulation of flexible membrane wings based on multibody system dynamics, in: U. Ahrens, M. Diehl, R. Schmehl (Eds.), *Airborne Wind Energy. Series: Green Energy and Technology*, 2013, pp. 287–305, http://dx.doi.org/10.1007/978-3-642-39965-7_16.
- [76] M. Folkersma, R. Schmehl, A. Viré, Boundary layer transition modeling on leading edge inflatable kite airfoils, *Wind. Energy* 22 (2019) 908–921, <http://dx.doi.org/10.1002/we.2329>.
- [77] A. Viré, P. Demkowicz, M. Folkersma, A. Roullier, R. Schmehl, Reynolds-averaged Navier-Stokes simulations of the flow past a leading edge inflatable wing for airborne wind energy applications, *J. Phys.: Conf. Ser.* 1618 (2020) <http://dx.doi.org/10.1088/1742-6596/1618/3/032007>.
- [78] A. Viré, G. Lebesque, M. Folkersma, R. Schmehl, Effect of chordwise struts and misaligned flow on the aerodynamic performance of a leading-edge inflatable wing, *Energies* 15 (2022) 1450, <http://dx.doi.org/10.3390/en15041450>.
- [79] P. Thedens, G. de Oliveira, R. Schmehl, Ram-air kite airfoil and reinforcements optimization for airborne wind energy applications, *Wind. Energy* 22 (2019) 653–665, <http://dx.doi.org/10.1002/we.2313>.
- [80] M. Milutinović, M. Corić, J. Deur, Operating cycle optimization for a magnus effect-based airborne wind energy system, *Energy Convers. Manage.* 90 (2015) 154–165, <http://dx.doi.org/10.1016/j.enconman.2014.10.066>.
- [81] Q.S. Ali, M.H. Kim, Design and performance analysis of an airborne wind turbine for high-altitude energy harvesting, *Energy* 230 (2021) 1–16, <http://dx.doi.org/10.1016/j.energy.2021.120829>.
- [82] Q.S. Ali, M.-H. Kim, Power conversion performance of airborne wind turbine under unsteady loads, *Renew. Sustain. Energy Rev.* 153 (2022) 1–17, <http://dx.doi.org/10.1016/j.rser.2021.111798>.
- [83] Q.S. Ali, M.H. Kim, Quantifying impacts of shell augmentation on power output of airborne wind energy system at elevated heights, *Energy* 239 (2022) <http://dx.doi.org/10.1016/j.energy.2021.121839>.
- [84] S.M. Salih, M.Q. Taha, M.K. Alawsaj, Performance analysis of wind turbine systems under different parameters effect, *Int. J. Energy Environ.* 3 (2012) 895–904, URL: <https://www.researchgate.net/publication/268485737>.
- [85] S. Rapp, R. Schmehl, E. Oland, T. Haas, Cascaded pumping cycle control for rigid wing airborne wind energy systems, *J. Guid. Control Dyn.* 42 (2019) 2456–2473, <http://dx.doi.org/10.2514/1.G004246>.
- [86] M. Schelbergen, R. Schmehl, Swinging motion of a kite with suspended control unit flying turning manoeuvres, *Wind. Energy Sci.* 9 (2024) 1323–1344, <http://dx.doi.org/10.5194/wes-9-1323-2024>.
- [87] A. Bormann, M. Ranneberg, P. Kövesdi, C. Gebhardt, S. Skutnik, Development of a three-line ground-actuated airborne wind energy converter, in: U. Ahrens, M. Diehl, R. Schmehl (Eds.), *Airborne Wind Energy*, Springer, 2013, pp. 427–436, http://dx.doi.org/10.1007/978-3-642-39965-7_24.
- [88] someAWE, someAWE webpage, 2024, URL: <https://someawe.org/>.
- [89] A. Frirdich, Kitekraft completes wind tunnel test campaign, 2023, <https://www.kitekraft.de/blog/kitekraft-completes-wind-tunnel-test-campaign>. (Accessed 5 August 2024).
- [90] K.W. McAlister, S.L. Pucci, W.J. McCroskey, L.W. Carr, An experimental study of dynamic stall on advanced airfoil sections. Volume 2. Pressure and force data, 1982, NASA Technical Memorandum 84245. URL: <https://ntrs.nasa.gov/citations/19820024438>.
- [91] M. Platzer, N. Sarigul-Klijn, A novel system for high altitude wind power extraction (iPG), in: *Airborne Wind Energy Conference 2010*, Stanford, CA, 2010, pp. 1–32.
- [92] G. Bangga, T. Lutz, M. Arnold, An improved second-order dynamic stall model for wind turbine airfoils, *Wind. Energy Sci.* 5 (2020) 1037–1058, <http://dx.doi.org/10.5194/wes-5-1037-2020>.
- [93] F. Trevisi, Conceptual Design of Windplanes (Ph.D. thesis), Politecnico di Milano, 2024, URL: https://www.researchgate.net/publication/378402043_Conceptual_design_of_windplanes.
- [94] F. Trevisi, A. Croce, Given a wingspan, which windplane design maximizes power? *J. Phys.: Conf. Series* 2767 (2024) <http://dx.doi.org/10.1088/1742-6596/2767/7/072014>.
- [95] I. Argatov, P. Rautakorpi, R. Silvennoinen, Estimation of the mechanical energy output of the kite wind generator, *Renew. Energy* 34 (2009) 1525–1532, <http://dx.doi.org/10.1016/j.renene.2008.11.001>.
- [96] I. Argatov, P. Rautakorpi, R. Silvennoinen, Apparent wind load effects on the tether of a kite power generator, *J. Wind Eng. Ind. Aerodyn.* 99 (2011) 1079–1088, <http://dx.doi.org/10.1016/j.jweia.2011.07.010>.
- [97] R. van der Vlugt, A. Bley, M. Noom, R. Schmehl, Quasi-steady model of a pumping kite power system, *Renew. Energy* 131 (2019) 83–99, <http://dx.doi.org/10.1016/j.renene.2018.07.023>.
- [98] F. Trevisi, M. Gaunaa, M. McWilliam, The influence of tether sag on airborne wind energy generation, *J. Phys.: Conf. Ser.* 1618 (2020) <http://dx.doi.org/10.1088/1742-6596/1618/3/032006>.
- [99] R. Schmehl, M. Noom, R.V. der Vlugt, Traction power generation with tethered wings, in: U. Ahrens, M. Diehl, R. Schmehl (Eds.), *Airborne Wind Energy. Series: Green Energy and Technology*, Springer, 2013, pp. 23–45, http://dx.doi.org/10.1007/978-3-642-39965-7_2.
- [100] S. Costello, C. Costello, G. François, D. Bonvin, Analysis of the maximum efficiency of kite-power systems, *J. Renew. Sustain. Energy* 7 (2015) <http://dx.doi.org/10.1063/1.4931111>.
- [101] M. Zanon, S. Gros, J. Meyers, M. Diehl, Airborne wind energy: Airfoil-airmass interaction, *IFAC Proc. Vol. (IFAC-PapersOnline)* 19 (2014) 5814–5819, <http://dx.doi.org/10.3182/20140824-6-za-1003.00258>.
- [102] R. Leuthold, S. Gros, M. Diehl, Induction in optimal control of multiple-kite airborne wind energy systems, *IFAC-PapersOnline* 50 (2017) 153–158, <http://dx.doi.org/10.1016/j.ifacol.2017.08.026>.
- [103] F. Bauer, D. Petzold, R.M. Kennel, F. Campagnolo, R. Schmehl, Control of a drag power kite over the entire wind speed range, *J. Guid. Control Dyn.* 42 (2019) 2167–2182, <http://dx.doi.org/10.2514/1.G004207>.
- [104] F. Trevisi, I. Castro-Fernández, G. Pasquinelli, C.E.D. Riboldi, A. Croce, Flight trajectory optimization of fly-gen airborne wind energy systems through a harmonic balance method, *Wind. Energy Sci.* 7 (2022) 2039–2058, <http://dx.doi.org/10.5194/wes-7-2039-2022>.
- [105] L. Shepard, Flying electric generators, in: *High Altitude Wind Power (HAWP) Conference 2009*, Chico, CA, 2009.
- [106] L. Shepard, B. Weddendorf, Sky WindPower. a generation above, in: *Airborne Wind Energy Conference 2010*, Stanford, CA, 2010, pp. 1–12.
- [107] S. Webster, Introduction of sky mill's HAWP system, in: *High Altitude Wind Power (HAWP) Conference 2009*, Chico, CA, 2009.
- [108] S. Webster, SkyMill energy, inc. a practical approach to tap the power of high-altitude wind, in: *Airborne Wind Energy Conference 2010*, vol. 360, Stanford, CA, 2010.
- [109] J. Bevirt, Joby energy high altitude wind energy and joby technology, in: *High Altitude Wind Power (HAWP) Conference 2009*, Chico, CA, 2009.
- [110] L. Fagiano, T. Marks, Design of a small-scale prototype for research in airborne wind energy, *IEEE/ASME Trans. Mechatronics* 20 (2015) 166–177, <http://dx.doi.org/10.1109/TMECH.2014.2322761>.
- [111] J. Hummel, D. Göhlich, R. Schmehl, Automatic measurement and characterization of the dynamic properties of tethered membrane wings, *Wind. Energy Sci.* 4 (2019) 41–55, <http://dx.doi.org/10.5194/wes-4-41-2019>.
- [112] M.A. Rushdi, T.N. Dief, S. Yoshida, R. Schmehl, Towing test data set of the Kyushu University kite system, *Data* 5 (2020) 1–18, <http://dx.doi.org/10.3390/data5030069>.
- [113] C. Jehle, R. Schmehl, Applied tracking control for kite power systems, *J. Guid. Control Dyn.* 37 (2014) 1211–1222, <http://dx.doi.org/10.2514/1.62380>.
- [114] L. Fagiano, A.U. Zraggen, M. Morari, M. Khammash, Automatic crosswind flight of tethered wings for airborne wind energy: Modeling, control design, and experimental results, *IEEE Trans. Control Syst. Technol.* 22 (2014) 1433–1447, <http://dx.doi.org/10.1109/TCST.2013.2279592>.
- [115] T.A. Wood, H. Hesse, A.U. Zraggen, R.S. Smith, Model-based identification and control of the velocity vector orientation for autonomous kites, *Proc. Am. Control. Conf.* 2015-July (2015) 2377–2382, <http://dx.doi.org/10.1109/ACC.2015.7171088>.
- [116] A. Bosch, R. Schmehl, P. Tiso, D. Rixen, Dynamic nonlinear aeroelastic model of a kite for power generation, *J. Guid. Control Dyn.* 37 (2014) 1426–1436, <http://dx.doi.org/10.2514/1.G000545>.
- [117] J. Oehler, R. Schmehl, Aerodynamic characterization of a soft kite by in situ flow measurement, *Wind. Energy Sci.* 4 (2019) 1–21, <http://dx.doi.org/10.5194/wes-4-1-2019>.
- [118] M. Gaster, The structure and behaviour of laminar separation bubbles, 1967, Report No. 3595, Aerodynamics Division, NPL. URL: <https://naca.central.cranfield.ac.uk/bitstream/handle/1826.2/2862/arc-rm-3595.pdf?sequence=1&isAllowed=y>.
- [119] L.W. Carr, Progress in analysis and prediction of dynamic stall, *J. Aircr.* 25 (1988) 6–17, <http://dx.doi.org/10.2514/3.45534>.
- [120] S.B. Pope, *Turbulent Flows*, Cambridge University Press, 2000, <http://dx.doi.org/10.1017/CBO9780511840531>.
- [121] P.S. Jackson, Optimal loading of a tension kite, *AIAA J.* 43 (11) (2005) 2273–2278, <http://dx.doi.org/10.2514/1.3543>.
- [122] A. de Solminihac, A. Nême, C. Duport, J.-B.L.K. Roncin, C. Jochum, Y. Parlier, Kite as a beam: A fast method to get the flying shape, in: R. Schmehl (Ed.), *Airborne Wind Energy: Advances in Technology Development and Research. Series: Green Energy and Technology*, Springer, 2018, pp. 79–97, http://dx.doi.org/10.1007/978-981-10-1947-0_4, URL: <https://link.springer.com/book/10.1007/978-981-10-1947-0>.
- [123] R. Leloup, K. Roncin, G. Bles, J.-B. Leroux, Estimation of the lift-to-drag ratio using the lifting line method: Application to a leading edge inflatable kite, in: U. Ahrens, M. Diehl, R. Schmehl (Eds.), *Airborne Wind Energy. Series: Green Energy and Technology*, 2013, pp. 339–355, http://dx.doi.org/10.1007/978-3-642-39965-7_19.
- [124] M. Gaunaa, Influence of implementation details in the accuracy of lifting line models for airborne wind energy applications, 2023, *Wind Energy Science Conference 2023*. URL: <https://www.northwindresearch.no/event/wind-energy-science-conference-2023/>.

- [125] T. Haas, J.D. Schutter, M. Diehl, J. Meyers, Large-eddy simulation of airborne wind energy farms, *Wind. Energy Sci.* 7 (2022) 1093–1135, <http://dx.doi.org/10.5194/wes-7-1093-2022>.
- [126] C. Dupont, Modeling with Consideration of the Fluid-Structure Interaction of the Behavior Under Load of a Kite for Auxiliary Traction of Ships (Ph.D. thesis), Université Bretagne Loire, 2018, URL: <https://theses.hal.science/tel-02383312v1>.
- [127] M. Ranneberg, Direct wing design and inverse airfoil identification with the nonlinear weissinger method, 2015, pp. 1–13, URL: <https://arxiv.org/abs/1501.04983>.
- [128] R. Damiani, F. Wendt, J. Jonkman, J. Sicard, A vortex step method for nonlinear airfoil polar data as implemented in KiteAeroDyn, 2019, <http://dx.doi.org/10.2514/6.2019-0804>, AIAA 2019-0804.
- [129] F. Gohl, R.H. Luchsinger, Simulation based wing design for kite power, in: U. Ahrens, M. Diehl, R. Schmehl (Eds.), *Airborne Wind Energy Series: Green Energy and Technology*, 2013, pp. 325–338, http://dx.doi.org/10.1007/978-3-642-39965-7_18.
- [130] R. Leuthold, Multiple-Wake Vortex Lattice Method for Membrane-Wing Kites (Ph.D. thesis), Delft Univ. Tech., 2015, <http://dx.doi.org/10.13140/RG.2.2.30811.41765>.
- [131] M. Gaunaa, F.P.P. Carqueija, P.-E. Réthoré, N.N. Sørensen, A computationally efficient method for determining the aerodynamic performance of kites for energy applications, in: EWEA 2011, 2011, pp. 1–11, URL: <http://orbit.dtu.dk/getResource?recordId=276109&objectId=1&versionId=4>.
- [132] U. Fasel, D. Keidel, G. Molinari, P. Ermanni, Aerostructural optimization of a morphing wing for airborne wind energy applications, *Smart Mater. Struct.* 26 (2017) 1–11, <http://dx.doi.org/10.1088/1361-665X/aa7c87>.
- [133] U. Fasel, P. Tiso, D. Keidel, G. Molinari, P. Ermanni, Reduced-order dynamic model of a morphing airborne wind energy aircraft, *AIAA J.* 57 (2019) 3586–3598, <http://dx.doi.org/10.2514/1.J058019>.
- [134] F. Trevisi, C.E.D. Riboldi, A. Croce, Vortex model of the aerodynamic wake of airborne wind energy systems, *Wind. Energy Sci.* 8 (2023) 999–1016, <http://dx.doi.org/10.5194/wes-8-999-2023>.
- [135] M. Gaunaa, A. Li, M. McWilliam, M. Kelly, Lifting-line aerodynamics for airborne wind energy on a prescribed path, in: *Airborne Wind Energy Conference, AWEC 2024*, Madrid, 2024, pp. 120–120, <http://dx.doi.org/10.4233/uuid:85fd0eb1-83ec-4e34-9ac8-be6b32082a52>.
- [136] I. Castro-Fernández, R. Borobia-Moreno, R. Cavallaro, G. Sánchez-Arriaga, Three-dimensional unsteady aerodynamic analysis of a rigid-Framed Delta kite applied to airborne wind energy, *Energies* 14 (2021) 8080, <http://dx.doi.org/10.3390/en14238080>.
- [137] N. Fonzi, S.L. Brunton, U. Fasel, Data-driven nonlinear aeroelastic models of morphing wings for control, *Proc. R. Soc. A* 476 (2239) (2020) 20200079, <http://dx.doi.org/10.1098/rspa.2020.0079>.
- [138] M. Buffoni, B. Galletti, J. Ferreau, L. Fagiano, M. Mercangoez, Active pitch control of tethered wings for airborne wind energy, in: *53rd IEEE Conference on Decision and Control, IEEECDC, 2014*, 2014, pp. 4893–4898, <http://dx.doi.org/10.1109/CDC.2014.7040153>.
- [139] A. Saleem, M.H. Kim, Effect of rotor axial position on the aerodynamic performance of an airborne wind turbine system in shell configuration, *Energy Convers. Manage.* 151 (2017) 587–600, <http://dx.doi.org/10.1016/j.enconman.2017.09.026>.
- [140] A. Saleem, M.H. Kim, Aerodynamic analysis of an airborne wind turbine with three different airfoil-based buoyant shells using steady RANS simulations, *Energy Convers. Manage.* 177 (2018) 233–248, <http://dx.doi.org/10.1016/j.enconman.2018.09.067>.
- [141] A. Saleem, M.H. Kim, Aerodynamic performance optimization of an airfoil-based airborne wind turbine using genetic algorithm, *Energy* 203 (2020) 117841, <http://dx.doi.org/10.1016/j.energy.2020.117841>.
- [142] M. Kheiri, F. Bourgault, V.S. Nasrabad, S. Victor, On the aerodynamic performance of crosswind kite power systems, *J. Wind Eng. Ind. Aerodyn.* 181 (2018) 1–13, <http://dx.doi.org/10.1016/j.jweia.2018.08.006>, URL: <https://resolver.tudelft.nl/uuid:18ae2cc6-434e-49c8-9296-d3fa450850a5>.
- [143] M. Kheiri, S. Victor, S. Rangriz, M.M. Karakouzian, F. Bourgault, Aerodynamic performance and wake flow of crosswind kite power systems, *Energies* 15 (2022) 2449, <http://dx.doi.org/10.3390/en15072449>.
- [144] N. Pynaert, J. Wauters, G. Crevecoeur, J. Degroote, Unsteady aerodynamic simulations of a multi-megawatt airborne wind energy reference system using computational fluid dynamics, *J. Phys.: Conf. Ser.* (2022) 1–10, <http://dx.doi.org/10.1088/1742-6596/2265/4/042060>.
- [145] N. Pynaert, T. Haas, J. Wauters, G. Crevecoeur, J. Degroote, Wing deformation of an airborne wind energy system in crosswind flight using high-fidelity fluid – structure interaction, *Energies* 16 (2023) 602, <http://dx.doi.org/10.3390/en16020602>.
- [146] N. Pynaert, T. Haas, J. Wauters, Moving control surfaces in a geometry-resolved CFD model of an airborne wind energy system, *J. Phys.: Conf. Ser.* 2767 (2024) <http://dx.doi.org/10.1088/1742-6596/2767/2/022041>.
- [147] M. Saeed, M.H. Kim, Aerodynamic performance analysis of an airborne wind turbine system with NREL phase IV rotor, *Energy Convers. Manage.* 134 (2017) 278–289, <http://dx.doi.org/10.1016/j.enconman.2016.12.021>.
- [148] Q.S. Ali, M.H. Kim, Unsteady aerodynamic performance analysis of an airborne wind turbine under load varying conditions at high altitude, *Energy Convers. Manage.* 210 (2020) 1–18, <http://dx.doi.org/10.1016/j.enconman.2020.112696>.
- [149] A.M. Nejad, D.J. Olinger, G. Tryggvason, Numerical modeling of kites for power generation, in: *FEDSM2014-21168*, 2014, pp. 1–8, <http://dx.doi.org/10.1115/FEDSM2014-21168>.
- [150] A. Scupi, E. Avital, D. Dinu, J. Williams, A. Munjiza, Large eddy simulation of flows around a kite used as an auxiliary propulsion system, *J. Fluids Eng.* 137 (2015) <http://dx.doi.org/10.1115/1.4030482>.
- [151] T. Haas, N. Pynaert, J. Degroote, Aerodynamic analysis of an airborne wind energy system in turbulent wind conditions, in: *Airborne Wind Energy Conference, AWEC 2024*, Madrid, 2024, <http://dx.doi.org/10.4233/uuid:85fd0eb1-83ec-4e34-9ac8-be6b32082a52>, 72–72.
- [152] J.-B. Crismer, T. Haas, M. Duponcheel, G. Winckelmans, Airborne wind energy systems flying optimal trajectories in turbulent wind using flight path tracking, *J. Phys.: Conf. Ser.* 2767 (2024) <http://dx.doi.org/10.1088/1742-6596/2767/7/072021>.
- [153] P. Moin, *Fundamentals of Engineering Numerical Analysis*, Cambridge Univ. Press, 2010, <http://dx.doi.org/10.1017/CBO9780511781438>.
- [154] J. Katz, A. Plotkin, *Low-Speed Aerodynamics*, second ed., San Diego, 2001, p. 629, <http://dx.doi.org/10.1017/CBO9780511810329>.
- [155] L. Prandtl, Theory of lifting surfaces, 1918, Technical Report National Advisory Committee for Aeronautics, Washington DC. URL: <https://ntrs.nasa.gov/api/citations/19930080806/downloads/19930080806.pdf>.
- [156] F. Bauer, Tech-deep-dive: How kitekraft solves aerodynamics, 2023, <https://www.kitekraft.de/blog/tech-deep-dive-how-kitekraft-solves-aerodynamics>. (Accessed 4 November 2024).
- [157] J. Moran, *An Introduction to Theoretical and Computational Aerodynamics*, John Wiley & Sons, 1984, <http://dx.doi.org/10.2514/3.48703>.
- [158] P. Thedens, M. Folkersma, R. Schmehl, Computational simulation of the aerodynamics of a ram-air kite for airborne wind energy applications, in: *Wind Energy Science Conference (WESC) 2021*, 2021, pp. 1–24, URL: <https://www.researchgate.net/publication/352372662>.
- [159] J.H. Ferziger, M. Perić, R.L. Street, *Computational Methods for Fluid Dynamics*, Springer International Publishing, Cham, 2020, <http://dx.doi.org/10.1007/978-3-319-99693-6>.
- [160] C. Hirsch, *Numerical Computation of Internal and External Flows*, Elsevier, 2007, <http://dx.doi.org/10.1016/B978-0-7506-6594-0.X5037-1>.
- [161] P. Sagaut, *Large Eddy Simulation for Incompressible Flows*, Springer-Verlag, Berlin/Heidelberg, 2006, <http://dx.doi.org/10.1007/b137536>.
- [162] R. Vinuesa, P. Negi, M. Atzori, A. Hanifi, D. Henningson, P. Schlatter, Turbulent boundary layers around wing sections up to $Re_c = 1,000,000$, *Int. J. Heat Fluid Flow* 72 (2018) 86–99, <http://dx.doi.org/10.1016/j.ijheatfluidflow.2018.04.017>.
- [163] M.R. Visbal, D.J. Garmann, Analysis of dynamic stall on a pitching airfoil using high-fidelity large-eddy simulations, *AIAA J.* 56 (2018) 46–63, <http://dx.doi.org/10.2514/1.J056108>.
- [164] P.A. Durbin, B.A.P. Reif, *Statistical Theory and Modeling for Turbulent Flows*, Wiley, 2010, <http://dx.doi.org/10.1002/9780470972076>.
- [165] T. Liu, S. Wang, H. Liu, G. He, Engineering perspective on bird flight: Scaling, geometry, kinematics and aerodynamics, *Prog. Aerosp. Sci.* (2023) 100933, <http://dx.doi.org/10.1016/j.paerosci.2023.100933>.
- [166] F.R. Menter, Zonal two equation kw turbulence models for aerodynamic flows, 1993, p. 2906, <http://dx.doi.org/10.2514/6.1993-2906>, 23rd Fluid dynamics, plasmadynamics, and lasers conference.
- [167] R.B. Langtry, F.R. Menter, Correlation-based transition modeling for unstructured parallelized computational fluid dynamics codes, *AIAA J.* 47 (12) (2009) 2894–2906, <http://dx.doi.org/10.2514/1.42362>.
- [168] J.C. Lin, Review of research on low-profile vortex generators to control boundary-layer separation, *Prog. Aerosp. Sci.* 38 (4–5) (2002) 389–420, [http://dx.doi.org/10.1016/S0376-0421\(02\)00010-6](http://dx.doi.org/10.1016/S0376-0421(02)00010-6).
- [169] R. Carpenter, Mesoscale modeling for airborne wind energy forecasting, in: *Airborne Wind Energy Conference 2010*, Stanford, CA, 2010.
- [170] W.C. Skamarock, J.B. Klemp, A time-split nonhydrostatic atmospheric model for weather research and forecasting applications, *J. Comput. Phys.* 227 (7) (2008) 3465–3485, <http://dx.doi.org/10.1016/j.jcp.2007.01.037>.
- [171] M. Sommerfeld, M. Dörenkämper, G. Steinfeld, C. Crawford, Improving mesoscale wind speed forecasts using lidar-based observation nudging for airborne wind energy systems, *Wind. Energy Sci.* 4 (4) (2019) 563–580, <http://dx.doi.org/10.5194/wes-4-563-2019>.
- [172] M. Sommerfeld, C. Crawford, A. Monahan, I. Bastigkeit, Lidar-based characterization of mid-altitude wind conditions for airborne wind energy systems, *Wind. Energy* 22 (2019) 1101–1120, <http://dx.doi.org/10.1002/we.2343>.
- [173] M. Sommerfeld, M. Dörenkämper, J.D. Schutter, C. Crawford, Impact of wind profiles on ground-generation airborne wind energy system performance, *Wind. Energy Sci.* 8 (2023) 1153–1178, <http://dx.doi.org/10.5194/wes-8-1153-2023>.
- [174] F.M. Rogallo, NASA research on flexible wings, 1967, L-5419, NASA Langley Research Center.

- [175] R.L. Naeseth, Low-speed wind-tunnel investigation of a series of twin-keel all-flexible parawings, 1970, D-5936, NASA Langley Research Center. URL: <https://ntrs.nasa.gov/api/citations/19710000578/downloads/19710000578.pdf>.
- [176] H. Babinsky, The aerodynamic performance of paragliders, *Aeronaut. J.* 103 (1027) (1999) 421–428, <http://dx.doi.org/10.1017/S0001924000027974>.
- [177] D.M. Benedetti, C.A.G. Veras, Wind-tunnel measurement of differential pressure on the surface of a dynamically inflatable wing cell, *Aerospace* 8 (2) (2021) <http://dx.doi.org/10.3390/aerospace8020034>.
- [178] S.B. Jackson, Free-flight tests on kites in the 24-ft wind tunnel, *Aeronaut. Res. Counc. Rep. Memo.* (1951) 1–90, URL: <https://reports.aerade.cranfield.ac.uk/handle/1826.2/3137>.
- [179] A.R. Zalduendi, Wind Tunnel Parametric Study of Kite Performance for Power Generation (Master's thesis), Cranfield University, 2019, URL: <https://api.semanticscholar.org/CorpusID:213511865>.
- [180] A. Bruining, Aerodynamic characteristics of a curved plate airfoil section at Reynolds numbers 60000 and 100000 and angles of attack from -10 to +90 degrees, 1979, Report LR-281, Delft, Netherlands, Delft Univ. Tech. URL: <https://resolver.tudelft.nl/uuid:6b92442a-01f7-4b7c-8d53-c4f10720ff3e>.
- [181] R. den Boer, Low speed aerodynamic characteristics of a two-dimensional sail wing with adjustable slack of the sail, 1980, Report LR-307, Delft, Netherlands, Delft University of Technology.
- [182] J.M. Van Spronsen, Rigidized Subscale Kite Wind Tunnel Test (Master's thesis), Delft Univ. Tech., 2024, URL: <https://resolver.tudelft.nl/uuid:61f979d7-0d90-4374-b84d-19b57d6d6bea>.
- [183] W. Pulliam, R. Norris, Historical perspective on inflatable wing structures, 2009, <http://dx.doi.org/10.2514/6.2009-2145>, 50th AIAA/ASME/ASCE/AHS/ASC Structures, Structural Dynamics, and Materials Conference.
- [184] S. Schetz, J. Kapania, R. Gupta, S. Desai, Wind tunnel testing of tethered inflatable wings, *J. Aircr.* (2024) 1–18, <http://dx.doi.org/10.2514/1.C037437>.
- [185] J. Wijnja, R. Schmehl, Wind tunnel analysis of the flutter behavior of an airborne wind turbine scale model, 2013, <http://dx.doi.org/10.5446/37652>, Delft Univ. Tech..
- [186] C. Vermillion, B. Glass, S. Greenwood, Evaluation of a water channel-based platform for characterizing aerostat flight dynamics: A case study on a lighter-than-air wind energy system, 2014, <http://dx.doi.org/10.2514/6.2014-2711>, AIAA 2014-2711.
- [187] N. Deodhar, A. Bafandeh, J. Deese, B. Smith, T. Muyimbwa, C. Vermillion, P. Tkacik, Laboratory-scale flight characterization of a multitethered aerostat for wind energy generation, *AIAA J.* 55 (6) (2017) 1823–1832, <http://dx.doi.org/10.2514/1.J054407>.
- [188] K. Geebelen, M. Vukov, A. Wagner, H. Ahmad, M. Zanon, S. Gros, D. Vandepitte, J. Swevers, M. Diehl, An experimental test setup for advanced estimation and control of an airborne wind energy system, in: U. Ahrens, M. Diehl, R. Schmehl (Eds.), *Airborne Wind Energy. Series: Green Energy and Technology*, Springer, 2013, pp. 459–471, http://dx.doi.org/10.1007/978-3-642-39965-7_27.
- [189] K. Geebelen, A small scale experimental setup for testing kite control systems, in: *Airborne Wind Energy Conference 2010*, Stanford, CA, 2010.
- [190] F. Healy, A. Pontillo, D. Rezzui, J.E. Cooper, J. Kirk, T. Wilson, A. Castrichini, Experimental analysis of the dynamics of flared folding wingtips via a novel tethered flight test, *AIAA* 2022-1757 (2022) <http://dx.doi.org/10.2514/6.2022-1757>.
- [191] U.C.I. de Madrid, Web page of the UC3M airborne wind energy group, 2022, URL: <https://aero.uc3m.es/airborne-wind-energy/>.
- [192] CT Engineering Group, The CT engineering group webpage, 2024, URL: <https://www.ctengineeringgroup.com/>.
- [193] U. Fechner, R. van der Vlugt, E. Schreuder, R. Schmehl, Dynamic model of a pumping kite power system, *Renew. Energy* 83 (2015) 705–716, <http://dx.doi.org/10.1016/j.renene.2015.04.028>.
- [194] G. Sánchez-Arriaga, A. Cerrillo-Vacas, D. Unterweger, C. Beaupoil, Dynamic analysis of the tensegrity structure of a rotary airborne wind energy machine, *Wind. Energy Sci.* 9 (5) (2024) 1273–1287, <http://dx.doi.org/10.5194/wes-9-1273-2024>.
- [195] R. Borobia, G. Sánchez-Arriaga, A. Serino, R. Schmehl, Flight-path reconstruction and flight test of four-line power kites, *J. Guid. Control Dyn.* 41 (2018) 2604–2614, <http://dx.doi.org/10.2514/1.G003581>.
- [196] H. Hesse, M. Polzin, T.A. Wood, R.S. Smith, Visual motion tracking and sensor fusion for ground-based kite power systems, in: *Airborne Wind Energy. Series: Green Energy and Technology*, 2018, pp. 413–438, http://dx.doi.org/10.1007/978-981-10-1947-0_17.
- [197] R.V. Castelinio, Y. Kashyap, P. Kosmopoulos, Airborne kite tether force estimation and experimental validation using analytical and machine learning models for coastal regions, *Remote. Sens.* 14 (23) (2022) <http://dx.doi.org/10.3390/rs14236111>.
- [198] F. Fritz, Application of an automated kite system for ship propulsion and power generation, in: U. Ahrens, M. Diehl, R. Schmehl (Eds.), *Airborne Wind Energy*, Springer Berlin Heidelberg, Berlin, Heidelberg, 2013, pp. 359–372, http://dx.doi.org/10.1007/978-3-642-39965-7_20.
- [199] R. Ruiterkamp, S. Sieberling, Description and preliminary test results of a six degrees of freedom rigid wing pumping system, in: U. Ahrens, M. Diehl, R. Schmehl (Eds.), *Airborne Wind Energy*, Springer Berlin Heidelberg, Berlin, Heidelberg, 2013, pp. 443–458, http://dx.doi.org/10.1007/978-3-642-39965-7_26.
- [200] J. Stevenson, K. Alexander, P. Lynn, Kite performance testing by flying in a circle, *Aeronaut. J.* 109 (1096) (2005) 269–276, <http://dx.doi.org/10.1017/S000192400000725>.
- [201] J.C. Stevenson, K.V. Alexander, Circular flight kite tests: converting to standard results, *Aeronaut. J.* 110 (1111) (2006) 605–614, <http://dx.doi.org/10.1017/S0001924000001469>.
- [202] G.M. Dadd, D.A. Hudson, R.A. Sheno, Comparison of two kite force models with experiment, *J. Aircr.* 47 (1) (2010) 212–224, <http://dx.doi.org/10.2514/1.44738>.
- [203] G.M. Dadd, D.A. Hudson, R.A. Sheno, Determination of kite forces using three-dimensional flight trajectories for ship propulsion, *Renew. Energy* 36 (2011) 2667–2678, <http://dx.doi.org/10.1016/j.renene.2011.01.027>.
- [204] J.C. Breuer, R.H. Luchsinger, Inflatable kites using the concept of tensairity, in: *Aerospace Science and Technology*, vol. 14, Elsevier Masson SAS, 2010, pp. 557–563, <http://dx.doi.org/10.1016/j.ast.2010.04.009>.
- [205] L. Fagiano, K. Huynh, B. Bamieh, M. Khammash, On sensor fusion for airborne wind energy systems, *IEEE Trans. Control Syst. Technol.* 22 (2014) 930–943, <http://dx.doi.org/10.1109/TCST.2013.2269865>.
- [206] A. Millane, H. Hesse, T.A. Wood, R.S. Smith, Range-inertial estimation for airborne wind energy, in: 54TH IEEE Conf. Decision and Control, CDC, 2015, pp. 455–460, URL: <https://www.research-collection.ethz.ch/server/api/core/bitstreams/5eaeab2b708-4bd8-8d34-6e67441422ed/content>.
- [207] R. Saraiva, M. De Lellis, E. Schmidt, A. Trofino, Dynamics identification, filtering and control design for power kites, *IFAC-PapersOnLine* 50 (1) (2017) 11938–11943, <http://dx.doi.org/10.1016/j.ifacol.2017.08.1036>.
- [208] M. Ranneberg, Sensor setups for state and wind estimation for airborne wind energy converters, 2013, URL: <http://arxiv.org/abs/1309.1029>.
- [209] E. Schmidt, M.D.L.C.D. Oliveira, R.S.D. Silva, L. Fagiano, A.T. Neto, In-flight estimation of the aerodynamics of tethered wings for airborne wind energy, *IEEE Trans. Control Syst. Technol.* 28 (2020) 1309–1322, <http://dx.doi.org/10.1109/TCST.2019.2907663>.
- [210] M. Behrel, R. Roncin, J.-B. Leroux, R. Hascoet, A. Nême, C. Jochum, Y. Parlier, Application of phase averaging method for measuring kites performance: Onshore results, *J. Sail. Technol.* 3 (2018) 1–29, <http://dx.doi.org/10.5957/jst.2018.05>.
- [211] R. Borobia-Moreno, Application of Aircraft's Flight Testing Techniques to the Aerodynamic Characterization of Power Kites (Ph.D. thesis), Universidad Carlos III de Madrid, 2021, URL: <https://e-archivo.uc3m.es/rest/api/core/bitstreams/98820924-3479-4e6c-9bbe-0149e4c61262/content>.
- [212] F. DeLosRíos-Navarrete, J. González-García, I. Castro-Fernández, G. Sánchez-Arriaga, A small-scale and autonomous testbed for three-line delta kites applied to airborne wind energy, *Wind. Energy Sci. Discuss.* 2024 (2024) 1–20, <http://dx.doi.org/10.5194/wes-2024-170>, URL: <https://wes.copernicus.org/preprints/wes-2024-170/>.
- [213] C. Elfert, D. Göhlich, R. Schmehl, Measurement of the turning behaviour of tethered membrane wings using automated flight manoeuvres, *Wind. Energy Sci.* (2024) <http://dx.doi.org/10.5194/wes-2024-87>.
- [214] E. Schmidt, M.D. Lellis, R. Saraiva, A. Trofino, State estimation of a tethered airfoil for monitoring, control and optimization, *IFAC-PapersOnLine* 50 (2017) 13246–13251, <http://dx.doi.org/10.1016/j.ifacol.2017.08.1960>.
- [215] G.M. Maneia, Aerodynamic Study of Airfoils and Wings for Power Kites Applications (Ph.D. thesis), Politecnico di Torino, 2007, p. 113, URL: <https://zenodo.org/records/7808538>.
- [216] H. Belloc, Wind tunnel investigation of a rigid paraglider reference wing, *J. Aircr.* 52 (2) (2015) <http://dx.doi.org/10.2514/1>.
- [217] G. Sánchez-Arriaga, A. Pastor-Rodríguez, M. Sanjurjo-Rivo, R. Schmehl, A lagrangian flight simulator for airborne wind energy systems, *Appl. Math. Model.* 69 (2019) 665–684, <http://dx.doi.org/10.1016/j.apm.2018.12.016>.
- [218] M.K. Cobb, K. Barton, H. Fathy, C. Vermillion, Iterative learning-based path optimization for repetitive path planning, with application to 3-D crosswind flight of airborne wind energy systems, *IEEE Trans. Control Syst. Technol.* 28 (2020) 1447–1459, <http://dx.doi.org/10.1109/TCST.2019.2912345>.
- [219] P. Williams, B. Lansdorp, W. Ockels, Modeling and control of a kite on a variable length flexible inelastic tether, in: *Collection of Technical Papers - 2007 AIAA Modeling and Simulation Technologies Conference*, vol. 2, 2007, pp. 852–871, <http://dx.doi.org/10.2514/6.2007-6705>.
- [220] P. Williams, Cable modeling approximations for rapid simulation, *J. Guid. Control Dyn.* 40 (2017) 1778–1787, <http://dx.doi.org/10.2514/1.G002354>.
- [221] D. Eijkelhof, R. Schmehl, Six-degrees-of-freedom simulation model for future multi-megawatt airborne wind energy systems, *Renew. Energy* 196 (2022) 137–150, <http://dx.doi.org/10.1016/j.renene.2022.06.094>.
- [222] S. Gros, M. Diehl, Modeling of airborne wind energy systems in natural coordinates, in: U. Ahrens, M. Diehl, R. Schmehl (Eds.), *Airborne Wind Energy. Series: Green Energy and Technology*, Springer, 2013, pp. 181–203, http://dx.doi.org/10.1007/978-3-642-39965-7_10.

- [223] R. Leuthold, J.D. Schutter, E.C. Malz, G. Licitra, S. Gros, M. Diehl, Operational regions of a multi-kite AWE system, in: European Control Conference, 2018, pp. 52–57, URL: <https://publications.syscop.de/Leuthold2018.pdf>.
- [224] J.D. Schutter, R. Leuthold, T. Bronnenmeyer, E. Malz, S. Gros, M. Diehl, AWE-box: An optimal control framework for single- and multi-aircraft airborne wind energy systems, *Energies* 16 (2023) <http://dx.doi.org/10.3390/en16041900>.
- [225] G. Sánchez-Arriaga, M. García-Villalba, R. Schmehl, Modeling and dynamics of a two-line kite, *Appl. Math. Model.* 47 (2017) 473–486, <http://dx.doi.org/10.1016/j.apm.2017.03.030>.
- [226] G. Sánchez-Arriaga, A. Pastor-Rodríguez, R. Borobia-Moreno, R. Schmehl, A constraint-free flight simulator package for airborne wind energy systems, in: *Journal of Physics: Conference Series*, vol. 1037, Institute of Physics Publishing, 2018, 062018, <http://dx.doi.org/10.1088/1742-6596/1037/6/062018>.
- [227] G. Sánchez-Arriaga, J.A. Serrano-Iglesias, R. Leuthold, M. Diehl, Modeling and natural mode analysis of tethered multi-aircraft systems, *J. Guid. Control Dyn.* 44 (2021) 1199–1210, <http://dx.doi.org/10.2514/1.g005075>.
- [228] A. Berra, L. Fagiano, An optimal reeling control strategy for pumping airborne wind energy systems without wind speed feedback, in: *European Control Conference, [IEEE], 2021*, pp. 1199–1204, URL: <https://arxiv.org/pdf/2109.15032>.
- [229] G. Licitra, S. Sieberling, S. Engelen, P. Williams, R. Ruiterkamp, M. Diehl, Optimal control for minimizing power consumption during holding patterns for airborne wind energy pumping system, in: 2016 European Control Conference, ECC 2016, Institute of Electrical and Electronics Engineers Inc., 2016, pp. 1574–1579, <http://dx.doi.org/10.1109/ECC.2016.7810515>.
- [230] M.A. Zempolteca-Jimenez, R. Castro-Linares, J. Alvarez-Gallegos, Trajectory tracking flight control of a tethered kite using a passive sliding mode approach, *IEEE Lat. Am. Trans.* 20 (2022) 133–140, <http://dx.doi.org/10.1109/TLA.2022.9662182>.
- [231] M. Aull, K. Cohen, A nonlinear inverse model for airborne wind energy system analysis, control, and design optimization, *Wind. Energy* 24 (2021) 133–148, <http://dx.doi.org/10.1002/we.2562>.
- [232] S. Diwale, T. Faulwasser, C.N. Jones, Model predictive path-following control for airborne wind energy systems, in: *International Federation of Automatic Control*, vol. 50, Elsevier B.V., 2017, pp. 13270–13275, <http://dx.doi.org/10.1016/j.ifacol.2017.08.1964>.
- [233] J.H. Baayen, W.J. Ockels, Tracking control with adaption of kites, *IET Control Theory Appl.* 6 (2012) 182–191, <http://dx.doi.org/10.1049/iet-cta.2011.0037>.
- [234] G. Sánchez, Dynamics and control of single-line kites, *Aeronaut. J.* 110 (2006) 615–622, <http://dx.doi.org/10.1017/s0001924000001470>.
- [235] E.J. Terink, J. Breukels, R. Schmehl, W.J. Ockels, Flight dynamics and stability of a tethered inflatable kiteplane, *J. Aircr.* 48 (2011) 503–513, <http://dx.doi.org/10.2514/1.C031108>.
- [236] J. Alonso-Pardo, G. Sánchez-Arriaga, Kite model with bridle control for wind-power generation, *J. Aircr.* 52 (2015) 917–923, <http://dx.doi.org/10.2514/1.C033283>.
- [237] M.C.R.M. Fernandes, L.T. Paiva, F.A.C.C. Fontes, Optimal path and path-following control in airborne wind energy systems, in: D. Greiner, B. Galván, J. Périaux (Eds.), in: *Advances in Evolutionary and Deterministic Methods for Design, Optimization and Control in Engineering and Sciences*, vol. 36, Springer, 2021, pp. 409–421, http://dx.doi.org/10.1007/978-3-319-11541-2_1.
- [238] S. Gros, M. Zanon, M. Diehl, Control of airborne wind energy systems based on nonlinear model predictive control & moving horizon estimation, in: 2013 European Control Conference, ECC 2013, IEEE Computer Society, 2013, pp. 1017–1022, <http://dx.doi.org/10.23919/ecc.2013.6669713>.
- [239] M. Kakavand, A. Nikoobin, Numerical simulation of tethered-wing power systems based on variational integration, *J. Comput. Sci.* 51 (2021) <http://dx.doi.org/10.1016/j.jocs.2021.101351>.
- [240] H. Li, D.J. Olinger, M.A. Demetriou, Control of an airborne wind energy system using an aircraft dynamics model, in: 2015 American Control Conference, 2015, pp. 2389–2394, <http://dx.doi.org/10.1109/ACC.2015.7171090>.
- [241] G. Licitra, J. Koenemann, G. Horn, P. Williams, R. Ruiterkamp, M. Diehl, Viability assessment of a rigid wing airborne wind energy pumping system, in: *Proceedings of the 2017 21st International Conference on Process Control, PC 2017*, Institute of Electrical and Electronics Engineers Inc., 2017, pp. 452–458, <http://dx.doi.org/10.1109/PC.2017.7976256>.
- [242] G. Licitra, J. Koenemann, A. Birger, P. Williams, R. Ruiterkamp, M. Diehl, Performance assessment of a rigid wing airborne wind energy pumping system, *Energy* 173 (2019) 569–585, <http://dx.doi.org/10.1016/j.energy.2019.02.064>.
- [243] E.C. Malz, J. Koenemann, S. Sieberling, S. Gros, A reference model for airborne wind energy systems for optimization and control, *Renew. Energy* 140 (2019) 1004–1011, <http://dx.doi.org/10.1016/j.renene.2019.03.111>.
- [244] S. Rapp, R. Schmehl, Enhancing control system resilience for airborne wind energy systems through upset condition avoidance, *J. Guid. Control Dyn.* 44 (2021) <http://dx.doi.org/10.2514/1.G005189>.
- [245] P. Nikpoorparizi, N. Deodhar, C. Vermillion, Modeling , control design , and combined plant / controller optimization for an energy-harvesting tethered wing, in: *IEEE Transactions on Control Systems Technology*, 2017, pp. 1–13, <http://dx.doi.org/10.1109/TCST.2017.2721361>.
- [246] H. Li, D.J. Olinger, M.A. Demetriou, Modeling of airborne wind energy systems: Extended apparent attitude tracking approach, *J. Guid. Control Dyn.* 43 (2020) 847–853, <http://dx.doi.org/10.2514/1.G004366>.
- [247] L. Salord Losantos, G. Sánchez-Arriaga, Flight dynamics and stability of kites in steady and unsteady wind conditions, *J. Aircr.* 52 (2015) 660–666, <http://dx.doi.org/10.2514/1.C032825>.
- [248] J.D. Schutter, R. Leuthold, T. Bronnenmeyer, R. Paelinck, M. Diehl, Optimal control of stacked multi-kite systems for utility-scale airborne wind energy, 2019, 2019 IEEE 58th Conference on Decision and Control (CDC), URL: <https://www.researchgate.net/publication/335827729>.
- [249] B. Houska, M. Diehl, Optimal control for power generating kites, in: *European Control Conference 2007, 2020*, pp. 3560–3567, URL: https://www.researchgate.net/publication/228563408_Optimal_Control_for_Power_Generating_Kites.
- [250] J.D. Schutter, R. Leuthold, M. Diehl, Optimal control of a rigid-wing rotary kite system for airborne wind energy, in: *European Control Conference*, 2018, pp. 1734–1739, URL: <https://publications.syscop.de/DeSchutter2018.pdf>.
- [251] O. Tulloch, A.K. Amiri, H. Yue, J. Feuchtwang, R. Read, Tensile rotary power transmission model development for airborne wind energy systems, in: *Journal of Physics: Conference Series*, vol. 1618, IOP Publishing Ltd, 2020, 032001, <http://dx.doi.org/10.1088/1742-6596/1618/3/032001>.
- [252] S.G.D. Groot, J. Breukels, R. Schmehl, W.J. Ockels, Modeling kite flight dynamics using a multibody reduction approach, *J. Guid. Control Dyn.* 34 (2011) 1671–1682, <http://dx.doi.org/10.2514/1.52686>.
- [253] D. Eijkelhof, S. Rapp, U. Fasel, M. Gaunaa, R. Schmehl, Reference design and simulation framework of a multi-megawatt airborne wind energy system, in: *Journal of Physics: Conference Series*, vol. 1618, IOP Publishing Ltd, 2020, 032020, <http://dx.doi.org/10.1088/1742-6596/1618/3/032020>.
- [254] L. Fagiano, E.N. Van, S. Schnez, Linear Take-Off and Landing of a Rigid Aircraft for Airborne Wind Energy Extraction, Springer Verlag, 2018, pp. 491–514, http://dx.doi.org/10.1007/978-981-10-1947-0_20.
- [255] E.N. Van, L. Fagiano, S. Schnez, On the autonomous take-off and landing of tethered wings for airborne wind energy, in: *Proceedings of the American Control Conference*, 2016, pp. 4077–4082, <http://dx.doi.org/10.1109/ACC.2016.7525562>.
- [256] P. Williams, S. Sieberling, R. Ruiterkamp, Flight test verification of a rigid wing airborne wind energy system, in: 2019 American Control Conference, ACC, 2019, pp. 2183–2190, <http://dx.doi.org/10.23919/ACC.2019.8814338>.
- [257] F. Trevisi, A. Croce, C.E. Riboldi, Flight stability of rigid wing airborne wind energy systems, *Energies* 14 (2021) <http://dx.doi.org/10.3390/en14227704>.
- [258] M. Canale, L. Fagiano, M. Milanese, High altitude wind energy generation using controlled power kites, in: *IEEE Transactions on Control Systems Technology*, vol. 18, 2010, pp. 279–293, <http://dx.doi.org/10.1109/TCST.2009.2017933>.
- [259] N. Orzan, C. Leone, A. Mazzolini, J. Oyero, A. Celani, Optimizing airborne wind energy with reinforcement learning, *Eur. Phys. J. E* 46 (2023) <http://dx.doi.org/10.1140/epje/s10189-022-00259-2>.
- [260] H. Fuest, D.F. Duda, T. Islam, D. Moormann, Stabilization of the vertical take-off of a rigid flying wing for an airborne wind energy system, *CEAS Aeronaut. J.* 12 (2021) 895–906, <http://dx.doi.org/10.1007/s13272-021-00545-3>.
- [261] D.F. Duda, H. Fuest, T. Islam, D. Moormann, Flight guidance concept for the launching and landing phase of a flying wing used in an airborne wind energy system, *Wind. Energy Sci. Discuss.* (2024) 1–25, <http://dx.doi.org/10.5194/wes-2024-90>.
- [262] A. Bosch, R. Schmehl, P. Tiso, D. Rixen, Nonlinear aeroelasticity, flight dynamics and control of a flexible membrane traction kite, in: U. Ahrens, M. Diehl, R. Schmehl (Eds.), *Airborne Wind Energy. Series: Green Energy and Technology*, 2013, pp. 307–323, http://dx.doi.org/10.1007/978-3-642-39965-7_17.
- [263] S. Desai, J.A. Schetz, R.K. Kapania, R. Gupta, Wind tunnel testing of tethered inflatable wings, *J. Aircr.* 61 (6) (2024) 1717–1734, <http://dx.doi.org/10.2514/1.C037437>.
- [264] P. Faggiani, R. Schmehl, Design and economics of a pumping kite wind park, 2018, pp. 391–411, http://dx.doi.org/10.1007/978-981-10-1947-0_16.
- [265] R. Joshi, D. von Terzi, R. Schmehl, System design and scaling trends in airborne wind energy demonstrated for a ground-generation concept, *Wind. Energy Sci.* 10 (4) (2025) 695–718, <http://dx.doi.org/10.5194/wes-10-695-2025>, URL: <https://www.copernicus.org/articles/10/695/2025/>.
- [266] B. Stoevesandt, G. Schepers, P. Fuglsang, Y. Sun, *Handbook of Wind Energy Aerodynamics*, first ed., Springer Cham, 2022, p. 1504, <http://dx.doi.org/10.1007/978-3-030-31307-4>.
- [267] Skysails power website, 2025, <https://skysails-power.com/>. (Accessed 03 November 2025).
- [268] J. Kim, C. Park, Wind power generation with a parawing on ships, a proposal, *Energy* 35 (3) (2010) 1425–1432, <http://dx.doi.org/10.1016/j.energy.2009.11.027>, URL: <https://www.sciencedirect.com/science/article/pii/S0360544209005167>.
- [269] F. Felker, Engineering challenges of airborne wind technology (presentation), in: *Airborne Wind Energy Conference 2010*, Stanford, CA, 2010, pp. 1–20, URL: <https://www.researchgate.net/publication/228563408>.
- [270] S. Le Clainche, E. Ferrer, S. Gibson, E. Cross, A. Parente, R. Vinuesa, Improving aircraft performance using machine learning: A review, *Aerosp. Sci. Tech.* 138 (2023) 108354, <http://dx.doi.org/10.1016/j.ast.2023.108354>.

- [271] R. Vinuesa, S.L. Brunton, Enhancing computational fluid dynamics with machine learning, *Nat. Comput. Sci.* 2 (6) (2022) 358–366, URL: <https://arxiv.org/abs/2110.02085>.
- [272] R. Vinuesa, S.L. Brunton, B.J. McKeon, The transformative potential of machine learning for experiments in fluid mechanics, *Nat. Rev. Phys.* 5 (9) (2023) 536–545, URL: <https://arxiv.org/abs/2303.15832>.
- [273] D. Singh, R.P. Dwight, K. Laugesen, L. Beaudet, A. Viré, Probabilistic surrogate modeling of offshore wind-turbine loads with chained Gaussian processes, in: *Journal of Physics: Conference Series*, vol. 2265, Institute of Physics, 2022, 032070, <http://dx.doi.org/10.1088/1742-6596/2265/3/032070>.
- [274] Z. Deng, Y. Chen, Y. Liu, K.C. Kim, Time-resolved turbulent velocity field reconstruction using a long short-term memory (LSTM)-based artificial intelligence framework, *Phys. Fluids* 31 (2019) <http://dx.doi.org/10.1063/1.5111558>.
- [275] N.B. Erichson, L. Mathelin, Z. Yao, S.L. Brunton, M.W. Mahoney, J.N. Kutz, Shallow neural networks for fluid flow reconstruction with limited sensors, *Proc. R. Soc. A: Math. Phys. Eng. Sci.* 476 (2020) <http://dx.doi.org/10.1098/rspa.2020.0097>.
- [276] A. Moreno Soto, A. Güemes, S. Discetti, Complete flow characterization from snapshot PIV, fast probes and physics-informed neural networks, *Comput. Methods Appl. Mech. Engrg.* 419 (2024) 116652, <http://dx.doi.org/10.1016/j.cma.2023.116652>.
- [277] D. Kochkov, J.A. Smith, A. Alieva, Q. Wang, M.P. Brenner, S. Hoyer, Machine learning-accelerated computational fluid dynamics, *Proc. Nat. Acad. Sci.* 118 (21) (2021) e2101784118, <http://dx.doi.org/10.1073/pnas.2101784118>.
- [278] C. Lee, J. Kim, D. Babcock, R. Goodman, Application of neural networks to turbulence control for drag reduction, *Phys. Fluids* 9 (1997) 1740–1747, <http://dx.doi.org/10.1063/1.869290>.
- [279] J. Rabault, M. Kuchta, A. Jensen, U. Réglade, N. Cerardi, Artificial neural networks trained through deep reinforcement learning discover control strategies for active flow control, *J. Fluid Mech.* 865 (2019) 281–302, <http://dx.doi.org/10.1017/jfm.2019.62>.
- [280] R. Paris, S. Beneddine, J. Dandois, Robust flow control and optimal sensor placement using deep reinforcement learning, *J. Fluid Mech.* 913 (2021) <http://dx.doi.org/10.1017/jfm.2020.1170>.
- [281] D. Fan, L. Yang, Z. Wang, M. Triantafyllou, G.E. Karniadakis, Reinforcement learning for bluff body active flow control in experiments and simulations, *Proc. Natl. Acad. Sci. USA* 117 (2020) 26091–26098, <http://dx.doi.org/10.1073/pnas.2004939117/-/DCSupplemental.y>.
- [282] R. Castellanos, A. Ianiro, S. Discetti, Genetically-inspired convective heat transfer enhancement in a turbulent boundary layer, *Appl. Therm. Eng.* 230 (2023) 120621, <http://dx.doi.org/10.1016/j.applthermaleng.2023.120621>.